Fine structure and Rydberg series of excitons in transition metal dichalcogenides

Piotr Kapuscinski

Wrocław University of Science and Technology

Université Grenoble Alpes

THÈSE

Pour obtenir le grade de

DOCTEUR DE L'UNIVERSITE GRENOBLE ALPES

préparée dans le cadre d'une cotutelle entre l'*Université Grenoble Alpes* et *Wrocław University of Science and Technology*

Spécialité : **NANOPHYSIQUE**

Arrêté ministériel : le 6 janvier 2005 – 25 mai 2016

Présentée par

Piotr KAPUŚCIŃSKI

Thèse dirigée par **Marek POTEMSKI** et **Leszek BRYJA**
et codirigée par **Joanna JADCZAK**

préparée au sein des **Laboratoire National des Champs Magnétiques Intenses** et **Laboratory for Optical Spectroscopy of Nanostructures**
dans **École doctorale de Physique** et **Faculty of Fundamental Problems of Technology**

Structure fine et série de Rydberg des excitons dans les dichalcogénures de métaux de transition

Thèse soutenue publiquement le **21.12.2021**,
devant le jury composé de :

M. Grzegorz SĘK
Professeur, Wrocław University of Science and Technology, Président
Mme Barbara PIĘTKA
Professeur assistant, University of Warsaw, Rapporteur
M. Mark O. GOERBIG
Directeur de Recherche, University of Paris-Saclay, Rapporteur
M. Johann CORAUX
Directeur de Recherche, CNRS, Institut Néel, Grenoble, Membre
M. Jacek KASPRZAK
Chargé de Recherche, CNRS, Institut Néel, Grenoble, Membre

Fine structure and Rydberg series of excitons in transition metal dichalcogenides

Wrocław University of Science and Technology

Piotr Kapuściński

Faculty of Fundamental Problems of Technology
Wrocław University of Science and Technology

École doctorale de Physique
Université Grenoble Alpes

PhD thesis supervised by
prof. dr hab. Marek Potemski and dr hab. inż. Leszek Bryja
and co-supervised by dr hab. inż. Joanna Jadczak

Wrocław, 2021

Abstract

Excitons, the basic excited states in intrinsic semiconducting solids that bring quantum mechanics to life, are of fundamental importance for the optical properties of such materials and provide a platform for optoelectronic device applications. Thus the investigations of the excitonic phenomena in semiconductors are relevant from the point of view of both the fundamental physics research and for understanding the properties of the materials before they can be employed in practical devices. One of the groups of the materials in which the excitons play an especially crucial role are semiconducting representatives of the transition metal dichalcogenides family (TMDs).

TMDs crystallizing in the layered form of van der Waals materials recently gained a second life in the scientific community after the discovery of graphene - a single layer of graphite. In the case of semiconducting transition metal dichalcogenides family (S-TMDs), it was the hexagonal structure (similar to those of graphene) and the presence of the bandgap (which graphene lacks) even in the single-layer that caught the eye of scientists. The dynamic research on these materials revealed further exotic phenomena, many of them related to the physics of excitons, prominent in these materials due to the reduced dimensionality of the carriers and their relatively large effective masses.

In this dissertation, two aspects of the physics of the excitonic complexes in S-TMDs are being studied: their fine structure and the Rydberg series. The former is related to the energy splitting between the excitonic states of different spin configurations. In the first approach, the spin states of excitons can be divided into two groups: bright excitons, which can interact with electromagnetic radiation, and dark excitons, which hardly couple to

photons. The origin of the energy splitting between such states can be related to either the spin-orbit splitting of the conduction and valence bands or differences in the magnitude of both direct and exchange Coulomb interactions. Whereas usually only the ground exciton states are considered, here also the excited states are being probed. The Rydberg series describe the energy levels of excitonic states differing by the principal quantum number. The fine structure is probed for both ground and excited exciton states.

Various representatives of semiconducting transition metal dichalcogenides are being considered in this work, with most of the focus put on the single-layers of group VI S-TMDs such as MoS_2, $MoSe_2$, WS_2 and WSe_2. To improve optical quality (mainly the linewidth of the resonances related to excitonic complexes), those were encapsulated in thin flakes of hexagonal boron nitride. Besides the group VII S-TMD - ReS_2 - has been studied in its bulk form.

Studies presented in this thesis have been performed using the optical spectroscopy techniques: photoluminescence and reflectance, often polarization (circular or linear) resolved. A strong magnetic field (up to 30 T) applied in various experimental geometries (Faraday, Voigt, and intermediate - tilted-field) was used as the primary perturbation of the system that helped to uncover the exciton's fine structure and observe the Rydberg series of bright and dark excitons.

The manuscript is organized into seven chapters. The first two chapters are introductory, with the first one establishing the theoretical background, while in the second one, experimental details and sample preparations are discussed. The following four chapters present the experimental results and their interpretation for the four separate projects, each predeceased by a more detailed introduction and the literature overview. The last chapter summarizes the findings and concludes the work. A short synopsis of all the chapters is given below:

- **Chapter 1 - Introduction**:

  A brief introduction to the physics of excitons, their energy spectrum, and fine structure is given. The properties of transition metal dichalcogenides are discussed, with the most emphasis on representatives from groups VI and VII.

- **Chapter 2 - Samples and methods**:

  In the first part, the procedure for the preparation of samples used in the performed experiments is discussed, and micrographs of typical samples are provided. In the second part, the experimental setups employed during the studies are described in detail.

- **Chapter 3 - Dark excitons in S-TMD monolayers**:

  The topic of dark excitons in group VI S-TMD monolayers is being introduced, the relevant literature is discussed, and the novel magneto-optical results on the exciton fine structure in Mo-based MLs are presented and interpreted. The data obtained from measurements in Voigt configuration prove that the MoS_2, contrary to some previous works, is the "darkish" material - in which the ground state of dark exciton has lower energy than the one of the bright exciton. The g-factors of dark excitons in MoS_2 and $MoSe_2$ monolayers are extracted from measurements performed in tilted-field configuration.

- **Chapter 4 - Rydberg series of dark excitons in WSe_2 monolayer**:

  In this chapter, the fine structure of not only the ground but also the excited states are being considered. It is shown in the example of a WSe_2 monolayer that not only the ground state of dark exciton can be brightened in Voigt configuration, but also the states with a higher principal quantum number. Moreover, the amplitude of the spin-orbit splitting of the conduction band is determined by comparing the energy ladder of bright and dark excitons.

- **Chapter 5 - Highly anisotropic excitons in bulk ReS_2**:

  Detailed magneto-photoluminescence studies of bulk ReS_2 samples performed in various experimental geometries are presented in this chapter. It is shown that two previously reported, linearly-polarised bright exciton Rydberg series share the same bandgap. Two other series of dark excitons are also observed in high magnetic fields in Voigt configuration. The phenomenological model explains the observed energy ladders and the selective coupling between the excitonic states, depends on the direction of the applied magnetic field.

- **Chapter 6 - Singlet and triplet negatively charged excitons - the case of WS_2**:

  The fine structure of negatively charged excitons - the singlet and triplet states - is analysed in an out-of-plane magnetic field. The valley polarisation of free carriers and charged excitons is probed by helicity-resolved reflectance and photoluminescence experiments, respectively. While the valley polarisation of the free electrons can be tuned by magnetic fields and probed by the reflectance experiments, the valley polarisation of trions observed in the photoluminescence response is affected by complex relaxation mechanisms.

- **Chapter 7 - Conclusions**:

  The most important results obtained in this thesis are listed, and the work is concluded.

Résumé

Les excitons, les états excités de base dans les solides semi-conducteurs intrinsèques qui donnent vie à la mécanique quantique, sont d'une importance fondamentale pour les propriétés optiques de ces matériaux et fournissent une plateforme pour les applications des dispositifs optoélectroniques. Ainsi, l'étude des phénomènes excitoniques dans les semi-conducteurs est pertinente tant du point de vue de la recherche en physique fondamentale que pour comprendre les propriétés des matériaux avant qu'ils ne puissent être utilisés dans des dispositifs pratiques. L'un des groupes de matériaux dans lesquels les excitons jouent un rôle particulièrement crucial est celui des semi-conducteurs de la famille des dichalcogénures de métaux de transition (TMD).

Les TMD, cristallisant sous la forme de matériaux en couches stabilisés par des forces de van der Waals, ont récemment acquis une seconde vie dans la communauté scientifique après la découverte du graphène - une couche unique de graphite. Dans le cas de la famille des dichalcogénures de métaux de transition semi-conducteurs (S-TMD), c'est la structure hexagonale (similaire à celle du graphène) et la présence de la bande interdite (dont le graphène est dépourvu) même en monocouche qui ont attiré l'attention des scientifiques. La recherche dynamique sur ces matériaux a révélé d'autres phénomènes exotiques, dont beaucoup sont liés à la physique des excitons, très présents dans ces matériaux en raison de leur dimensionnalité réduite et de leurs masses effectives relativement importantes.

Dans cette thèse, deux aspects de la physique des complexes excitoniques dans les S-TMD sont étudiés : leur structure fine et la série de Rydberg. Le premier aspect est lié au partage de l'énergie entre les états excitoniques de différentes configurations de spin. Dans la première approche, les états

de spin des excitons peuvent être divisés en deux groupes : les excitons brillants, qui peuvent interagir avec le rayonnement électromagnétique, et les excitons obscurs, qui ne se couplent pratiquement pas aux photons. L'origine de la répartition de l'énergie entre ces états peut être liée soit au partage spin-orbite des bandes de conduction et de valence, soit à des différences dans l'ampleur des interactions coulombiennes directes et d'échange. Alors qu'habituellement seuls les états excitoniques fondamentaux sont considérés, les états excités sont également étudiés ici.

La série de Rydberg de l'exciton décrit les niveaux d'énergie des états excitoniques qui diffèrent par le nombre quantique principal, par analogie avec la série de Rydberg de l'atome d'hydrogène. Cependant, comme dans le cas de l'hydrogène, la série de Rydberg converge vers le seuil d'énergie d'ionisation, pour les excitons, elle converge vers l'énergie de la bande interdite. Ainsi, à partir de l'observation de la série de Rydberg excitonique, on peut extrapoler la bande interdite du matériau. De plus, les états excités sont également sujets à la division de la structure fine. Dans cette thèse, elle a été sondée à la fois pour les états excitoniques au sol et excités.

Différents représentants des dichalcogénures de métaux de transition semi-conducteurs sont considérés dans ce travail, l'accent étant mis sur les monocouches des S-TMD du groupe VI tels que MoS_2, $MoSe_2$, WS_2 et WSe_2. Les monocouches sont des semi-conducteurs à bande interdite directe, caractérisés par de forts effets excitoniques et le couplage entre les degrés de liberté de spin et de vallée, où deux vallées peuvent être adressées sélectivement par une lumière polarisée circulairement. Pour profiter de leur qualité optique améliorée (principalement la largeur de raie des résonances liées aux complexes excitoniques), les monocouches encapsulées dans le nitrure de bore hexagonal ont été étudiées dans cette thèse. Le représentant des TMDs du groupe VII, ReS_2 dans sa forme massive, fait également l'objet des recherches présentées dans ce manuscrit. Ce matériau est caractérisé par une forte anisotropie dans le plan de la structure cristalline, conduisant à une forte anisotropie des propriétés optiques. Ceci conduit à son tour à la présence d'excitons se couplant à la lumière polarisée linéairement.

Les études présentées dans cette thèse ont été réalisées en utilisant les techniques de spectroscopie optique : photoluminescence et réflectance, souvent résolues en polarisation (circulaire ou linéaire). Un fort champ magnétique (jusqu'à 30 T) appliqué dans différentes géométries expérimentales (Faraday, Voigt, et intermédiaire - champ incliné) a été utilisé comme perturbation primaire du système qui a permis de découvrir la structure fine de l'exciton et d'observer la série de Rydberg des excitons brillants et obscurs. Le manuscrit est organisé en sept chapitres. Les deux premiers chapitres sont des introductions, le premier établissant le contexte théorique, tandis que le second aborde les détails expérimentaux et la préparation des échantillons. Les quatre chapitres suivants présentent les résultats expérimentaux et leur interprétation pour les quatre projets distincts, chacun étant précédé d'une introduction plus détaillée et d'un aperçu de la littérature. Le dernier chapitre résume les résultats et conclut le travail. Un bref synopsis de tous les chapitres est donné ci-dessous :

- **Chapitre 1 - Introduction** :

  Une brève introduction à la physique des excitons est donnée, en mettant l'accent sur la série des excitons de Rydberg et leur structure fine. Les propriétés des dichalcogénures de métaux de transition sont abordées, en mettant l'accent sur les représentants des groupes VI et VII.

- **Chapitre 2 - Echantillons et méthodes** :

  Dans la première partie, la procédure de préparation des échantillons utilisés dans les expériences réalisées est discutée, et des micrographies d'échantillons typiques sont fournies. Les hétérostructures constituées de monocouches de TMD du groupe VI encapsulées dans le nitrure de bore hexagonal ont été préparées par la technique de l'estampage à sec. Les échantillons de ReS_2 n'ont pas nécessité de préparation particulière, car ils ont été étudiés dans sa forme tri-dimensionnelle. Cependant, comme ces cristaux sont fortement anisotropes, l'orientation du cristal était cruciale dans les expériences. On explique comment elle a été déterminée à l'aide des défauts linéaires visibles à la surface des couches du matériau. Dans la deuxième partie, les montages expérimentaux

employés pendant les études sont décrits en détail. La photoluminescence et la réflectance ont été les techniques utilisées pour sonder les propriétés excitoniques des TMD. Trois montages expérimentaux distincts ont été utilisés pour les mesures de spectroscopie : un montage expérimental basse température à champ nul et deux pour les mesures en champ magnétique : à faisceau libre et à fibre.

- **Chapitre 3 - Excitons obscurs dans les monocouches de S-TMD** :

  Le sujet des excitons obscurs dans les monocouches de S-TMD du groupe VI est introduit, la littérature pertinente est discutée, et les nouveaux résultats magnéto-optiques sur la structure fine des excitons dans les monocouches à base de Mo sont présentés et interprétés. Les mesures de magnéto-photoluminescence dans des champs magnétiques transversaux et inclinés jusqu'à 30 T réalisées sur des échantillons de haute qualité de monocouches de MoS_2 et $MoSe_2$ encapsulées dans du hBN ont permis d'étudier en détail la structure fine des excitons dans ces matériaux. Plus important encore, il a été prouvé que dans la monocouche de MoS_2, l'exciton obscur se situe énergétiquement en dessous de l'exciton brillant, contrairement aux interprétations fournies dans certaines études précédentes. De plus, l'amplitude du partage d'énergie entre les excitons obscurs et brillants dans les monocouches de MoS_2 et $MoSe_2$ a été déterminée à partir de mesures effectuées dans la configuration de Voigt du champ magnétique, tandis que les facteurs g des excitons obscurs ont été extraits des résultats des mesures effectuées dans la configuration de champ incliné. Ces paramètres fondamentaux sont des éléments cruciaux pour comprendre les propriétés optoélectroniques et de vallée de ces semi-conducteurs 2D.

- **Chapitre 4 - Série de Rydberg des excitons obscurs dans la monocouche WSe_2** :

  Dans ce chapitre, on considère la structure fine non seulement des états fondamentaux mais aussi des états excités. Dans ce chapitre, il a été montré pour la première fois, sur l'exemple d'une monocouche WSe_2,

que l'éclaircissement magnétique pouvait être utilisé pour sonder les états excités des excitons obscurs dans les monocouches TMD. Les mesures ont été effectuées sur l'échantillon de haute qualité de monocouche de diséléniure de tungstène encapsulé dans du hBN, pour lequel la série de Rydberg des excitons brillants a pu être observée même sans application de champ magnétique. L'application du champ magnétique dans la configuration de Voigt a conduit à l'apparition des lignes d'émission supplémentaires observées dans le spectre de photoluminescence. Ces lignes ont été interprétées comme les états excités de la série Rydberg des excitons obscurs. L'augmentation quadratique de l'intensité relative de ces états par rapport aux états excitoniques brillants a confirmé cette attribution. La comparaison des échelles d'énergie des séries de Rydberg des excitons brillants et obscurs a permis d'obtenir le paramètre longtemps recherché et très important pour l'interprétation de nombreux résultats expérimentaux dans le WSe_2 monocouches encapsulé dans le hBN - l'amplitude de la séparation spin-orbite de la bande de conduction. Sa valeur de 14 meV, nettement inférieure à celle communément admise, montre que la modélisation théorique des bandes électroniques pourrait nécessiter une révision. Les énergies de liaison de deux espèces d'exciton avec une comparaison avec les masses calculées des électrons dans deux sous-bandes de la bande de conduction suggèrent que l'impact des interactions d'échange sur les énergies de ces deux complexes excitoniques pourrait être négligeable.

- **Chapitre 5 - Excitons hautement anisotropes dans le ReS_2 massif** :

  Les propriétés optiques du diséléniure de rhénium massif sont discutées et des études détaillées de magnéto-photoluminescence d'échantillons de ReS_2 massifs réalisées dans diverses géométries expérimentales sont présentées dans ce chapitre. Plusieurs lignes d'émission qui peuvent être distinguées dans le spectre de photoluminescence à basse température et à champ magnétique nul du disulfure de rhénium massif sont identifiées ici comme deux séries de Rydberg brillantes, séparées par les

interactions d'échange résultant de la faible symétrie du cristal. Les mesures de magnéto-photoluminescence effectuées en géométrie de Voigt révèlent la présence de deux séries de Rydberg obscurs supplémentaires, non dégénérées. Les quatre séries s'hybrident dans le champ magnétique en raison du couplage Zeeman d'une manière complexe, dépendant de la direction dans le plan du champ appliqué. Ces phénomènes peuvent être bien expliqués en utilisant le modèle phénoménologique simple qui considère à la fois les interactions d'échange des états de spin et les hamiltoniens Zeeman décrivant les interactions des spins des porteurs avec un champ magnétique. Ces résultats confirment que les quatre séries excitoniques de Rydberg proviennent du même point de la zone de Brillouin. Toutefois, les résultats obtenus dans la configuration de Faraday ne sont pas aussi simples et, tout comme les règles de polarisation qui régissent ces transitions, ils doivent faire l'objet de travaux théoriques supplémentaires pour être pleinement compris.

- **Chapitre 6 - Excitons singlets et triplets chargés négativement - le cas de WS_2** :

  La structure fine des excitons chargés négativement - les états singlet et triplet - est discutée et analysée dans un champ magnétique hors du plan. L'évolution sous champ magnétique des caractéristiques des trions négatifs dans une monocouche WS_2 encapsulée dans des paillettes de hBN a été étudiée par des expériences de contraste de réflectance et de photoluminescence. Les résultats obtenus par ces deux techniques sont étonnamment différents. Le signal de contraste de réflectance peut être compris en considérant uniquement la redistribution des porteurs entre deux vallées, qui se produit en raison du décalage induit par le champ magnétique des énergies de bande par rapport à l'énergie de Fermi. Cette redistribution permet d'obtenir une forte polarisation de vallée des porteurs libres dans le système en appliquant un champ magnétique, ce qui conduit ensuite à la polarisation circulaire de l'absorption des caractéristiques du trion. En d'autres termes, la polarisation de vallée des porteurs peut être efficacement sondée par des expériences de type absorption résolue en polarisation. De plus, le changement de la

concentration des porteurs dans l'échantillon entraîne un changement des énergies des caractéristiques des trions, modifiant les valeurs des facteurs g effectifs des complexes de trions observés. L'effet de la redistribution des porteurs sur la réponse de la photoluminescence est moins évident. Une augmentation similaire de la polarisation circulaire est observée uniquement dans le cas du trion singulet. Cette divergence pourrait résulter de l'interaction entre les effets concurrents de la relaxation de l'exciton vers des états d'énergie inférieure (qui n'affecte pas les expériences de type absorption) et des changements dans la probabilité de formation des composants polarisés des espèces de trions induits par la redistribution des porteurs entre les vallées. Les expériences nous ont permis d'extraire les valeurs des facteurs g des deux complexes de trions et d'estimer la concentration des électrons. Les résultats décrits révèlent que la polarisation de vallée des électrons libres peut être contrôlée par des champs magnétiques et sondée par les expériences de contraste de réflectance. D'autre part, la réponse de photoluminescence met en évidence la complexité des différents mécanismes impliqués dans l'émission liée aux trions.

- **Chapitre 7 - Conclusions** :

  Les résultats les plus importants obtenus dans cette thèse sont listés et la conclusion de ce travail est revue.

Streszczenie

Ekscytony, stany wzbudzone struktury elektronowej w półprzewodnikowych ciałach stałych, przenoszące teorie mechaniki kwantowej do życia, mają nie tylko fundamentalne znaczenie dla właściwości optycznych tych materiałów, ale także stanowią platformę dla nowych zastosowań w urządzeniach optoelekteonicznych. Dlatego badania zjawisk ekscytonowych w półprzewodnikach są istotne zarówno z punktu widzenia badań fizyki fundamentalnej, jak i zrozumienia właściwości materiałów przed ich zastosowaniem w praktycznych urządzeniach. Jedną z grup materiałów, w których ekscytony odgrywają szczególnie istotną rolę są półprzewodnikowe dichalkogenki metali przejściowych (TMDs).

TMDs krystalizujące w postaci warstwowej materiałów van der Waalsa zyskały drugie życie w środowisku naukowym po odkryciu grafenu - pojedynczej warstwy grafitu. W przypadku rodziny półprzewodnikowych dichalkogenków metali przejściowych (S-TMD) uwagę naukowców przykuła heksagonalna struktura (podobna do grafenu) oraz obecność przerwy wzbronionej (której brakuje grafenowi) nawet w pojedynczej warstwie. Dynamiczne badania tych materiałów ujawniły kolejne egzotyczne zjawiska, wiele z nich związanych z fizyką ekscytonów, które to są wyjątkowo istotne w tych materiałach ze względu na zredukowaną wymiarowość nośników i ich stosunkowo duże masy efektywne.

W niniejszej pracy doktorskiej badane są dwa aspekty fizyki kompleksów ekscytonowych w S-TMDs: ich struktura subtelna oraz serie Rydberga. Pierwszy z nich związany jest z rozszczepieniem energii pomiędzy stanami ekscytonowymi o różnych konfiguracjach spinowych. W pierwszym podejściu, stany spinowe ekscytonów można podzielić na dwie grupy: ekscytonów jasnych,

które mogą oddziaływać z promieniowaniem elektromagnetycznym oraz ekscytonów ciemnych, które nie oddziałują ze światłem. Źródło tego rozszczepienia energii pomiędzy stanami może być związane albo z rozszczepieniem spin-orbita pasm przewodnictwa i walencyjnych, albo z różnicami w wielkości bezpośrednich i wymiennych oddziaływań kulombowskich. Chociaż zwykle rozważane są tylko stany podstawowe ekscytonów, tutaj badane są również stany wzbudzone. Szeregi Rydberga opisują poziomy energetyczne stanów ekscytonowych różniących się główną liczbą kwantową. Struktura subtelna jest badana zarówno dla stanów podstawowych jak i wzbudzonych.

W pracy badani są różni przedstawiciele półprzewodzących dichalkogenków metali przejściowych, przy czym największy nacisk kładziony jest na jednowarstwowe S-TMD grupy VI, takie jak MoS_2, $MoSe_2$, WS_2 i WSe_2. W celu poprawy jakości optycznej (głównie szerokości liniowej rezonansów związanych z kompleksami ekscytonowymi), zostały one zamknięte w cienkich płatkach heksagonalnego azotku boru. Oprócz nich przebadano również reprezentatnta grupy VII S-TMD - ReS_2 - w postaci objętościowej.

Badania przedstawione w tej pracy zostały wykonane przy użyciu technik spektroskopii optycznej: fotoluminescencji i odbicia, często z rozdzielonych polaryzacyjnie (kołowo lub liniowo). Silne pole magnetyczne (do 30 T) przyłożone w różnych geometriach eksperymentalnych (Faradaya, Voigta i pośredniej - "tilted-field") zostało użyte jako główna perturbacja układu, która pozwoliła na badanie subtelnej struktury ekscytonu i zaobserwowanie serii Rydberga jasnych i ciemnych ekscytonów.

Manuskrypt składa się z siedmiu rozdziałów. Dwa pierwsze rozdziały mają charakter wprowadzający, w pierwszym z nich nakreślone jest tło teoretyczne, natomiast w drugim omówione są szczegóły eksperymentalne i przygotowanie próbek. Kolejne cztery rozdziały przedstawiają wyniki eksperymentalne i ich interpretację dla czterech oddzielnych projektów, a każdy poprzedzony jest bardziej szczegółowym wstępem i przeglądem literatury. ostatni rozdział podsumowuje wyniki i kończy pracę. Krótkie streszczenie wszystkich rozdziałów jest podane poniżej:

- **Rozdział 1 - Wprowadzenie**:

  Podano krótkie wprowadzenie do fizyki ekscytonów, ich widma energetycznego i struktury subtelnej. Omówiono właściwości dichalkogenków metali przejściowych, przy czym największy nacisk położono na półprzewodnikowych przedstawicieli z grup VI i VII.

- **Rozdział 2 - Próbki i metody**:

  W pierwszej części omówiono procedurę przygotowania próbek wykorzystywanych w przeprowadzonych eksperymentach oraz zamieszczono zdjęcia z mikroskopu typowych próbek. W drugiej części szczegółowo opisano układy doświadczalne zastosowane podczas badań.

- **Rozdział 3 - Ciemne ekscytony w monowarstwach S-TMD**:

  Przedstawiono wprowadzenie do tematu ciemnych ekscytonów w monowarstwach S-TMD grupy VI, omówiono stosowną literaturę oraz zaprezentowano i zinterpretowano nowatorskie wyniki doświadczeń magnetooptycznych dotyczące struktury subtelnej ekscytonów w MLs dichalkogenków na bazie Mo. Dane uzyskane z pomiarów w konfiguracji Voigta dowodzą, że MoS_2, wbrew niektórym wcześniejszym pracom, jest materiałem “ciemnym” - takim, w którym stan podstawowy ciemnego ekscytonu ma niższą energię niż stan jasnego ekscytonu. g-czynniki ciemnych ekscytonów w monowarstwach MoS_2 i $MoSe_2$ zostały wyznaczone z pomiarów wykonanych w konfiguracji "tilted-field".

- **Rozdział 4 - Serie Rydberga ciemnych ekscytonów w monowarstwie WSe_2**:

  W rozdziale tym rozważana jest struktura subtelna zarówno stanów podstawowych, jak i stanów wzbudzonych. Na przykładzie monowarstwy WSe_2 pokazano, że nie tylko stan podstawowy ciemnych ekscytonów może być rozjaśniony w konfiguracji Voigta, ale również stany o wyższej głównej liczbie kwantowej. Ponadto, poprzez porównanie poziomów energetycznych serii jasnych i ciemnych ekscytonów otrzymano amplitudę rozszczepienia spin-orbita pasma przewodnictwa.

- **Rozdział 5 - Wysoce anizotropowe ekscytony w objętościowym ReS_2**:

  W rozdziale tym przedstawione są szczegółowe badania magnetofotoluminescencji próbek ReS_2 wykonane w różnych geometriach eksperymentalnych. Pokazano, że dwie poprzednio opisane, liniowo spolaryzowane serie Rydberga jasnych ekscytonów charakteryzują się tą samą przerwą pasmową. Oprócz nich, w wysokich polach magnetycznych w konfiguracji Voigta obserwowane są jeszcze dwie inne serie ciemnych ekscytonów. Obserwowane zależności energetyczne i selektywne sprzężenie pomiędzy stanami ekscytonowymi zależne od kierunku pola magnetycznego są dobrze wyjaśnione przez model fenomenologiczny.

- **Rozdział 6 - Singletowe i trypletowe ujemnie naładowane ekscytony - przypadek WS_2**:

  Analizowana jest struktura subtelna ujemnie naładowanych ekscytonów - stanów singletowych i trypletowych - w prostopadłym do płaszczyzny próbki polu magnetycznym. Polaryzacja dolinowa swobodnych nośników i naładowanych ekscytonów jest badana odpowiednio za pomocą eksperymentów odbicia i fotoluminescencji rozdzielonych w polaryzacji kołowej. Pokazano, że te dwie polaryzacje dolinowe różnią się znacząco. Podczas gdy polaryzacja dolinowa elektronów swobodnych może być strojona przez pola magnetyczne i badana przez eksperymenty odbicia, polaryzacja dolinowa trionów obserwowana w fotoluminescencji jest zależna od złożonych mechanizmów relaksacyjnych nośników.

- **Rozdział 7 - Wnioski**:

  Wymieniono najważniejsze wyniki uzyskane w tej rozprawie oraz podsumowano pracę.

Acknowledgements

My doctoral studies were carried out in a cotutelle formula at the University of Grenoble and the Technical University of Wrocław. The result of the three years of work is the research presented in this dissertation. I am extremely grateful to all those who helped make me to complete my PhD and supported me in all the difficulties involved.

Above all, thanks are due to the two supervisors who guided me through this time - Prof. Marek Potemski from Grenoble and Prof. Leszek Bryja from Wrocław. For all the help I received from them, for the patience they showed me despite my stubbornness, for the knowledge they shared with me and for the support and understanding they offered me. Also, for the rather large amount of freedom I was given in my research, which allowed, I believe, to bring out the best in me. Thanks also to my assistant supervisor, Dr Joanna Jadczak, for all her help and for persuading me to take my PhD in a cotutelle formula.

A big thank you also to all the people with whom I worked and who offered me their help and shared their experience and knowledge with me when I needed it: Diana Vaclavkova, Maciej Molas, Alex Delhomme, Clément Faugeras, Ivan Breslawitz, Artur O. Slobodeniuk, Mirek Bartos, Magdalena Grzeszczyk, Jan Dzian, Carlos Rodríguez-Fernández and Joanna Kutrowska-Girzyca. Thanks also to people I did not cooperate with directly: Jan Wyzula, Ivan Mohelsky, Thomas Pelini, Dipankar Jana, Leonid Bovkun, Milan Orlita and Gérard Martinez. Thank you all very much for all the discussions during lunch and coffee breaks and for your help and support. Thanks to all of you, my work was not only much easier but also definitely more enjoyable.

I would also like to thank all the administrative staff in Grenoble and Wroclaw, especially to Alexandra Gasparini and Nina Kuczynska for dealing with my countless travels.

I am incredibly grateful to my parents and brother for all the help and support they offered me during these years of my PhD.

A big thanks to my friends, in particular: Dąbrówka, Gośka, Rafał, Edyta, Andrzej, and all the others, for their support and time devoted to me, which made coping with all the stress much easier.

Contents

1 Introduction **1**

1.1 Excitons . . . 1

1.1.1 Rydberg series . . . 3

1.1.2 Fine structure . . . 6

1.1.3 Excitonic molecules/complexes . . . 7

1.2 Transition metal dichalcogenides . . . 8

1.2.1 TMDs of Group VI . . . 10

1.2.2 TMDs of Group VII . . . 14

2 Samples and methods **17**

2.1 Samples preparation . . . 17

2.1.1 Monolayers of group VI S-TMDs . . . 17

2.1.2 Bulk samples of group VII S-TMDs . . . 18

2.2 Experimental setups . . . 19

2.2.1 Zero-field low-temperature experimental setup . . . 19

2.2.2 Fiber-based setups for measurements in magnetic fields . . . 21

2.2.3 Free-beam setup for measurements in magnetic fields . . . 22

3 Dark excitons in S-TMD monolayers **25**

3.1 Introduction . . . 25

3.2 Theoretical description . . . 29

3.3 Experimental results . . . 30

3.3.1 Magneto-photoluminescence in in-plane magnetic field . . . 30

3.3.2 Magneto-photoluminescence in tilted magnetic field . . . 35

3.4 Discussion . . . 41

3.5 Conclusions . . . 45

4 Rydberg series of dark excitons in WSe_2 monolayer 47

4.1 Introduction . . . 47

4.2 Experimental results - Magneto-photoluminescence in in-plane magnetic field . . . 49

4.3 Discussion . . . 52

4.4 Conclusions . . . 56

5 Highly anisotropic excitons in bulk ReS_2 57

5.1 Introduction . . . 57

5.2 Experimental results . . . 59

5.2.1 Excitonic resonances in PL of bulk ReS_2 . . . 59

5.2.2 Magneto-photoluminescence . . . 62

5.2.2.1 Out-of-plane magnetic field . . . 62

5.2.2.2 In-plane magnetic field $B \parallel b$ . . . 66

5.2.2.3 In-plane magnetic field $B \perp b$ . . . 68

5.2.2.4 In-plane magnetic field $\angle(B, b) \sim 20°$ . . . 68

5.3 Theoretical modelling . . . 69

5.3.1 Phenomenological model . . . 70

5.3.1.1 Exchange terms . . . 70

5.3.1.2 Out-of-plane magnetic field . . . 72

5.3.1.3 In-plane magnetic field $B \parallel b$ . . . 73

5.3.1.4 In-plane magnetic field $B \perp b$ . . . 73

5.3.1.5 Consequences of the model . . . 74

5.3.2 Parameters . . . 76

5.3.3 Comparison with experimental results . . . 76

5.4 Discussion . . . 80

5.5 Conclusions . . . 81

6 Singlet and triplet negatively charged excitons - the case of WS_2 83

6.1 Introduction . . . 83

6.2 Experimental results . . . 87

6.2.1 Trion resonances in tungsten disulfide monolayer . . . 87

6.2.2 Trion resonances in magnetic field - the RC response 89
6.2.3 Trion resonances in magnetic field - the PL response 89
6.3 Discussion 92
6.4 Conclusions 95

7 Conclusions **97**

List of publications **99**

References **103**

1

Introduction

1.1 Excitons

The electronic ground state of the semiconducting material relates to the case when the valence band (VB) is entirely filled by the "sea" of N electrons while the conduction band (CB) is empty. When one of the electrons from the VB is excited to the CB (e.g. due to the absorption of the photon of the adequate energy), it leaves $N-1$ electrons in VB and 1 electron in CB. Alternatively, this can be seen as the presence of N electrons in VB plus one hole - a quasi-particle of the very same properties as the conduction band electron, yet with an opposite sign of charge and with the k-vector of the opposite sign to that of the missing valence electron. Hence the absorption of the light can be viewed as the creation of the electron-hole (e-h) pair. This approach provides a very convenient way of describing the multibody phenomenon by reducing the problem to that of two interacting particles (electron and hole).

When the Coulomb interactions are disregarded, the minimal energy needed to excite the electron from the CB to the VB is equal to the difference of their energies, or in other words, to the bandgap E_g of the semiconductor considered. However, the Coulomb interactions can significantly reduce this energy and therefore one has to take them into account. The source of these Coulomb interactions has to be viewed as the reduction of the Coulomb repulsion between the electrons in the VB and the CB states due to the removal of one of the electrons from "sea" in the VB. This reduction can lead to the binding of the CB electron to the empty VB state or their correlation. When the concept of valence hole is introduced, the additional Coulomb forces come

from the attractive interaction between the negatively charged electron in the CB and the positively charged hole in the VB. This approach is more convenient, as it requires consideration of only two particles. The electron-hole pair correlated by the Coulomb interactions are known as an exciton.

Depending on the strength of the Coulomb interactions, defined mainly by the screening effects, two limiting cases for the excitons can be defined. In the first case, where the electron and hole are tightly bound within the same or neighbouring atomic site, the e-h pairs are called Frenkel excitons, after the author of the first developed model of such excitons (1). Such quasiparticles are often found in ionic crystals. The second case corresponds to the Wannier-Mott excitons (or just Wannier excitons) (2), which appear when the electron and hole are only weakly bound due to the strong screening effects found in most of the semiconducting materials. Thus only the Wannier excitons will be explored further in the text.

The basic properties of the Wannier excitons can be conveniently presented when electronic bands are described within the effective mass approximation (3, 4). Within this approximation, the motion of the carrier from the vicinity of each extremum of a band structure resembles the motion of the free electron in vacuum. The effect of the periodic crystal potential are simply included by introduction of the effective masses of carriers: m_e and m_h, for electrons and holes. Then, the kinetic energy $p^2_{e/h}/2m_{e/h}$ of an electron/hole translates into parabolic dispersions $E_{\boldsymbol{k},e/h} = \hbar^2\boldsymbol{k}^2_{e/h}/2m_{e/h}$ of the electronic/hole bands with the k-vector defined by association with crystal momentum: $\boldsymbol{p}_{e/h} = \hbar\boldsymbol{k}_{e/h}$. The exciton can be naturally seen as the semiconductors' analogue of the hydrogen atom, also the Coulomb bound pair of opposite charges. This analogy is not, however, wholly accurate. In the case of hydrogen atoms, the huge difference in the masses of electron and proton simplifies the description of particles' motion to the case of an electron orbiting around a proton. The similar effective masses of an electron and a hole makes exciton more comparable to an electron-positron pair. The analogy to a hydrogen atom is more adequate for the donor and acceptor states when one of the bound particles has virtually infinite mass.

As the exciton problem is a two-particle one, the motion of the carriers can be separated into a movement of a center-of-mass (CoM) and a relative movement of an electron and a hole around the CoM. The CoM can move freely over the volume of a crystal, acting like a particle with an effective mass $M = m_e + m_h$ and kinetic energy

$E_{k,ex} = \hbar^2 \boldsymbol{K}^2/2M$, where exciton wavevector is equal to: $\boldsymbol{K} = \boldsymbol{k}_e + \boldsymbol{k}_h$. The relative motion of the carriers, on the other hand, is similar to the one of electron and proton in a hydrogen atom, leading to both bound and continuum states. As in hydrogen atoms, the bound states are quantized and described by a principal quantum number n and an orbital angular momentum l, producing $s, p, d, ...$ states. The continuum states relate to the ionized exciton into a free electron and a free hole, wavefunctions of which are still modified due to the Coulomb interactions.

1.1.1 Rydberg series

The energies of the excitonic states can be calculated using the effective mass approximation in the case of a three-dimensional, direct bandgap semiconductor, with parabolic dispersion of the VB and the CB around the bandgap point, in the following way. First, let us assume a zero-energy level to coincide with the top of the VB. In that case, the energy of the hole can be written as: $E_h(\boldsymbol{k}_h) = \hbar^2 \boldsymbol{k}_h^2/2m_h$. Similarly, the energy of the electron: $E_h(\boldsymbol{k}_e) = E_g + \hbar^2 \boldsymbol{k}_e^2/2m_e$. The wave equation for the exciton envelope wavefunction $\Phi(\boldsymbol{R}_e, \boldsymbol{R}_e)$ takes the following form (5):

$$\left[-\left(\frac{\hbar^2}{2m_e}\right) \nabla^2_{\boldsymbol{R}_e} - \left(\frac{\hbar^2}{2m_h}\right) \nabla^2_{\boldsymbol{R}_h} - \frac{e^2}{\kappa |\boldsymbol{R}_e - \boldsymbol{R}_h|} \right] \Phi(\boldsymbol{R}_e, \boldsymbol{R}_e) = E\Phi(\boldsymbol{R}_e, \boldsymbol{R}_e). \tag{1.1}$$

Here, κ is the absolute permittivity of a material and can be expressed as the product of a vacuum permittivity ϵ_0 and static dielectric constant of the material ϵ_r: $\kappa = \epsilon_0 \epsilon_r$. As stated before, this wave equation can be separated into two parts: one for the movement of the CoM and the other describing the relative motion of the carriers. To do so, first a CoM coordinate $\boldsymbol{R}$ and a relative coordinate $\boldsymbol{r}$ have to be defined:

$$\boldsymbol{R} = \frac{m_e \boldsymbol{R}_e + m_h \boldsymbol{R}_h}{m_e + m_h} \text{ and } \boldsymbol{r} = \boldsymbol{R}_e - \boldsymbol{R}_h. \tag{1.2}$$

As the Coulomb interaction does not depend on $\boldsymbol{R}$, the equation for the motion of the CoM can be separated from the relative motion part:

$$\left(-\frac{\hbar^2}{2M}\right) \nabla^2_{\boldsymbol{R}} \psi(\boldsymbol{R}) = E_R \psi(\boldsymbol{R}), \tag{1.3}$$

and

$$\left(-\frac{\hbar^2}{2\mu} - \frac{e^2}{\kappa r}\right) \nabla^2_{\boldsymbol{r}} \psi(\boldsymbol{r}) = E_r \phi(\boldsymbol{r}), \tag{1.4}$$

where μ is the reduced mass of the exciton $\mu^{-1} = m_e^{-1} + m_h^{-1}$. Now the total energy of the exciton will be a sum of the eigenvalues of the Eq.(1.3) and Eq.(1.4). Since the Eq.(1.3) describes free particle, the eigenvalue will contain only the kinetic energy of the CoM:

$$E_R = \frac{\hbar^2 K^2}{2M}. \tag{1.5}$$

The Eq.(1.4), being similar to hydrogen atom equation, gives similar solutions, with the eigenfunctions indexed by three quantum numbers: principal quantum number n, angular quantum number l and magnetic quantum number m. The energies, however, depend only on n in the following way:

$$E_r(n) = E_r(\infty) - \frac{R^*}{n^2}. \tag{1.6}$$

$E_r(\infty)$ here corresponds to the energy for $n \to \infty$ at which the continuum states start, hence it coincides with the band gap E_g, while the R^* is the effective Rydberg, by analogy to hydrogen atom defined as:

$$R^* = \frac{\mu e^4}{2\hbar^2 \kappa^2} = \frac{\mu}{m\epsilon_r^2} \cdot 13.6 \text{ eV}. \tag{1.7}$$

The larger the exciton reduced mass μ and the smaller dielectric screening ϵ_r, the stronger binding between the e-h pair is. Typical semiconductors are characterised by effective masses smaller then the free electron mass and by dielectric constants in the range of $\epsilon_r \sim 10$. The effective Rydberg is typically by two - up to four orders of magnitude smaller then the "bare" Rydberg energy. For example, in the case of gallium arsenide, low temperature static dielectric constant is equal to $\epsilon_r = 12.4$(6), and the exciton reduced mass can be estimated to be $\mu = 0.057m$(7). Hence the effective Rydberg is of the order of 5 meV, and excitons in GaAs can be probed only at low temperatures.

By combining Eq.(1.6) and Eq.(1.5) one gets the total energy spectrum of a Wannier exciton:

$$E(n, K) = E_g + \frac{\hbar^2 K^2}{2M} - \frac{R^*}{n^2}. \tag{1.8}$$

It is presented schematically in Fig. 1.1. Due to the high dispersion of photon energy, only the states around the $K \approx 0$, related to static or nearly static excitons, can be probed optically. Therefore the kinetic energy of the center of mass is often neglected.

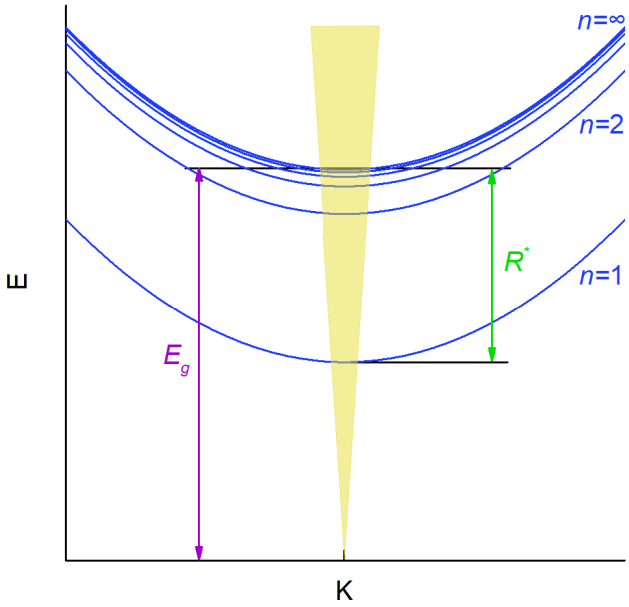

Figure 1.1: Schematic representation of the Wannier exciton energy spectrum (blue lines) with the bandgap E_g and effective Rydberg R^* marked with purple and green arrows, correspondingly. The light cone, representing the dispersion of the photons, marking the excitonic states that can be probed optically, is shown in yellow.

The energy ladder defined by $E(n) = E_g - \frac{R^*}{n^2}$ is usually referred to as the exciton Rydberg series.

For now, all the considerations involved three-dimensional excitons, which are relevant for most of the bulk semiconducting materials. However, in nanostructures, such as quantum wells, quantum dots or quantum wires, the obtained spectrum of the Rydberg series would not be applicable. The exciton spectrum in the N-dimensional space has the following form (8):

$$E(n) = E_g - \frac{R^*}{n + \frac{N-3}{2}}. \tag{1.9}$$

Moreover, this model works also for the anisotropic media, where the static dielectric constant is direction-dependent, since the anisotropic interactions in 3D become isotropic in a lower fractional-dimensional space (8). A very similar result was obtained for the excitons in two-dimensional materials surrounded by the medium of different static dielectric constant (9).

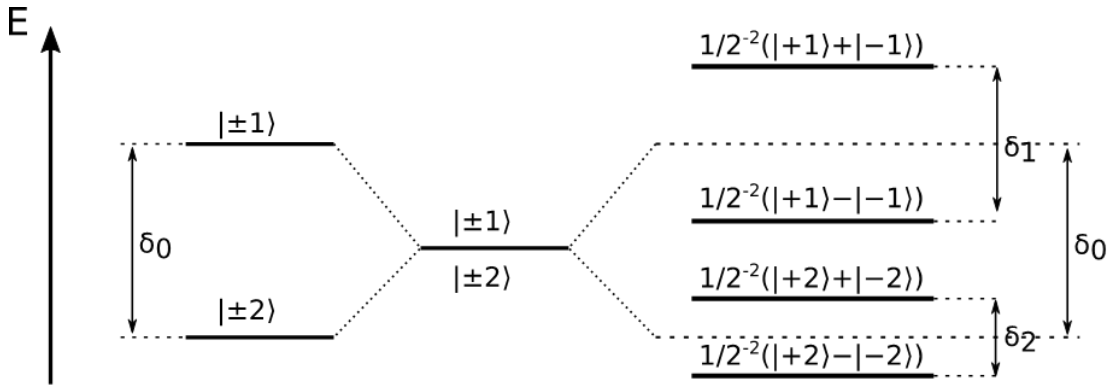

Figure 1.2: Schematic representation of the exchange splitting of the excitonic spin-states. The middle part shows the four-fold degenerated exciton state, without the consideration of the exchange interactions, left part presents the exchange splitting of parallel and anti-parallel spin configurations, while the right part represents the hybridization of both parallel and anti-parallel spin-states, which can be expected in the systems with low symmetry, that leads to the new spin eigenstates and also their energy splitting. In higher symmetries, only parallel or anti-parallel states hybridize, depending on the symmetry. Note that in the systems of lowest symmetries all four spin states can be mixed.

1.1.2 Fine structure

So far, only the direct Coulomb interaction was taken into account in the considerations on exciton energy structure. It gives rise to the spin-degenerated excitonic Rydberg series. This degeneracy can be lifted by either spin-orbit or the exchange Coulomb interactions, depending on the symmetry of the system (10), producing an exciton fine structure. Here, only the exchange splitting will be included to keep the considerations general, while the impact of the spin-orbit splitting of either conduction or valence or both bands will be neglected.

For simplicity, let's consider excitons originating from the only doubly-degenerated conduction and valence bands. Here the spin states of the conduction band (electrons' spins) are denoted as $\{\uparrow,\downarrow\}$ and of the valence band (holes' spins) as $\{\Uparrow,\Downarrow\}$. In that case, four exciton spin-states can be created: $\{|\uparrow\Uparrow\rangle, |\downarrow\Downarrow\rangle, |\uparrow\Downarrow\rangle, |\downarrow\Uparrow\rangle\}$. Those can be divided into to sub-groups of parallel $\{|\uparrow\Uparrow\rangle, |\downarrow\Downarrow\rangle\}$ and anti-parallel $\{|\uparrow\Downarrow\rangle, |\downarrow\Uparrow\rangle\}$ spin configurations. Now, depending on the symmetries of the bands, only parallel or anti-parallel excitons will couple with electro-magnetic radiation. Hence the division into "bright" (interacting with light, optically active or spin-allowed) or "dark" (optically

inactive or spin-forbidden) excitons. Alternatively, these states could be distinguished by their total angular momentum $J = 1, 2$ (or $J = 1, 0$, depending on the system) or its component along z-axis as $\{|+1\rangle, |-1\rangle\}$ in the case of bright and $\{|+2\rangle, |-2\rangle\}$ in the case of dark states. More important for these consideration is, however, that the short-range exchange interaction for excitons with parallel and anti-parallel spin configurations will differ, being a first factor that lifts fourfold spin degeneracy and splitting bright and dark excitons by δ_0, but without the mixing of the spin-states (10), see left panel of Fig. 1.2. The sign of the δ_0 will differ for different symmetries. For example the bright excitons ($J = 1$) will be of lower energy in crystals of T_d symmetry, while in D_{2d} symmetry crystals dark excitons will be the lower energy states (11).

Depending on the symmetry, either only dark (e.g. T_d or D_{2d} or both dark and bright states (e.g. C_{2v}) hybridize due to the short-range exchange interaction, leading to the eigenstates being linear superpositions of the spin-states and an energy splitting of new states (11), as in the right side of Fig. 1.2. Note that in the systems of the symmetries lower than C_{2v} all four states can be mixed(12). The bright states can be independently split by the longitudinal-transverse splitting (long-range exchange interaction) (13). Nonetheless, the symmetry of the system plays a crucial role in defining the exciton fine structure.

The energy scale of the short-range exchange interaction can be said to be of the order of $E_0(a_0/a_e)^3$ (14), where E_0 as the atomic energy ($\sim e^2/a_0$), a_0 is the lattice constant, and a_e is the exciton Bohr radius. Hence, the smaller the exciton is (or, more bound by the direct Coulomb interactions), the stronger the exchange splitting. Besides, the the size of the unit cell itself has an impact on the exchange splitting. The long-range exchange interactions, on the other hand, are of the order of E_b^2/E_g (14), where E_b and E_g are the exciton binding energy and the bandgap, respectively. Therefore the longitudinal-transverse splitting will be the most prominent in the systems with the exciton states bound deeply in the bandgap.

1.1.3 Excitonic molecules/complexes

The exciton X, a Coulomb bound electron-hole pair, is an electrically neutral quasiparticle, just as the hydrogen atom. However, just as in the case of atoms, more complex excitonic quasiparticles can be formed; for example, trions or charged excitons. The negatively charged exciton X^-, consisting of two electrons and a hole, is an analogue of

hydrogen anion (protide) H^-. Such excitonic complex was first theoretically predicted in 1958 by Lampert(15) but they were not unambiguously observed in bulk semiconductor structures due to the small binding energies. However, in 1993 trions were first experimentally evidenced in CdTe/CdZnTe quantum wells (16) in which the binding energy is significantly increased as compared to bulk materials. Also, the positive trions X^+ with one electron and two holes, the analogue of hydrogen cation (hydron) H^+, can be found (17). As such, trions are freely moving carriers of not only energy but also of charge. Trions, however, are hardly observed in bulk crystals, as their binding energy (the difference between exciton and trion energy) is usually too small for these states to be bound in achievable conditions. However, the increase of Coulomb interactions due to the spatial confinement of the carriers in the nanostructures such as quantum wells or dots makes the observation of trions possible.

Not only trions but also complex excitonic molecules were observed in quantum structures. Biexciton (XX or 2X), being an analogue of H_2 molecule consisting of two electrons and two holes, was found in quantum wells (18). In quantum dots, even bigger excitonic complexes were observed, such as charged, or even doubly charged biexcitons (19) or doubly-, triply- or multi-charged excitons(19, 20) or higher multi-excitons such as triexcitons and quadexcitons (20, 21, 22). In such zero-dimensional structures, however, since carriers are confined in the potential defined by the size of the structure, no center of mass movement is possible. Excitons and excitonic complexes are localised and can no longer carry spatially energy and charge.

1.2 Transition metal dichalcogenides

Although the increase of the Coulomb interactions in excitonic complexes due to the spatial confinement makes the semiconductor nanostructures an exciting platform for the studies and application of such quasiparticles, there are some other, easier to obtain systems where the robust excitons are present. Examples of such can be found in semiconducting transition metal dichalcogenides (S-TMDs), materials in which carriers are confined in two-dimensional layers, have relatively high effective masses and are subjected to relatively weak dielectric screening(23). All of that leads to the high excitonic binding energies of tens or hundreds of meVs even in the case of bulk crystals (23, 24).

Transition metal dichalcogenides (TMDs) are formed from the chalcogen atoms (sulphur, selenium or tellurium, denoted here as X) and the transition metal elements (here denoted as T) of the Group VI, V, VI, VII, VIII, IX and X, in the ratio of TX_2 (25). Most of these compounds (except of those containing Group IX transition metal atoms) can be found in the layered structures in which "sandwich" layers of transition metal atom plane surrounded by two chalcogen atom planes are separated by a van der Waals gap. This gap is present due to the fact that although strong covalent forces bind the atoms inside the single layer, the bonding between neighbouring layers includes only weak van der Waals and electrostatic interactions (26). Such structure not only leads to the partial confinement of the carriers in the two-dimensional plane - single layer - but also allows exfoliation into thin layers, for example, by intercalation with lithium (27), ultrasonication (28), or micromechanical cleavage (29, 30), even into monolayers - single "sandwich" layers (30, 31).

The atoms of the same element lie on hexagonal lattice planes. These lattices inside a single "sandwich" layer, but also subsequent layers, can be arranged in many ways, which leads to a wide variety of possible polytypes. The most common polytypes are: 1T, 2Ha, 2Hb, 3Ra and 3Rb. Digit 1,2 or 3 defines the number of layers in the unit cell. The letters T, H, and R stand for the system's trigonal, hexagonal and rhombohedral symmetry. In the 1T and 2Ha structures, the metal atoms are stacked directly above each other, while in the other polytypes, the metal atom hexagonal planes are shifted with respect to each other. In both 2Ha and 2Hb and also 3Ra polytypes, chalcogen atoms surround the metal atoms in trigonal prismatic coordination, while in the 1T and 3Rb phases, the coordination is trigonal antiprismatic (26). These differences in the atom planes stacking, leading to the variations in stacking orders of subsequent layers and metal atom coordination inside a single layer, affect the electronic structure in a significant way and therefore also the resulting properties (26). This is especially well demonstrated by the Group VI MoS_2, which can be either semiconducting in the "natural" 2H phase (23), or metallic in chemically synthesized 1T phase (32).

The metal atom coordination strongly determines the electronic structure of TMDs, and also a number of its *d*-electrons (25). The Group IV TMDs (e.g. TiS_2, $ZrSe_2$ or $HfTe_2$) are found predominantly in a 1T phase and have diamagnetic and semiconducting character (23). TMDs of Group V (e.g. TaS_2, $NbSe_2$ or VTe_2), on the other hand, can be found in both 1T and 2H phases and electronically are narrowband metals,

demonstrating Pauli paramagnetism and band antiferromagnetism (23, 26). The Group VI transition metal dichalcogenides such as MS_2, WSe_2 and $MoTe_2$, naturally found in the 2H phase, are diamagnetic semiconductors (23, 26). Layered group VII TMDs, such as ReS_2 and $ReSe_2$, crystallize in distorted 1T' phase and are semiconducting and diamagnetic compounds (33, 34). Transition metal dichalcogenides of both Group VIII and IX crystallize mostly in the non-layered form. However, there are exceptions, such as the cobalt-based TMDs, which are metallic and antiferromagnetic (23). At last, the Group X TMDs (e.g. PtS_2, $PdTe_2$ or $NiTe_2$) are found predominantly in 1T phase. Tellurides are metallic and Pauli paramagnetic, while the sulfides and selenides are semiconducting and diamagnetic (23).

As the excitonic properties are the primary focus of this thesis, the semiconducting transition metal dichalcogenides (S-TMDs) are of the most interest. The low band-gap of the Group X S-TMDs of the order of 0.4 eV (23), however, makes it impossible to study excitons in these materials by optical spectroscopy in the visible spectrum range, which are the available experimental methods. Moreover, the excitons are not commonly reported for the Group IV S-TMDs. On the other hand, the profound excitonic effects are known to be characteristic for both the Group VI (35, 36, 37, 38) and the Group VII (39, 40) S-TMDs. Therefore this thesis will be focused on the excitons in these two groups. The significantly different properties of compounds from these two S-TMDs groups are described below in more detail.

1.2.1 TMDs of Group VI

The experimental and theoretical studies of bulk crystals (23, 41, 42, 43) and also thin layers (44) of S-TMDS of Group VI started more than half a century ago. At that time, the properties such as the band structure (45) or the excitonic effects (35, 37) were extensively studied and largely understood. However, as it was shown that these materials are indirect semiconductors (45), they were not considered for optoelectronic applications. The successful exfoliation of a single graphite layer (graphene) (46) brought back the attention to other layer materials (29). But it was the discovery of the transition from the indirect bandgap for bulk crystals to the direct bandgap in the monolayer limit (30, 47, 48, 49, 50), that put a spotlight on the Group VI S-TMDs.

The indirect bandgap of $\sim 1.0 - 1.4$ eV in the Group VI S-TMDs, with a value depending on the chalcogen and transition metal elements, is found between valence band

maximum (VBM) at Γ point and the conduction band minimum (CBM) halfway between Γ and K points (49). The electronic states at Γ point consist mostly of chalcogen p_z and transition metal d_{z^2} orbitals (51, 52). The spatial overlap between the neighbouring "sandwich" layers of the electronic states at VBM and CBM is non-negligible. Therefore, when the number of layers decreases, the indirect bandgap increases. On the other hand, CB and VB states at K point contain contributions from d_{z^2} and $d_{x^2-x^2} \pm id_{xy}$ states, respectively, which are strongly localized in the metal atom plane(51, 52). Hence, the direct bandgap at K point stays almost unchanged when a material is thinned down, close to the direct bandgap of the bulk systems, with the size of $\sim 1.4 - 2.2$ eV (49).

When the material is thinned down from the bulk to the monolayer limit, not only the character of the bandgap is changed, but also the symmetry of the system. While the 2H phase TMDs are described by the D_{6h} point group, monolayers have lower symmetry corresponding to the D_{3h} point group. Moreover, since the inversion symmetry is broken, instead of a single K point in the Brillouin zone, there are two inequivalent K^+ and K^- points. The symmetry of the states at this points is characterized by the the C_{3h} point group, what leads to the valley dependent circularly polarised selection rules (53, 54).

Due to the relatively heavy elements that make up the TMDs and the contribution from the d orbitals from a transition metal, the spin-orbit interactions are strong in these materials. The spin-splitting of the valence band at $K^{\pm}$ points reaches 0.2 eV in Mo-based and 0.4 eV in W-based TMD MLs (54, 55, 56). Also, the conduction band is split by the spin-orbit interaction, although the magnitude of this splitting is smaller due to the partial compensation of contributions from p and d orbitals (52, 57). The two contributions of the opposite sign lead to the two different signs of the spin-splitting at CBM, depending on the material. Theoretical calculations suggest that sign of the splitting is defined mostly by the transition metal element (52). Hence, there are two possibilities for the energy ordering of the spin states, which will be a defining factor for many optical properties. The spin-orbit interactions fully lift the spin-degeneracy at K^+ and K^- points, in contrast to conventionally applied semiconductors such as GaAs and CdTe, where both VBM and CBM are spin-degenerate. Moreover, the time-reversal symmetry leads to the opposite sign of the carrier spin for a given valley at two K^+ and K^- points. All these effects render the spin-structure of the bands around the bandgap presented schematically in Fig. 1.3.

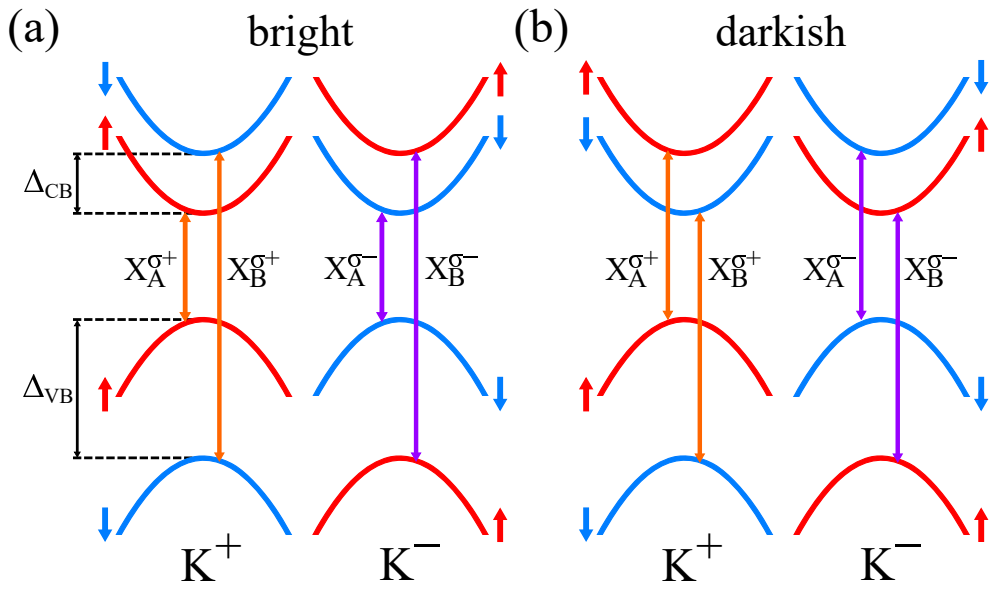

Figure 1.3: Diagram of the subbands relevant for direct optical transitions around the K^+ and K^- points of the BZ in the case of the (a) bright and (b) darkish MLs of S-TMDs along with the optical selection rules.

The selection rules of the optical transitions in these materials are defined by C_{3h} symmetry of the $K^{\pm}$ states. While the orbital Bloch functions of the VB at $K^{\pm}$ are invariants, the states in the CB transform as angular momentum components ± 1 (53, 54). Hence the chiral optical selection rules, according to which only σ^+ (σ^-) circularly polarised light can couple to transition at K^+ (K^-). This rule, together with total angular momentum conservation, leads to the optical transitions between bands of the same spin. Hence the sign of the spin-orbit splitting of the CB will decide whether the lowest energy transition is optically allowed (bright) or forbidden (dark). Based on that, monolayers are divided into "bright" - lowest energy transition is allowed, and "darkish" - lowest energy transition is forbidden. Optical selection rules are compared for "bright" and "darkish" monolayers in Fig. 1.3.

The optical properties of Group VI TMD MLs are largely dominated by the excitonic effects for several independent reasons. The reduction of the dimensionality of the carriers due to their confinement in the thickness of the single monolayer, comparable with their wavefunction size in the out-of-plane direction, leads to the, in principle, fourfold increase of the binding energy in this 2D case as compared with the 3D one (see. Eq.(1.9). Moreover, the effective masses of the carriers are relatively large as

compared with conventional semiconductors, on the order of $\sim 0.5m_0$ (52, 58), leads to high reduced masses μ and hence increased Coulomb interactions. Finally, the dielectric screening is usually reduced in the case of the ML, as they are surrounded by air/vacuum, the low ϵ_r substrate such as Si or SiO_2 or encapsulated in hBN. Altogether these contributions lead to the binding energies of few hundreds of meV (59, 60, 61). Moreover, the aforementioned selection rules allowed valley-selective optical excitation and generation of robust emission polarisation (54, 62, 63, 64). Non-homogeneous dielectric screening, however, leads to non-hydrogenic Rydberg series of excitons in MLs (59, 61). Hence, instead of simple analytical 2D Rydberg formula, the numerical approaches involving solving the problem of exciton in Rytova-Keldysh potential were used (65). The fine structure of exciton was also probed by employing the effect of the magnetic brightening of dark excitons in an in-plane magnetic field, and it was experimentally proven that WSe_2 and WS_2 MLs are of "darkish" type (66, 67).

Not only neutral excitons, but also trions (68, 69, 70) and biexcitons (70, 71, 72) were reported in these materials. Moreover, the series of additional low energy emission lines, described as "localized excitons", were observed in the emission spectra of WSe_2 and WS_2, but the reliable interpretation of their origin was lacking (70, 73, 74). The relatively broad feature linewidths ($\sim$ 50 meV), as compared with the energy separation between various excitonic complexes ($\sim 10 - 30$ meV), made it very difficult to thoroughly study the subtleties of them.

That has changed with the introduction of the encapsulation of S-TMDs in between of flakes of hexagonal boron nitride, which improved the linewidths of excitonic features observed in optical response from few tens of meVs to just a few meVs (75). This opened a new era in the optical studies of the excitonic complexes in monolayers of Group VI S-TMDs. The Rydberg series of bright excitons were now extensively studied (9, 76, 77, 78, 79), as well as the fine structure of neutral excitons (80, 81, 82), although in both cases usually only in hBN encapsulated WSe_2 monolayers. Also, the fine structure of trions was finally probed (83, 84), as well as their excited states (85).

However, few crucial things were missing when the preparation of this thesis has started. One of them was the understanding of the exciton fine structure in molybdenum-based monolayers. The values of the energy splitting between bright and dark excitons were not known, and the question of whether MoS_2 monolayer should be considered "bright" or "darkish" remained somehow controversial. Moreover, although

the fine structure of ground states of excitons in tungsten-based monolayers was much understood, the excited states of dark excitons were never observed, which meant that the extracted dark-bright energy splitting remained the sum of the effects (spin-orbit splitting of CB and Coulomb interactions) with unknown contributions. Finally, the possibility of the employment of the magnetic field to induce valley polarisation of trion features in tungsten-based monolayers was not yet thoroughly studied and understood.

These three, among other, remaining puzzles, are dealt with in this thesis. The fine structure of excitons in molybdenum-based TMD monolayers is explored in Chapter 3. The observation of the Rydberg series of dark excitons in WSe_2 monolayer and the resulting determination of the amplitude of spin-orbit splitting of the conduction band is presented in Chapter 4. Chapter 6 is devoted to the studies of the impact of magnetic field on the singlet and triplet trions in WS_2 monolayer. Each of these studies is preceded by a more in-depth introduction to a given topic.

1.2.2 TMDs of Group VII

Semiconducting transition metal dichalcogenides of Group VII, such as ReS_2 and $ReSe_2$ differ significantly from Group VI TMDs described in the previous section. Instead of the 2H phase typical for Group VI S-TMDs, rhenium based TMDs crystallize in the 1T' phase. Therefore, the mirror symmetry of the single layer is changed into inversion symmetry. Moreover, the strong interactions between rhenium atoms lead to the formation of the Re_4 clusters and, subsequently, the Jahn-Teller distortion of the crystal structure (33, 86, 87, 88). These rhenium clusters form zigzag chains that run along the b-axis of the unit cell, which is also known as the in-plane axis. The resulting in-plane anisotropy leads to firmly different properties from the ones observed in S-TMDs of hexagonal symmetry.

Although most studies, both experimental (89, 90, 91, 92, 93, 94, 95) and theoretical (96), show the indirect bandgap character of these materials, there are also reports contradicting this claim (97, 98, 99). These misunderstandings could be a result of the fact that the indirect bandgap is located in the Brillouin zone neither in the points of the high symmetry nor on the lines connecting such points, which makes it possible to miss a conduction band minimum and valence band maximum in the process of theoretical determination of their band structure (96). Experimental discrepancies could stem from the relatively small energy difference between indirect and direct band gaps (96, 98). In

contrast to the Group VI S-TMDs, the bandgap character does not seem to change when the material is thinned down to the monolayer limit, which is evidenced by the decrease instead of an increase of the PL yield (24, 100). This does not come as a surprise, as the interlayer coupling in Group VII S-TMDs seems to be much weaker, and therefore the electronic and optical properties should be mostly determined by the intra-layer coupling parameters even in the limit of bulk crystals (97, 101, 102, 103, 104, 105).

The in-plane anisotropy of rhenium-based TMDs is reflected in their optical absorption and reflectance spectra which show the linear-polarisation dependence of the absorption edge (92, 93, 94, 106). Besides, it is also prominent in the Raman spectroscopy studies (107, 108, 109, 110) as well as in electrical transport measurements (111, 112). Moreover, the optical response is known to be dominated by the excitonic effects (39, 40). Recently it was shown that two excitonic Rydberg series of different linear polarisations could be found in these materials (24, 113). Still, very little is known about the origin of these excitons. It is not clear where in the Brillouin zone they originate, but also what kind of phenomena lead to the formation of complexes of two different linear polarisations. There are few contradictory propositions, yet none has been confirmed so far. One of them invokes the exchange interaction as the reason for the energy splitting of excitons(105), the other one assigns the excitons to transitions originating at two different points of the Brillouin zone: Z and K1 (114), and yet another one invokes the involvement of different atomic orbitals (113).

The goal of Chapter 5 is to shed new light on this puzzle and to try to unravel the origin of two linearly polarised excitons in the bulk ReS_2. The magnetic field is employed to probe the excitonic complexes observed in the photoluminescence spectra. The measurements show the presence of not only two previously reported, linearly polarised bright exciton series but also two additional dark series.

2

Samples and methods

2.1 Samples preparation

This section aims to briefly describe the preparation procedures that were used to obtain the samples studied in this thesis. Firstly, the dry-stamping technique of preparing the monolayers of group VI transition metal dichalcogenides encapsulated in hexagonal boron nitride is presented. Then, the preparation of the bulk crystals of the group VII S-TMD for measurements is discussed.

2.1.1 Monolayers of group VI S-TMDs

The samples of group VI S-TMDs monolayers encapsulated in hexagonal boron nitride were fabricated by two-stage polydimethylsiloxane (PDMS)-based(115) mechanical exfoliation of S-TMDs and hBN bulk crystals. The commercially available (purchased at HQ Graphene) group VI S-TMDs bulk crystals were used for the exfoliation. The hBN crystals were grown by K. Watanabe and T. Taniguchi at National Institute for Materials Science in Tsukuba, Japan.

In order to prepare the hBN encapsulated monolayer samples, first, the bottom hBN was non-deterministically exfoliated onto the silicon substrate. Then the monolayer of S-TMD and think flake of hBN were mechanically exfoliated using the adhesive tape and subsequently dry-transferred onto the bottom hBN flake using the PDMS stamps. The micrograph of the typical sample is presented in Fig. 2.1. The typical size of the measured hBN/S-TMD-ML/hBN heterostructures samples was of few hundreds of μm^2.

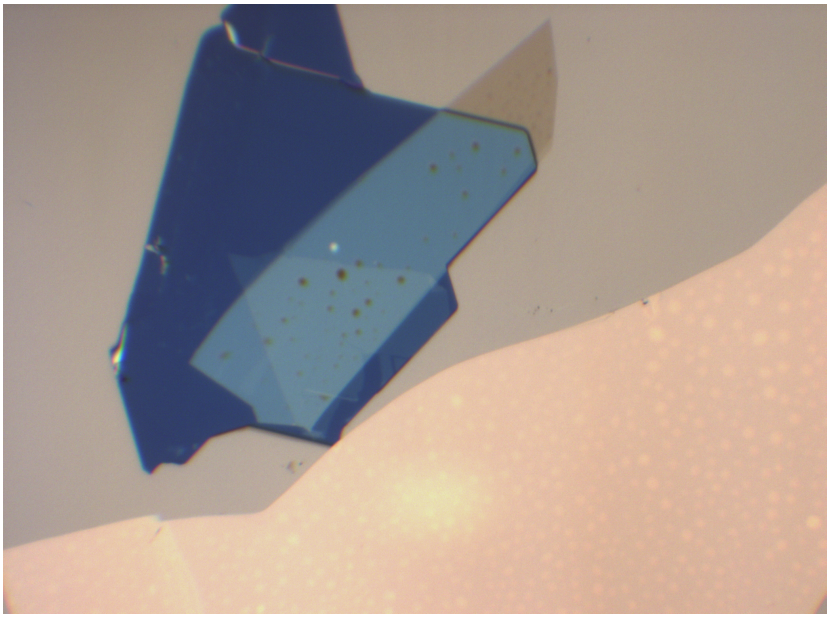

Figure 2.1: Micrograph of the typical sample of an hBN-encpsulated S-TMD monolayer deposited on a silicon substrate, here hBN/WSe_2/hBN/Si. The bottom hBN flake has a dark blue colour, while the area covered by the top hBN flake can be seen as light blue. The triangular shape visible in the light-blue region limits the area of the hBN/WSe_2/hBN heterostructure, which is equal to few hundreds of μm^2.

The samples of molybdenum-based monolayers used for the measurements presented in Chapter 3 were prepared by B. Han at the University of Toulouse, France, and by M. Bartos at Laboratoire National des Champs Magnétiques Intenses in Grenoble, France. The hBN/WSe_2/hBN and hBN/WS_2/hBN heterostructures used for the measurements presented in the Chapters 4 and 6 were prepared by M. Bartos.

2.1.2 Bulk samples of group VII S-TMDs

The bulk ReS_2 crystals used in this study were grown by Professor Y. S. Huang at the National Taiwan University of Science and Technology. The technique used for the growth was chemical vapour transport (CVT).

The samples used for the optical experiments presented in Chapter 5 were prepared by attaching the bulk ReS_2 crystal flakes to silicon substrates using photo-glue. The micrograph of a typical sample is presented in Fig. 2.2. Vertical line defects or breaks can be seen on the sample surface. These lines indicate the rhenium chains in the

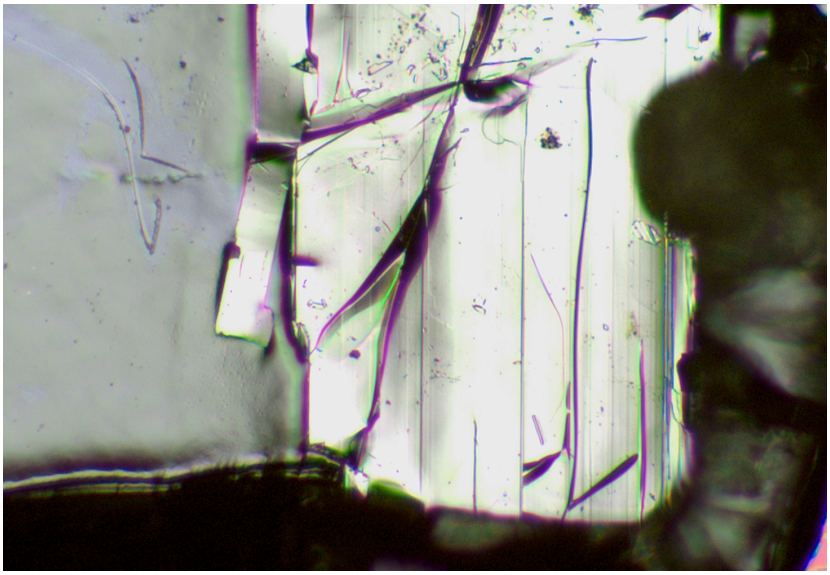

Figure 2.2: Micrograph of typical bulk ReS_2 sample. The vertical cracks visible on the material's surface, indicative of the direction of the b-axis of the crystal, were used to align the sample with respect to one of the edges of the Si substrate.

material, as the strong Re-Re bonds lead to the preferential breaking along them (also here denoted as b-axis of the crystal)(108, 116). Those cracks were used to align the b-axis along or perpendicularly to the well-defined edge of the silicon substrate in order to be able to control the alignment of the sample with respect to the experimental setup and, finally, to the direction of the magnetic field.

2.2 Experimental setups

This Section is dedicated to the presentation of the experimental setups used for the studies of the optical properties of semiconducting transition metal dichalcogenides presented in this thesis. The zero-field micro-photoluminescence and micro-reflectance setup are shown along with the two magnetophotoluminescence setups built around fiber-based and free-beam insert probes.

2.2.1 Zero-field low-temperature experimental setup

The experimental setup used for the micro-PL and micro-RC measurements is schematically depicted in Fig. 2.3. In the case of the micro-PL experiments, a CW diode-

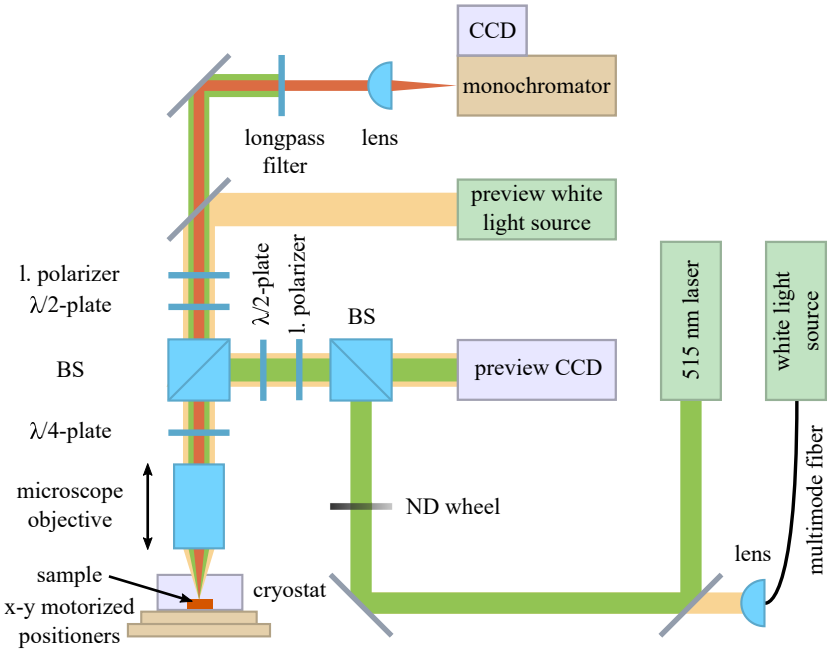

Figure 2.3: Schematic illustration of the experimental setup used for zero-field low-temperature measurements.

pumped laser with a 515 nm wavelength was used as an excitation source, while the micro-RC employed a tungsten halogen lamp as a white light source. White light was introduced to the setup through the multi-mode fiber, whose output was collimated by a lens to achieve a parallel beam. The power of the excitation beam was controlled by the continuously variable neutral density filter wheel. After passing through two 70:30 beam-splitters, the excitation light was focused with an infinity-corrected objective ($M = 50\text{X}$, $NA = 0.5$), which allowed to achieve the excitation spot on the sample's surface of the size of $\sim 1\mu\text{m}^2$. The sample itself was placed on a cold finger of a continuous flow cryostat, which allowed it to achieve a temperature close to the one of liquid helium ($T = 4.6 - 5$ K) and control it using heaters. The cryostat was mounted on the motorized x-y positioners, enabling precise movement of the excitation sport on the surface of the sample. The same objective collected the signal, and the second beam-splitter separated the collection and excitation axis. The collected light was focused by a lens on the slit of 0.5 m long monochromator equipped with 300 g/mm or 600 g/mm gratings and dispersed on the liquid nitrogen cooled CCD camera, used to detect the signal. In the case of the micro-PL experiments, the excitation light was

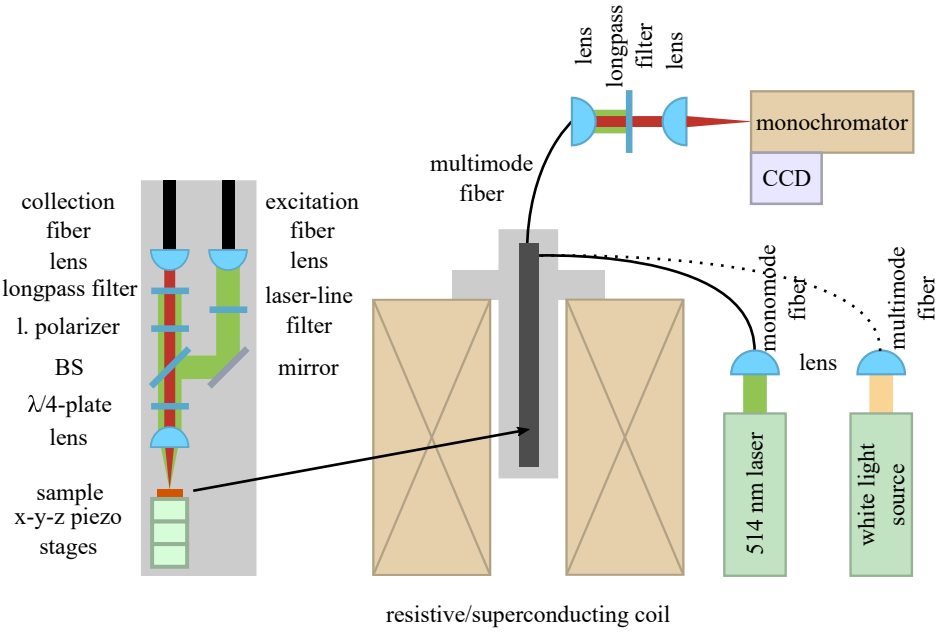

Figure 2.4: Schematic illustration of the experimental setup with the optical fiber-based insert probe used for micro-photoluminescence and micro-reflectance measurements in magnetic fields.

removed from the signal by the longpass filter.

The preview of the surface of the sample was enabled by the introduction of the white light from another source to the collection axis by the mirror on the flip mount and the placement of the preview CCD camera behind the first beam-splitter. In the case of polarization-resolved experiments, polarization control was introduced with the proper sets of quarter-wave-, half-wave plates and linear polarisers. In order to avoid detection artefacts related to the anisotropic setup, response polarisation of the signal was controlled by the motorized half-wave plate inserted before the fixed linear polariser.

2.2.2 Fiber-based setups for measurements in magnetic fields

The magneto-photoluminescence and magneto-reflectance measurements of the spin-forbidden dark excitons and valley polarisation of trions, presented in Chapters 3 and 6, respectively, were performed with similar setups, presented schematically in Fig. 2.4. Two magnet systems available in the Grenoble High Magnetic Fields Laboratory were used: (a) a superconducting magnet producing magnetic fields up to 14 T and (b) a 20 MW resistive magnet with a 50 mm bore diameter producing magnetic fields up to

31 T. In both cases, optical fiber-based insert probes kept in the bath cryostat were used to align the sample in the centre of the field. The sample was placed on top of the x-y-z piezo-stage in gaseous helium at $T = 4.2$ K. The excitation beam was introduced into the insert probe by the optical fiber. In the case of the photoluminescence measurements, it was CW diode-pumped laser with a 515 nm wavelength coupled into the monomode fiber with a 10 μm core diameter, while for the reflectance measurements, white light from tungsten halogen lamp was coupled into the multimode fiber with a 50 μm core diameter. Inside the insert probe, a set of optical elements was used. The excitation light from the fiber was firstly collimated by the lens. The excitation light was introduced into the collection axis by the mirror and beamsplitter and focused on the sample surface by the aspheric lens. The excitation spot on the surface of the sample was of the size of $\sim 1\mu\text{m}^2$ for photoluminescence and $\sim 5\mu\text{m}^2$ for reflectance measurements. The signal was collected by the same lens and coupled into the collection fiber by another lens. The light from the collection fiber was first collimated and then focused on the slit of the 0.5 m long monochromator. The liquid nitrogen cooled CCD camera was used to detect the signal.

In the case of the micro-PL experiments, the excitation light was removed from the signal by the longpass filter before and after the collection fiber. Additionally, the excitation beam was cleaned by the laser-line filter from the light produced by inelastic scattering in the excitation fiber.

Circular polarisation of the signal was achieved by insertion of the quarter-wave plate between beamsplitter and lens, focusing the light on the sample and linear polariser just before the lens coupling the light into the collection fiber.

2.2.3 Free-beam setup for measurements in magnetic fields

While the setup described in the previous section is very convenient for micro-PL measurements in magnetic fields, the control of linear polarisation of the collected light, much needed for the measurements of the ReS_2 samples presented in Chapter 5, is very difficult, mainly due to the usage of the optical fibers for extraction of the signal. For that reason, a free-beam insert probe-based setup, presented schematically in Fig. 2.5, was used to conduct these experiments, and also experiments presented in Chapter 4. In this setup, optical fiber is used only to transmit excitation light from the source to the probe. In the case of the experiments on ReS_2, a CW 633 nm diode-pumped

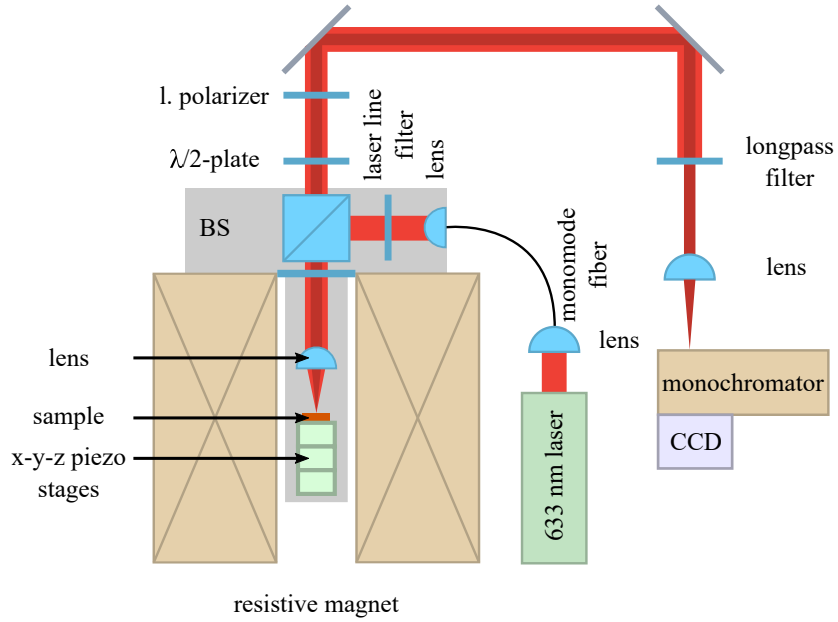

Figure 2.5: Schematic illustration of the experimental setup with the free-beam insert probe used for micro-photoluminescence measurements in magnetic fields.

laser with wavelength close to the signal was used to reduce the negative impact of the focusing lens achromaticity. The experiments on the excited states of dark excitons in WSe_2 described in Chapter 4 employed a CW diode-pumped laser with a 515 nm wavelength. Excitation light was transmitted to the probe by the monomode fiber with a 10 μm core diameter, where it was collimated with a lens, filtered by the laser-line filer, directed onto the optical window of the probe by the beamsplitter, which also separated excitation and collection axis. The lens was used to focus the light on the sample's surface, giving the excitation spot of the size of 1 μm^2. The sample was placed on x-y-z piezo-stage in gaseous helium at $T = 4.2$ K, with the whole probe kept in the helium bath cryostat. The same lens was used to collect the signal, which was analysed by a half-wave plate and linear polariser. The long-pass filter was used to remove the excitation light from the signal, and the lens was used to focus the collected beam on the slit of 0.5 m long monochromator. Again, the liquid nitrogen cooled CCD camera was used to detect the signal.

3

Dark excitons in S-TMD monolayers

3.1 Introduction

Monolayers (MLs) of semiconducting transition metal dichalcogenides (S-TMDs) of the group VI, with general formula MX_2 where M = Mo or W and X = S or Se, are direct bandgap semiconductors, with the bandgap located in two corners (K^+ and K^- points) of the two-dimensional Brillouin zone (BZ) (30, 49), which are inequivalent due to the lack the inversion symmetry (53). Moreover, strong spin-orbit coupling (SOC) originating mainly from the d orbitals of the transition metal atoms (55) produces significant spin-splitting in the valence (VB) band. Together, lack of inversion symmetry and SOC lead to the coupling of the spin and valley degrees of freedom, allowing selective excitation of the carriers with various combinations of spin and valley indices by photons of different circular polarisations and energies (54). In both valleys, two kinds of excitons can be formed: A-exciton, which includes a hole from the top VB, and B-exciton, with a hole from the lower VB subband. Optical selection rules of S-TMDs MLs are presented schematically in Fig. 1.3.

The SOC leads to the spin-splitting of the VB (Δ_{VB}), of the order of the hundreds of meVs, and varies in different S-TMDs between $\sim 200 - 400$ meV (52). This rather large splitting implies that the energy difference between A- and B-excitons is significant, and so the B-excitons do not play an essential role in the optical properties around the bandgap energies. On the other hand, the spin-splitting of the CB (Δ_{CB}) is a bit more

complicated. Firstly, its value is very small, less than 10% of the Δ_{VB}, and due to that, it was initially neglected in the first studies of the MLs of semiconducting transition metal dichalcogenides. However, it can still play an important role at low temperatures. Secondly, it can differ by the sign for different materials. Both stem from the fact that the Δ_{CB} is the result of a competition between two factors: (i) first-order contribution from the chalcogen atoms and (ii) second-order contribution due to the coupling to the other bands (58, 117). Thus the sign and the value of the Δ_{CB} depends on the material and, in consequence, two ways of the band ordering of the CB subbands are possible (58, 118). This has a considerable impact on the fine structure of excitons around the bandgap, which will be primarily defined by this splitting.

Due to the optical selection rules, the band ordering has a significant impact on the optical properties of TMDs MLs. The sign of the spins in the top VB and bottom CB have a major impact on whether the exciton ground state is bright (the spins of the bands are parallel) or dark (when the spins are anti-parallel). Based on this ordering, the MLs of S-TMD are divided into two families: bright and darkish ones (66). Both are presented schematically in Fig. 3.1. The theoretical calculations based on DFT methods predict the bright ordering for $MoSe_2$ ML and darkish ordering for WSe_2 and WS_2 MLs, with the conduction band splitting of an order of 20-40 meV (52, 57, 117). In MoS_2 ML, the Δ_{CB} is predicted to be very small, of the order of few meVs only (52, 57, 117) and in this case, the difference between the dark and bright exciton binding energies can also have an impact on whether the lowest energy exciton is bright or dark.

The fine structure of exciton hugely determines the optoelectronic properties (119, 120, 121, 122), as well as spin relaxation of excitons (123). Thus, the knowledge about the energy ordering of excitons is crucial. However, it is not easy to determine the energy of dark states experimentally. Dark states from the K^+ and K^- valley (intravalley dark excitons) nominally interact only with light polarised in a direction perpendicular to the ML's plane, hence cannot be observed optically when probed from out-of-plane direction (81, 124, 125). However, the exchange interaction mixes the dark states from opposite valleys, lifting the energy degeneracy. The new higher energy eigenstate has the whole (yet extremely small as compared with the bright excitons) oscillator strength and is therefore named as "grey exciton" (X_G), while the lower energy eigenstate does not interact with optical field of any polarisation and remains called as "dark exciton" (X_D) (125, 126). The interaction of the grey exciton with in-plane propagating light can

and was successfully used to determine the ordering of the excitons in WSe_2 and WS_2 MLs (81, 125). This was possible only because of the relatively large (several tens of meV) energy difference between bright and grey excitons, which compensated the small oscillator strength by huge population difference favouring grey exciton (as compared with optically active, bright ones). For that reason, such a technique would not work in the case of smaller energy splitting or if the grey state has higher energy than a bright one.

Fortunately, the relatively small Δ_{CB} enables the manipulation of the spins of the conduction band with the external magnetic field. The bright and dark valley excitons and the influence of magnetic fields applied in-plane or out-of-plane of the ML of darkish materials are presented schematically in Fig. 3.1. The magnetic field applied perpendicularly to the ML's plane induces Zeeman shift, lifting degeneracy of the energy bands in opposite valleys and allows to control control the splitting of dark/grey excitons (82). On the other hand, the in-plane magnetic field induces Zeeman coupling between conduction bands split by the SOC and therefore also the coupling of the dark and grey excitons with the bright ones (125). This coupling implies a transfer of optical activity from bright to dark and grey excitons, which can then interact with the in-plane

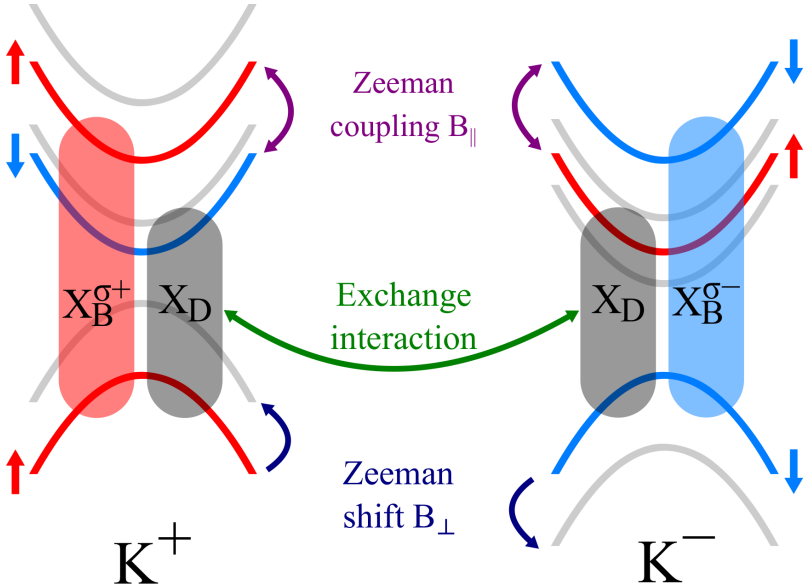

Figure 3.1: Schematic representation of the spin and valley structure of the darkish materials around the band gap in the BZ along with the influence of the perpendicular and in-plane magnetic fields

polarised optical field. Magnetic brightening of the dark excitons is a technique widely used in the studies of nanostructures of semiconducting materials, such as quantum wells, dots, wires, and carbon nanotubes (127, 128, 129, 130, 131, 132, 133), and was recently successfully used on tungsten based MLs, providing the first direct experimental confirmation that these materials are indeed darkish (66, 120). Subsequent improvement of the quality of the measured structures with remarkable reduction of the linewidth of emission lines, achieved by encapsulation of the MLs of S-TMD in hexagonal boron nitride (75) allowed for more detailed studies of dark and grey excitons. In particular, it enabled studies of linear polarisation of the dark and grey excitons and determination of the value of the energy splitting induced by exchange interaction in WSe_2 (80), and WS_2 (134). Moreover, also dark trions were directly observed in tungsten-based MLs (80, 134, 135). However, dark excitons in molybdenum based S-TMDs were not successfully observed experimentally for a few years. One article suggested the presence of the dark state in MoS_2 around 100 meV below the bright exciton (66), but the existence of the wide defect states band in the same energy region and the surprisingly high energy difference between dark and bright ($\Delta_{\mathrm{D-B}}$) states made these suggestions questionable.

Finally, dark excitons were also observed in $MoSe_2$ ML by the brightening in magnetic field (136). Although these results confirmed the bright nature of this material, the big surprise came from the fact that the splitting between bright and dark states was found to be equal to only $\Delta_{\mathrm{D-B}} = -1.5$ meV, more than an order of magnitude less than two tens of meVs expected from the calculations of the Δ_{CB}. This discrepancy was explained by the difference in the dark and bright exciton binding energies, resulting from (i) different values of the masses of electrons residing in two conduction band subbands (52) and (ii) short-range electron-hole exchange interaction (137), which depends on the configuration of the carries' spins. Such interpretation was also in line with the differences observed between Δ_{CB} expected from theory and measured $\Delta_{\mathrm{D-B}}$ for tungsten-based monolayers, suggesting that also MoS_2 ML can be expected to be of darkish type.

To confirm these surprising findings and probe their consequences, the magneto-photoluminescence studies in Voigt and "tilted-field" geometries of the molybdenum-based monolayers were performed and the results of these studies are presented in this chapter. First, the theoretical framework used to describe the fine structure of the excitons and their interaction with the magnetic field in MLs of the group is presented.

Next, the measurement of the $MoSe_2$ ML in Voigt and "tilted-field" geometries are shown, followed by the MoS_2 probed in the same configurations. These results are then discussed, and finally, the conclusions are drawn.

3.2 Theoretical description

There are two convenient ways of choosing basis for the description of the fine structure of the excitons in group VI S-TMDs MLs: (i) one with four intervalley A-exciton states (80) and (ii) the other one with the two intervalley bright excitons, the dark exciton and the grey exciton. Here the first approach will be presented and used. Is this convention the basis states $\left|\mathbf{K}^{\pm}, s_c\right\rangle$ can be distinguished by the valley $\mathbf{K}^{\pm}$ and the projection of the spin in the conduction band $s_c = \uparrow, \downarrow$. Since for A-excitons the spin projection in valence band is fixed to be $s_v = \Uparrow$ in $\mathbf{K}^{+}$ and $s_v = \Downarrow$ in $\mathbf{K}^{-}$, the $\left|\mathbf{K}^{+}, \uparrow\right\rangle$ and $\left|\mathbf{K}^{-}, \downarrow\right\rangle$ states are bright and can be denoted as $\left|\mathbf{K}^{+}, B\right\rangle$ and $\left|\mathbf{K}^{-}, B\right\rangle$, respectively. The same way the $\left|\mathbf{K}^{+}, \downarrow\right\rangle$ and $\left|\mathbf{K}^{-}, \uparrow\right\rangle$ are dark and can be denoted as $\left|\mathbf{K}^{+}, D\right\rangle$ and $\left|\mathbf{K}^{-}, D\right\rangle$, respectively.

The effective Hamiltonian taking into account both spin-orbit and exchange interactions in the basis of the intervalley bright and dark excitons $\{\left|\mathbf{K}^{+}, B\right\rangle, \left|\mathbf{K}^{-}, B\right\rangle, \left|\mathbf{K}^{+}, D\right\rangle, \left|\mathbf{K}^{-}, D\right\rangle\}$ takes the following form:

$$\mathcal{H}_{ex} = \begin{pmatrix} -\Delta_{\mathrm{D-B}} & 0 & 0 & 0 \\ 0 & -\Delta_{\mathrm{D-B}} & 0 & 0 \\ 0 & 0 & \delta/2 & \delta/2 \\ 0 & 0 & \delta/2 & \delta/2 \end{pmatrix}. \tag{3.1}$$

The $\Delta_{\mathrm{D-B}}$ denotes the energy difference between the dark and bright states, while δ represents the exchange interaction between the $\left|\mathbf{K}^{+}, D\right\rangle$ and $\left|\mathbf{K}^{-}, D\right\rangle$ states. This exchange coupling of dark states lifts their degeneracy, leading to two new eigenstates (grey and dark excitons) $|G\rangle, |D\rangle = (\left|\mathbf{K}^{+}, D\right\rangle \pm \left|\mathbf{K}^{-}, D\right\rangle)/\sqrt{2}$ split by the energy equal to δ.

To include the effect of the out-of-plane magnetic field $\mathbf{B}_{\perp} = (0, 0, B_z)$ on the excitonic states, the following Hamiltonian has to be added to the exchange Hamiltonian:

$$\mathcal{H}_{\perp} = \frac{\mu_B}{2} \begin{pmatrix} +g_{\mathrm{B}} B_z & 0 & 0 & 0 \\ 0 & -g_{\mathrm{B}} B_z & 0 & 0 \\ 0 & 0 & +g_{\mathrm{D}} B_z & 0 \\ 0 & 0 & 0 & -g_{\mathrm{D}} B_z \end{pmatrix}. \tag{3.2}$$

Here, g_{B} and g_{D} are the out-of-plane g-factors of the bright and dark excitons, respectively, while the μ_B represents the Bohr magneton. The B_z lifts the degeneracy of the bright valley excitons and changes the energies of valley dark excitons, reducing the effect of the exchange interaction, leading back to the eigenstates of the dark valley excitons for $B_z >> \dfrac{\delta}{\mu_B g_{\mathrm{D}}}$.

The in-plane magnetic field $\mathbf{B}_{\parallel} = (B_x, B_y, 0)$ can be included by addition of the following Hamiltonian:

$$\mathcal{H}_{\parallel} = \frac{\mu_B}{2} \begin{pmatrix} 0 & 0 & g_{\parallel}(B_x - iB_y) & 0 \\ 0 & 0 & 0 & g_{\parallel}(B_x + iB_y) \\ g_{\parallel}(B_x + iB_y) & 0 & 0 & 0 \\ 0 & g_{\parallel}(B_x - iB_y) & 0 & 0 \end{pmatrix}. \tag{3.3}$$

Here, the $g_{\parallel}$ is the in-plane g-factor, which determines the strength of the Zeeman coupling between the conduction band electronic states with the opposite spin in the same valley, leading to the mixing of the intravalley dark excitons with the bright excitons from the same valley. That allows transferring some of the in-plane oscillator strength from the bright excitons to the dark excitons, leading to the brightening effect.

The application of the out-of-plane and in-plane magnetic fields provides a way to control dark states' energies and probe them, respectively. The valley content of the dark and grey excitons can be tuned by applying $\mathbf{B}_{\perp}$. By increasing $\mathbf{B}_{\parallel}$, one can mix dark states with bright ones, leading to the brightening effect, which opens the possibility to probe mixed states optically.

3.3 Experimental results

In order to study the properties of dark excitons in MoS_2 and $MoSe_2$ MLs, magneto-photoluminescence measurements in in-plane and tilted magnetic fields were performed. The in-plane configuration allowed to determine the energies of the dark states, while the tilted field geometry enabled determination of their out-of-plane g-factors.

3.3.1 Magneto-photoluminescence in in-plane magnetic field

The effect of an in-plane magnetic field on the low temperature ($T = 4.2$ K) photoluminescence spectra of MoS_2 ML encapsulated in hBN was first studied. The false-colour

map of the PL intensity as a function of the in-plane magnetic field from 0 T to 30 T is presented in Fig. 3.2. At 0 T, only one emission line at 1.931 eV is observed in the presented energy range, corresponding to the bright exciton X_B radiative recombination, with good agreement with previous reports (75, 138). With the increase of the magnetic field, another peak appears in the spectrum at the energy ∼14 meV below the X_B state. This feature is assigned to the spin-forbidden excitons $X_{D/G}$, which are brightened by the in-plane magnetic field. According to Eq(3.1), this line should correspond to both grey and dark excitons. However, due to the broad inhomogeneous linewidth in the investigated samples (with the linewidth of $X_{D/G}$ of around 5 meV), it is not possible to resolve the small splitting δ expected between grey and dark states. This splitting, however, can be probed when the linear polarisation of the emitted signal is analysed, as the linear polarisation of the emission from grey and dark components are perpendicular to each other (80).

To confirm the assignment of the observed line as due to grey and dark states, the intensity ratio between this line and the X_B peak should be analysed. It is expected that in the case when splitting between the dark and bright states is significantly larger than thermal energy $|\Delta_{D-B}| >> k_B T$, the ratio of the intensity of the dark state brightened by the magnetic field and intensity of the bright state should follow simple quadratic law: $I_{D/G}/I_B \propto \mathbf{B}_{\parallel}{}^2$ (66, 120). As presented in Fig. 3.3, this law describes very well the measured intensity ratio $I_{D/G}/I_B$, being an indication of the dark character of the observed line.

To obtain the energy splitting between grey and dark excitons, additional measurements of the PL spectrum dependence on the angle of the linear polarisation analyser were performed and are presented in Fig. 3.4. Note that the angle indicated on the axis is relative to the experimental setup, not to the direction of the in-plane field. As the emission from the grey and dark excitons are perpendicular to each other linear polarisation, the energy spitting between these states was determined from the difference between the highest and lowest observed emission energy. This splitting of $\delta = 300$ μeV is twice lower than the one observed in the tungsten-based MLs (80, 134). This finding is a bit confusing, as the binding energies of molybdenum based MLs are normally higher than those in tungsten-based materials (79), so one could expect the same for the dark and grey excitons energy splitting, which is related to the exchange interaction. This

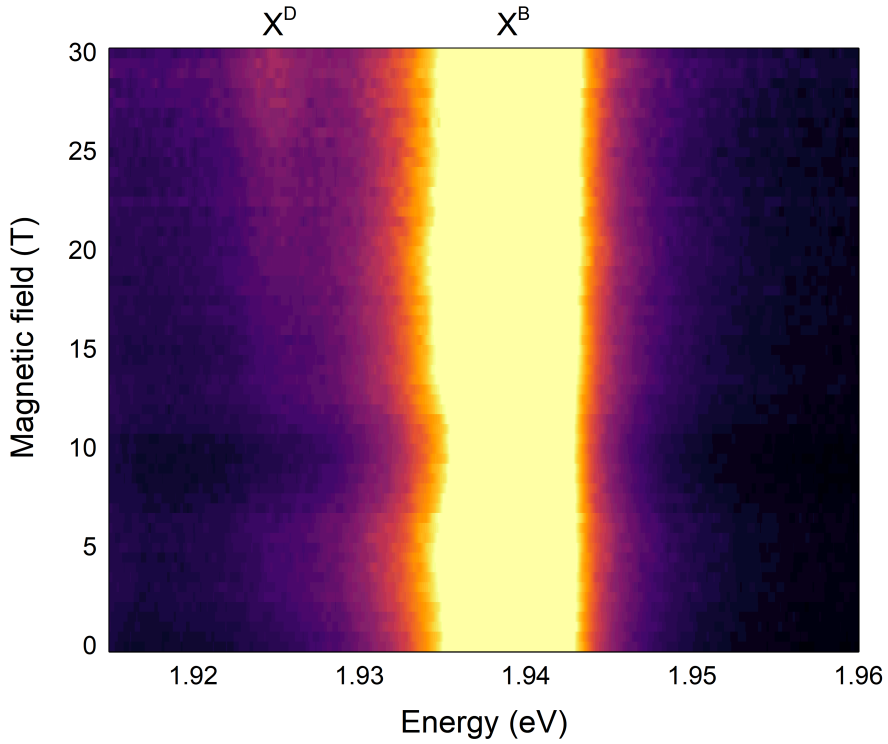

Figure 3.2: Color map of the variation of the PL intensity of the MoS_2 monolayer encapsulated in hBN as a function of $\mathbf{B}_{||}$. Each spectrum was normalized by the intensity of the bright exciton X_B.

shows that the relation between the magnitude of the direct and exchange Coulomb interactions is not straightforward.

Analogous measurements of the PL spectrum dependence on the in-plane magnetic field were also performed for the $MoSe_2$ monolayer encapsulated in hBN. This time, as shown in Fig. 3.5, the brightened dark and grey exciton states $X_{D/G}$ lie above bright exciton X_B. Similarly to the case of the MoS_2 ML the broadening of the $X_{D/G}$ line does not allow to resolve X_D and X_G separately and determine fine splitting δ. Another obvious difference between $MoSe_2$ and MoS_2 comes from the fact that in molybdenum diselenide bright and dark states significantly change their energies when a magnetic field is applied. In contrast, in molybdenum disulfide no such change can be resolved. This is the result of the relatively small energy difference between bright and dark states.

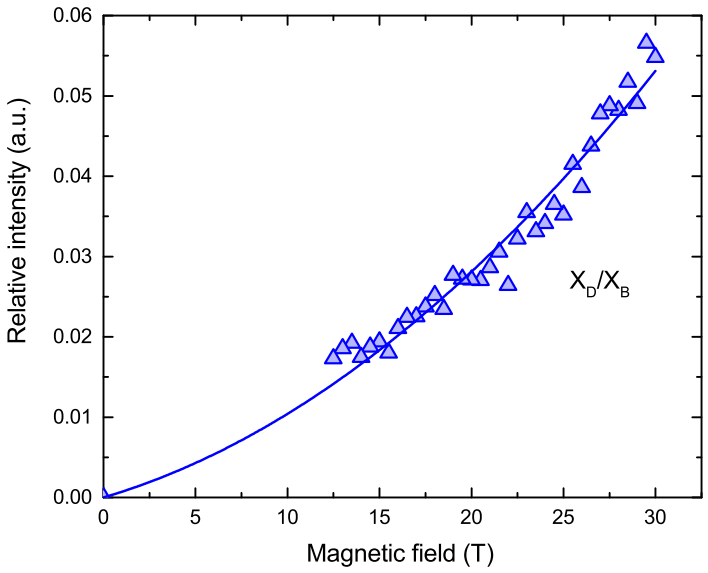

Figure 3.3: Relative intensity $X_{D/G}/X_B$ in the MoS_2 monolayer encapsulated in hBN as a function of $\mathbf{B}_\parallel$. The solid lines correspond to the fits obtained from the model described in the text.

According to the Eq.(3.1) and Eq.(3.3), in a simplified approach assuming $\delta = 0$, the energies of the dark and bright states as a function of an in-plane magnetic field can be described by following equations:

$$E_{D/G} = \frac{\Delta_{D-B}}{2} + \frac{1}{2}\sqrt{\Delta_{D-B}^2 + (\mu_B g_\parallel \mathbf{B}_\parallel)^2}, E_B = -\frac{\Delta_{D-B}}{2} - \frac{1}{2}\sqrt{\Delta_{D-B}^2 + (\mu_B g_\parallel \mathbf{B}_\parallel)^2}. \tag{3.4}$$

When $|\Delta_{D-B}| >> \mu_B g_\parallel {\mathbf{B}_\parallel}^2$, no energy change with application of in-plane magnetic field is observed, as in MoS_2 ML. In the case of MoS_2 ML, however, the Δ_{D-B} is smaller by order of magnitude, allowing the observation of the Zeeman energy shift.

To probe the magnetic field influence on the dark and bright states in a more qualitative way, the measured spectral lines were fitted by Lorentzian functions, allowing the extraction of the energies and amplitudes of the transitions. In Fig. 3.6(a), the energies of the dark and bright states along with the best fits with Eq.(3.4) are presented. From this fits the dark-bright energy splitting $\Delta_{D-B} = 1.4\,\text{meV}$ and in-plane

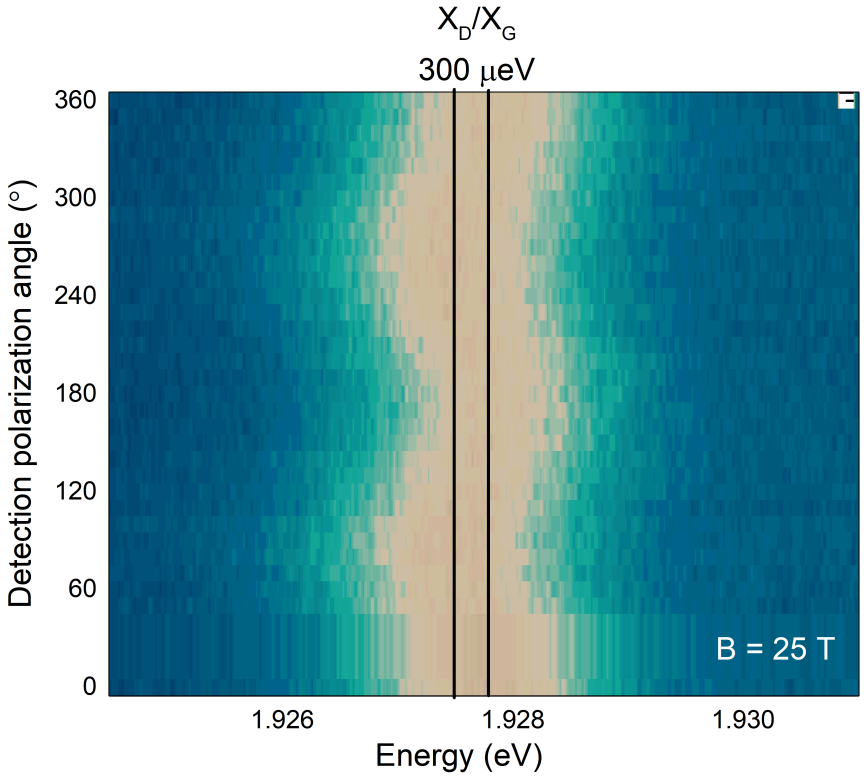

Figure 3.4: Angular dependence of the linearly polarised photoluminescence spectrum of the $X_{D/G}$ line in the MoS_2 monolayer encapsulated in hBN measured at the in-plane magnetic field of $\mathbf{B}_{\parallel} = 25$ T. The solid lines mark the extracted energies of the dark and grey excitons. The energy splitting is also indicated.

g-factor $g_{\parallel} = 2.0$ were extracted. These values are in excellent agreement with similar measurements recently reported (136).

As previously noted, the quadratic increase of the relative intensity $I_{D/G}/I_B$ can be a strong indication of the brightening effect on the dark state. However, this simple quadratic law works only if $|\Delta_{D-B}| >> k_B T$. As in the case of $MoSe_2$ monolayer these values are comparable, one has to take the thermal distribution into account, which results in following relation: $I_{D/G}/B \propto \mathbf{B}_{\parallel}{}^2 e^{-\Delta_{D-B}(\mathbf{B}_{\parallel})/k_B T}$. The relative amplitude $I_{D/G}/B$ obtained from the measurements is presented in Fig. 3.6(b) along with the best fit to the described relation. The temperature obtained $T = 10$ K is more than twice as high as expected in our setup, but that could be the result of the local heating of

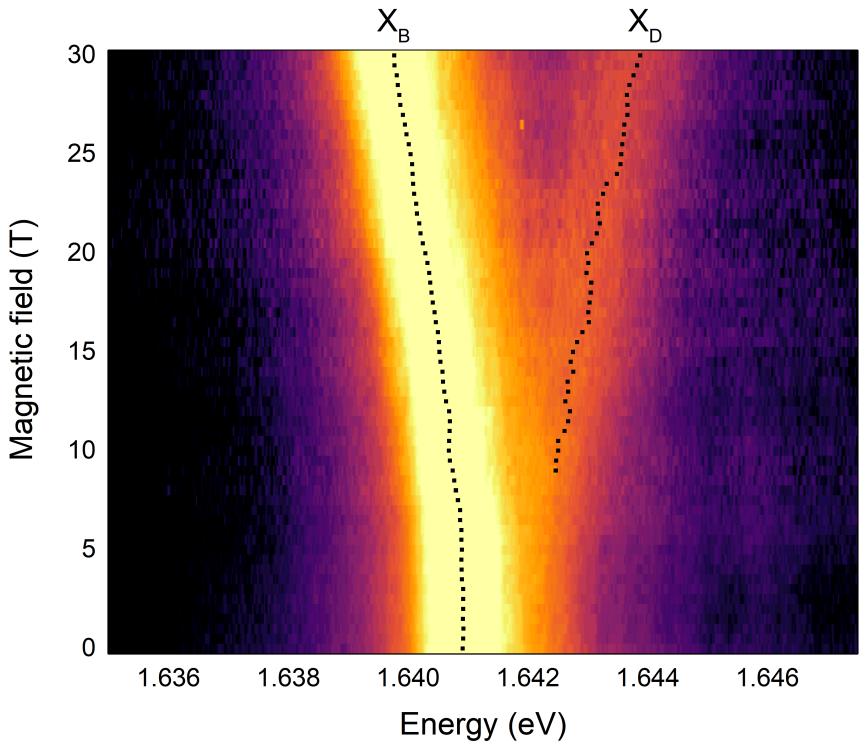

Figure 3.5: Color map of the variation of the PL intensity of the $MoSe_2$ monolayer encapsulated in hBN as a function of $\mathbf{B}_{\parallel}$. Each spectrum was normalized by the intensity of the bright exciton X_B. Black dots represents the energies of $X_{D/G}$ resonances retrieved from the spectrum by fitting two Lorentzian functions.

the sample by the excitation beam. The good agreement between the data and models for both energies and intensities of observed lines confirms the assignment of the higher energy line as the dark state is brightened by the magnetic field.

3.3.2 Magneto-photoluminescence in tilted magnetic field

Additional information about the dark states can be obtained in an out-of-plane magnetic field. However, due to their lack of interaction with the optical field, they cannot be observed in such geometry. To overcome that obstacle, the tilted-field geometry was employed, which is Faraday configuration with the sample's plane tilted by 45°. In such geometry, the in-plane and out-of-plane components of the magnetic field vector

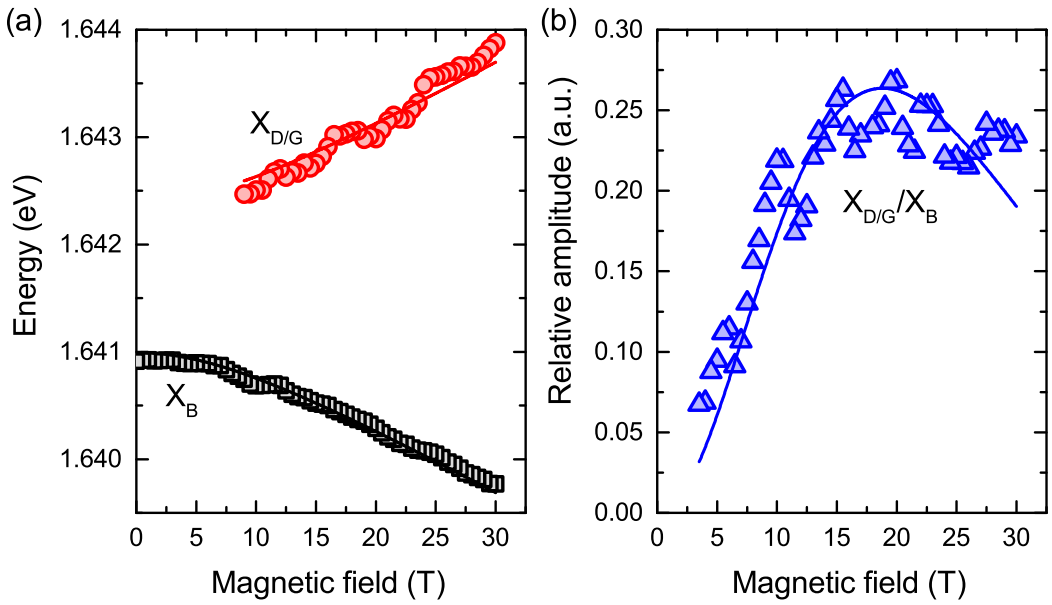

Figure 3.6: (a) Energy of dark $X_{D/G}$ and bright excitons X_B and (b) relative intensity $X_{D/G}/X_B$ in the $MoSe_2$ monolayer encapsulated in hBN as a function of $\mathbf{B}_{\parallel}$. The solid lines correspond to the fits obtained from the models described in the text.

have the same modulus. The in-plane component, as shown before, allows transferring of optical activity from bright to dark states, making them observable in photoluminescence experiments, while the out-of-plane component leads to Zeeman shifts of the bands' energies. As a result, dark and grey states change their energies according to their out-of-plane g-factor. Hence the tilted-field experiment allows determining this parameter.

The low temperature ($T = 4.2$ K) photoluminescence spectra of MoS_2 ML encapsulated in hBN as a function of a total magnetic field from $\mathbf{B} = 0$ T to 30 T in tilted-field configuration is presented as the false-colour map in Fig. 3.7. Again, at $\mathbf{B} = 0$ T only bright state X_B can be observed. With the increase of the total magnetic field, for $\mathbf{B} > 17$ T, two additional lines appear below bright exciton. These lines are attributed to the initially dark and grey states, which by application of the magnetic field are mixed with X_B states and their energy is modified due to the out-of-plane component of the magnetic field, according to Eq.(3.2). It should be noted that also the splitting of X_B into X_B^+ and X_B^- is expected, as the out-of-plane magnetic field should split the energies of the intravalley bright excitons. This is not observed as the broad linewidth

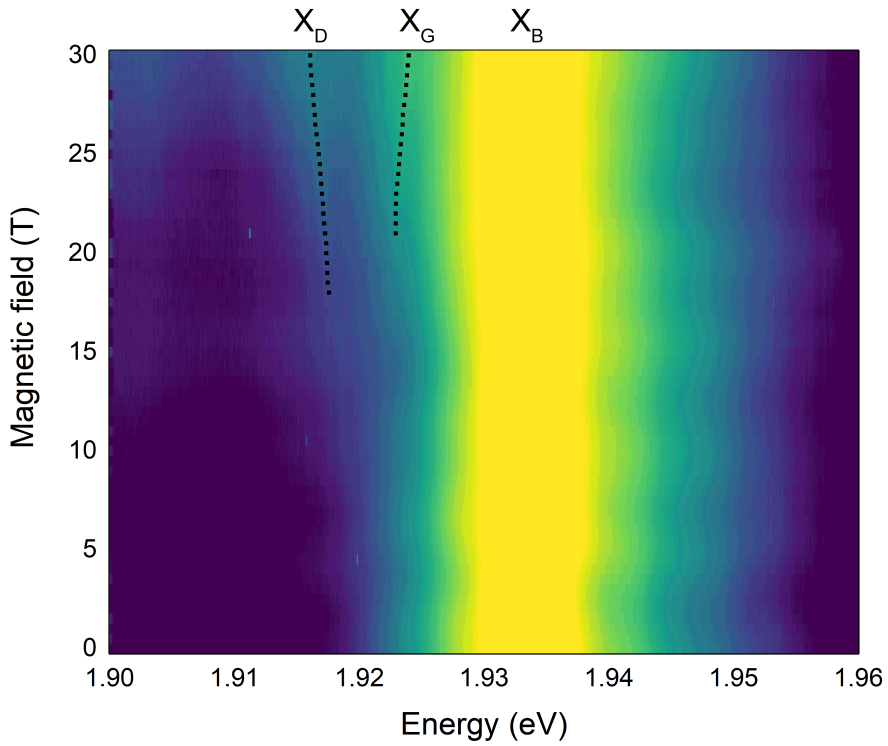

Figure 3.7: Color map of the variation of the PL intensity of the MoS_2 monolayer encapsulated in hBN as a function of total magnetic field $\mathbf{B}$ in tilted-field geometry. Each spectrum was normalized by the intensity of the bright exciton X_B. Black dots represents the energies of X_B and $X_{D/G}$ resonances retrieved from the spectrum by fitting two Lorentzian functions.

of X_B together with expected small g-factor of bright states (75, 79) does not allow to resolve intravalley bright components.

The energies of X_D and X_G states as a function of total magnetic field are presented in the Fig. 3.8. To model these energies with aforementioned model one has to add all three parts of Hamiltonian: exchange (Eq.(3.1)), in-plane (Eq.(3.3)) and out-of-plane (Eq.(3.2)). However, as already shown, the in-plane part does not affect the energies of dark states due to the large energy splitting between dark and bright states Δ_{D-B}. Hence in a simple approach only Eq.(3.1) and Eq.(3.2) can be taken into account. Then, these energies can be described by following equations:

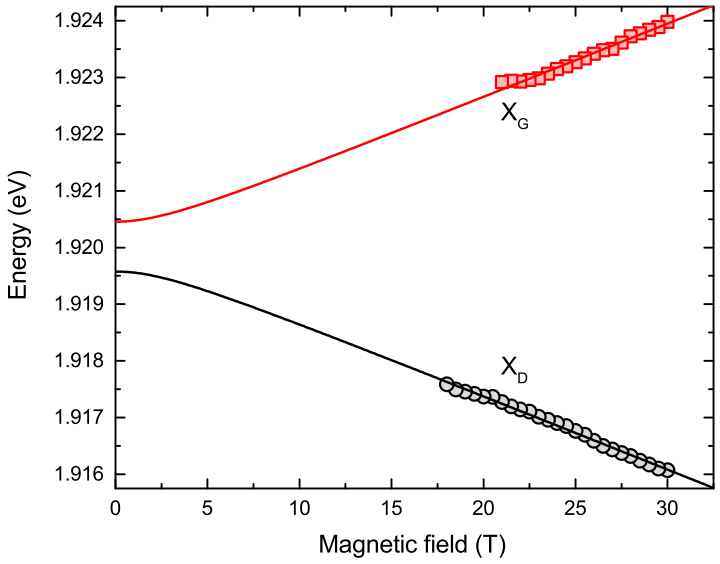

Figure 3.8: The energy of X_D and X_G in the MoS_2 monolayer encapsulated in hBN as a function of total magnetic field $\mathbf{B}$. The solid lines correspond to the fits obtained from the model described in the text.

$$E_G = \frac{1}{2}\sqrt{\delta^2 + (\mu_B g_D \mathbf{B}_\perp)^2}, E_D = -\frac{1}{2}\sqrt{\delta^2 + (\mu_B g_D \mathbf{B}_\perp)^2}. \tag{3.5}$$

The best fits using this equation to the observed energies are also presented in Fig. 3.8. From these fits, the g-factor of dark excitons was obtained to be equal to $g_D = 6.5$. Note that labelling of lines as X_G and X_D is accurate only at 0 T, as these states are being mixed by the magnetic field.

Similar measurements were performed also for $MoSe_2$ ML, as presented in the Fig. 3.9. At zero magnetic field only bright state X_B can be observed. When the magnetic field is applied, the single line splits into four distinct ones, which can be clearly resolved for a total magnetic field above 15 T. Below this field, the splitting is comparable with the linewidth of the observed transitions. The energies of the features obtained by fitting with Lorentzian functions are also presented in Fig. 3.9 as black dots. Splitting into four lines results mainly from the Zeeman shift induced by the out-of-plane field component of both intravalley bright and dark excitons. However, as in

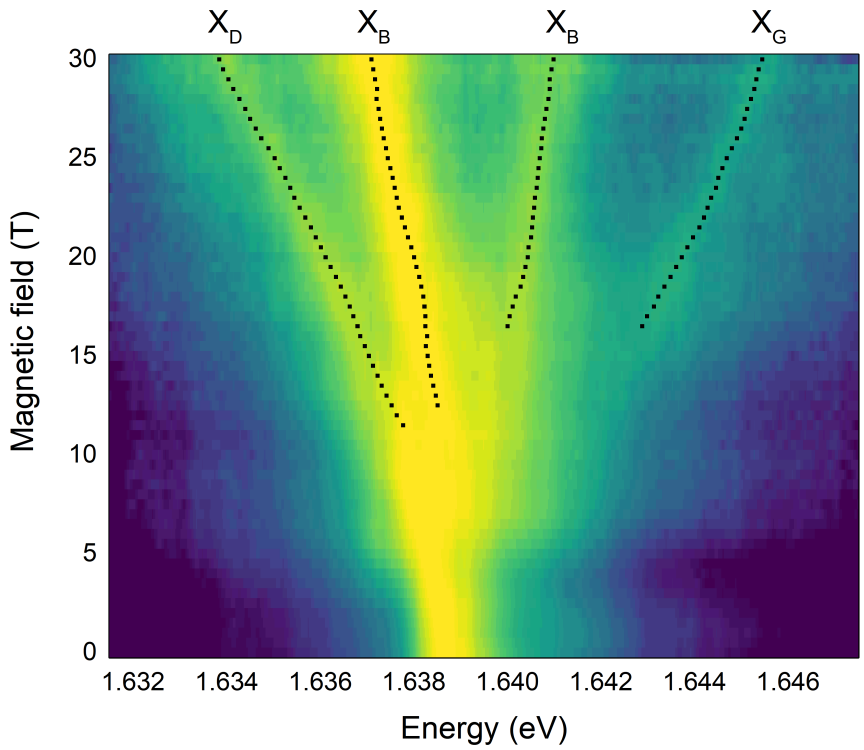

Figure 3.9: Color map of the variation of the PL intensity of the $MoSe_2$ monolayer encapsulated in hBN as a function of total magnetic field **B** in tilted-field geometry. Each spectrum was normalized by the intensity of the bright exciton X_B. Black dots represents the energies of X_B and $X_{D/G}$ resonances retrieved from the spectrum by fitting two Lorentzian functions.

the case of $MoSe_2$ ML, bright and dark excitons are close in energy, dark-bright mixing induced by in-plane component is strong and also has to be taken into account, as it leads to apparent energy repelling of the lines. Thus, no simple formula for the final energy of the states can be provided, and one has to diagonalize full Hamiltonian (sum of Eq.(3.1), Eq.(3.3) and Eq.(3.2)) to model the evolution of the transition energies in the field.

In the full Hamiltonian the interaction of excitons with magnetic field is driven by out-of-plane g-factors of bright (g_B) and dark (g_D) states and in-plane electron g-factor $g_\parallel$. The energy shift in a tilted magnetic field is mainly determined by g_B and g_D with additional, smaller correction resulting from mixing between dark and bright states via

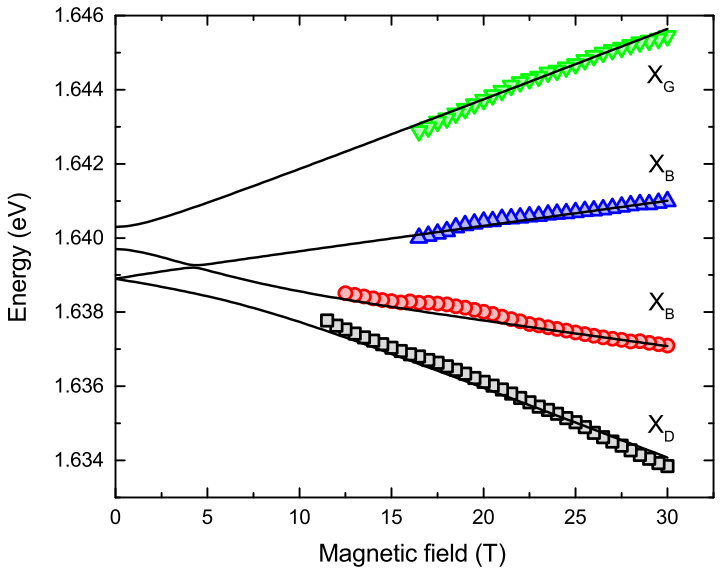

Figure 3.10: The energy of X_D and X_G in the $MoSe_2$ monolayer encapsulated in hBN as a function of total magnetic field **B**. The solid lines correspond to the fits obtained from the model described in the text.

$g_\parallel$. Now, using the $\Delta_{D-B} = 1.4\,\text{meV}$ and $g_\parallel = 2.0$ extracted from Voigt experiments, one can fit simultaneously the numerically obtained eigenvalues of full Hamiltonian to the field dependence of the energy of all four exciton lines. The result of such fitting along with the energies of observed transitions is shown in Fig. 3.10. The best fit gives very good agreement between the measured data and the theoretical model and yields g-factors of bright and dark excitons equal of $g_B = -4.0$ and $g_D = -8.6$. As the linewidth of the excitons prevents from extracting energies of the states at low fields, the value of the exchange splitting of dark states δ cannot be obtained - with lack of low field data, the fitting procedure is insensitive to the value of δ. For calculations presented in the Fig. 3.10 splitting of $\delta = 0.6$ meV was assumed. It should be noted that labelling of lines as X_G, X_B, X_B and X_D is accurate only at 0 T, as in tilted magnetic field all the states are mixed.

Table 3.1: Summary of exciton fine structure parameters and g-factors measured for S-TMDs monolayers encapsulated in hBN.

	MoS_2	$MoSe_2$	WS_2	WSe_2
Δ_{D-B} (meV)	-14	1.4 1.5(136)	-40(134)	-40(81, 139) -38(80)
δ (meV)	0.3	< 1	0.5(134)	0.6(80, 82)
g_B	-1.7(75)	-4.0	-4.0(79)	-4.25(76) -4.1(80)
g_D	-6.5	-8.6	-	-9.4(82) -9.6(80)
$g_{\parallel}$	-	2 2(136)	-	2.7(80)

3.4 Discussion

The measurements described above allowed for the first experimental determination of the dark-bright exciton energy splitting Δ_{D-B} in MoS_2 and out-of-plane g-factors of dark excitons g_D in MoS_2 and $MoSe_2$. The out-of-plane g-factor of bright exciton g_B and in-plane g-factor of electrons $g_{\parallel}$ in $MoSe_2$ were also obtained, while the upper bounds for the values of grey-dark exciton splitting δ were provided. All these parameters are summarized in Tab. 3.1, along with the values obtained in previous works and for tungsten-based MLs. Now let's discuss the obtained parameters' values and their potential consequences.

The measured value of the dark-bright exciton splitting in MoS_2 ML encapsulated in hBN of $\Delta_{D-B} = -14$ meV has significant repercussions. Firstly, it shows that the monolayer of MoS_2 is optically dark, in contrast with theoretically predicted small but positive spin-orbit splitting $\Delta_{CB} \sim 3$ meV(52, 57, 117). This suggests that not only spin-orbit splitting of conduction band determines the energy ordering of bright and dark excitons, but that also the difference of exciton binding energies is important. The difference in binding energies stems from the difference in masses of electrons' forming dark and bright states and also from the exchange interaction between electron and

hole, which differs for bright and dark states. One can say that dark-bright exciton splitting is equal to: $\Delta_{\mathrm{D-B}} = \Delta_{\mathrm{CB}} + \Delta_{\mathrm{M}} + \Delta_{\mathrm{ex}}$. This shows that the $\Delta_{\mathrm{M}} + \Delta_{\mathrm{ex}}$ part has to be negative, equal to over a dozen meVs. Similar difference between $\Delta_{\mathrm{D-B}}$ and Δ_{CB} we see also in $MoSe_2$ (in line with previous results(136)) and was observed in tungsten-based materials (80, 82, 134). One can estimate the value of Δ_{M} using the formula for exciton binding energy from Ref. (9) and electrons' masses in conduction band from Ref. (52), which lead to $\Delta_{\mathrm{M}} \sim -8$ meV. Now, combining the values of $\Delta_{\mathrm{D-B}}$, Δ_{CB} and Δ_{M} the exchange difference of $\Delta_{\mathrm{ex}} \sim -9$ meV can be deduced. This suggests (assuming the correctness of the used theoretical calculations) that the short-range exchange interaction could also have a significant impact on the ordering of bright and dark states to the one of spin-orbit splitting of the conduction band and binding energy difference, which in turn could have pivotal consequences for the trion fine structure (140).

The obtained results also show that it is not clear whether MoS_2 ML encapsulated in hBN can be simply interpreted either as "bright" material, as it has been so far assumed, or as a "darkish" material. One of the characteristics of S-TMDs monolayers considered as "darkish", such as WS_2 and WSe_2, is low photoluminescence yield at low temperatures, which increases with the temperature as the bright states are thermally activated(70, 119, 120, 121, 122). On the other hand, the "bright" monolayers such as $MoSe_2$ and $MoTe_2$, but also MoS_2, show stronger photoluminescence at low temperatures, as compared to "darkish" ones, while the photoluminescence intensity decreases with the increase of temperature(70, 119, 120, 141). It was assumed that this difference was a result of the energy ordering of dark and bright excitons. It is consistent with the now known fine structure of WS_2, WSe_2 and $MoSe_2$, but not with the $\Delta_{\mathrm{D-B}} = -14$ meV of MoS_2 presented here. Moreover, it shows that temperature dependence of PL intensity cannot be used to distinguish between "bright" and "darkish" materials, as in the case of MoS_2 ML, the observed tendency might be the result of non-trivial relaxation processes between bright and dark and its interplay with the non-radiative recombination.

The difference in the amplitude of the valley polarisation of excitons is another property of S-TMD monolayers that was initially explained by the dark and bright exciton energy ordering(142). In "darkish" MLs (WS_2 and WSe_2) strong valley polarisation can be achieved(143, 144, 145, 146, 147), and also in MoS_2(63, 64, 148, 149), while

in "bright" $MoSe_2$ and $MoTe_2$ valley polarisation is weak(141, 150, 151) (except for quasi-resonant excitation in the case of $MoSe_2$(152)). More detailed explanation, which suggests that the crossing of bright and dark excitons dispersion curves along with the Rasha effect resulting from local fluctuations of the electric field may cause fast spin relaxation, was recently proposed(153). The values of Δ_{D-B} measured for MoS_2 and $MoSe_2$ MLs are in good agreement with this theory. Relatively strong splitting of $\Delta_{D-B} = -14$ meV in MoS_2 and larger effective mass of dark excitons as compared with bright ones lead to the lack of crossing of their dispersions, as it is also in the case of WS_2 and WSe_2, allowing to achieve strong valley polarisation in this material under circularly polarised excitation. On the other hand, small splitting of $\Delta_{D-B} = 1.4$ meV combined with the dark state being above bright one in energy could lead to the crossing of their dispersions, leading to fast spin relaxation, making it difficult to achieve valley polarisation in $MoSe_2$ ML.

Although in all WS_2, WSe_2 and MoS_2 MLs, dark excitons states are of lower energies than the bright excitons states, there is one more striking difference between these materials. While the grey excitons in tungsten-based MLs were observed without in-plane magnetic field by measurement of the in-plane emission(81) or by the use of high numerical aperture objectives(80, 81, 82, 134), similar results were never obtained for the MoS_2 MLs. Furthermore, the magnitude of the in-plane magnetic field required to brighten the dark states in molybdenum disulfide (more than 14 T) is much larger than the one required to observe them in tungsten-based MLs (just a few teslas (80, 82, 134)). This difference could be speculatively explained by the lower relative population of dark excitons to bright excitons and also by the lower oscillator strength of transitions involving the grey excitons. Lower population could be explained by the fact that the dark-bright splitting in MoS_2 $\Delta_{D-B} = -14$ meV is much lower than the energy of optical phonon $E_{\Gamma^5} = 36$ meV, which is responsible for scattering from bright to dark states, while in the tungsten-based systems Δ_{D-B} (see Tab. 3.1) is larger than E_{Γ^5}(126). The higher value of Δ_{D-B} should also imply a higher relative population due to the thermal distribution. The smaller oscillator strength could be explained by noticing that weaker SOC in MoS_2 compared to tungsten-based MLs may lead to a weaker oscillator strength of the grey exciton, as it is related to the spin-orbit mixing with higher energy bands(81, 118).

The exact value of the dark-grey energy splitting δ can be obtained by the measurement of linearly polarised emission in in-plane magnetic field(80, 134) or by measurements of PL in out-of-plane magnetic fields if grey exciton can be observed at 0 T(80, 82). Here the former approach was used only in the case of MoS_2. This allowed extracting the splitting of $\delta = 0.3$ meV. Such measurements were performed for $MoSe_2$ monolayer. However, higher bounds could be put on this value, estimated from the linewidth of the dark/grey line measured in the in-plane field configuration. These estimations lead to the higher bounds of $\delta < 1$ meV. These bounds are consistent with values measured for WS_2 and WSe_2 (see Tab. 3.1).

The out-of-plane g-factor of bright exciton $g_B = 4.0$ of $MoSe_2$ was also obtained from the measurements in the tilted field configuration. It's value is consistent with those measured for WS_2 and WSe_2 (see Tab. 3.1). The splitting of the bright exciton in the same configuration in MoS_2 was too small to resolve two separate lines properly. This is consistent with the relatively small g-factor of $g_B = 1.7$, previously measured in this material(75). The measured out-of-plane g-factors of dark exciton of $g_D = 6.5$ for MoS_2 and $g_D = 8.6$ for $MoSe_2$ are significantly higher than those of bright excitons, which is also the case in WSe_2(80, 82). The in-plane g-factor $g_{\parallel}$, responsible for dark-bright mixing in an in-plane magnetic field, was estimated to be equal to $g_{\parallel} = 2.0$, in good agreement with previous works(136).

In a simple model g-factors of bright and dark excitons can be separated into tree contributions of electrons and holes: spin g_s, orbital g_{d^2} and valley g_v(154). In a first approximation one can assume that the valley contribution of hole and electrons is the same, which means that the exciton g-factor depends only on spin orbital contributions, which can be approximated by: $g_s \sim 1$ and $g_{d^2} \sim 2$. In this model g-factors of bright exciton can be written as $g_B = 2g_{d^2} \sim -4$, of dark exciton as $g_D = 2(g_{d^2}+2g_s) \sim -8$ and in-plane g-factor as $g_{\parallel} = -2g_s \sim 2$. This oversimplified model works quite well with the values obtained for $MoSe_2$, WSe_2 and WS_2 (compare with Tab. 3.1). However, it is far of the values known for MoS_2, One can say that in this material the valley contribution cannot be neglected, which leads to $g_B = 2g_{d^2} + g_v$ and $g_D = 2(g_{d^2} + 2g_s) + g_v$. From $g_B = -1.7$ one can deduce $g_v = 2.3$ and then $g_D = -5.7$, which is not much different from the value $g_D = -6.5$ obtained in the experiment. However, this shows that to precisely model g-factors of excitons of MoS_2 this simplified model is not sufficient

and more sophisticated approach is needed, as presented in some recent theoretical works(155, 156).

3.5 Conclusions

The measurements of magneto-photoluminescence in transverse and tilted magnetic fields up to 30 T performed on high-quality samples of MoS_2 and $MoSe_2$ monolayers encapsulated in hBN allowed the detailed studies of the exciton fine structure in these materials. Most importantly, it has been proven that in MoS_2 monolayer, dark exciton lies energetically below the bright exciton. Energy splitting between dark and bright excitons and their g-factors were determined. These fundamental parameters are crucial elements to understand the optoelectronic and valley properties of these 2D semiconductors.

4

Rydberg series of dark excitons in WSe_2 monolayer

4.1 Introduction

The observation of the ground state of dark excitons provides much useful information about the probed system, as discussed in the previous chapter. It does not, however, allow for the extraction of the amplitude of the spin-orbit splitting of the conduction band (Δ_{CB}), which is crucial for the interpretation of optical and transport experiments. It is due to the unknown magnitude of the binding energies difference of bright and dark excitons states that Δ_{CB} cannot be easily extracted. In this chapter, it will be presented how Δ_{CB} can be obtained for the WSe_2 ML from the comparison of the energies of not only the ground states but the whole Rydberg series of both bright and dark excitons.

The idea driving this project is presented schematically in Fig. 4.1. In the single-particle picture (Fig. 4.1(a)), three electronic bands (per each K^+ and K^- valley) are needed to be taken into account when primary allowed and forbidden transitions are being considered: one valence band and two conduction band subbands, separated due to the spin-orbit splitting. The allowed (optically active) band-to-band transitions with the change of the total angular momentum $j_z = \pm 1$ happen in WSe_2 between the valence band and the upper conduction subband. Those between the valence band and lower conduction subband are characterized by the $j_z = 0$ and hence are not optically active (spin-forbidden) under conventional conductions/configurations(81). However, these transitions are weakly allowed only when the interacting photons have some component

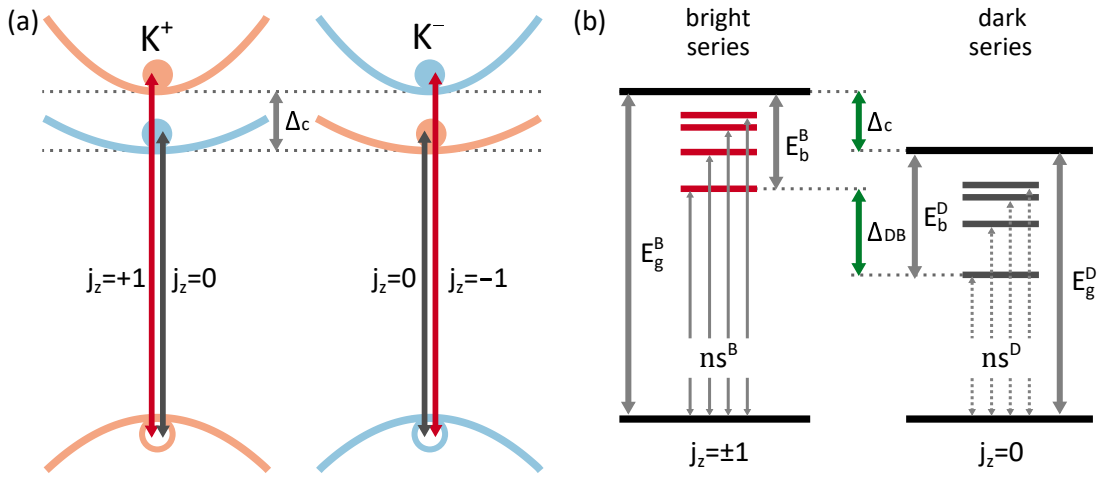

Figure 4.1: (a) Schematic representation of the interband transitions in a single-particle picture. The spin-up and spin-down states are depicted as light orange and light blue parabolas, respectively. The red arrows represent optically active (bright) transitions at K^+ and K^- valleys, while dark grey arrows represent optically inactive (dark) transitions. The conduction band spin-orbit splitting (Δ_{CB}) is shown as a light grey arrow. (b) The diagram of energy levels of excitonic transitions: series of bright (ns^B) and dark (ns^D) resonances. The horizontal red and dark grey lines represent bright and dark excitonic levels, respectively. The light grey arrows depict the band gaps for bright and dark excitons ($\mathrm{E}_g^{B/D}$) and the binding energies of the ground states of bright and dark excitons ($\mathrm{E}_b^{B/D}$). The green arrows represent the energy splitting between ground states of bright and dark excitons (Δ_{DB}) and the conduction band spin-orbit splitting (Δ_{CB}).

of the out-of-plane polarisation. The energy difference between these two transitions is defined strictly by the amplitude of the spin-orbit splitting of the conduction band.

While this single-particle picture is informative and frequently used to discuss the optical transitions in TMDs, it does not capture the electron-hole Coulomb interactions, so the crucial here excitonic effects are missing in it. As was already mentioned in the previous chapter, those effects are also significant when the bright and dark excitons are being considered. More relevant in that case is the two-particle picture (Fig. 4.1(b)). Here, two distinct excitonic Rydberg series ns can be identified: bright excitons X^B, related to the allowed band-to-band transition, and the dark excitons X^D, related to the forbidden transitions. The energy difference Δ_{DB} between ground states of X^B and X^D is defined by both the amplitude of spin-orbit splitting of conduction band Δ_{CB} and the difference of the binding energies of bright and dark excitons: $\Delta_{\mathrm{DB}} = \Delta_{\mathrm{CB}} + (E_b^D - E_b^B)$, where the binding energy difference is due to the difference in masses

of the electrons involved in bright and dark excitons and the exchange interactions(52), as the spin-configurations for these two states are not the same(118, 137, 157). However, for the high values of principal quantum number n, as the binding energies decrease, the energies of excitonic states converge to the bandgap energies. Now, as the bandgap energies for bright and dark excitons are the same as the allowed and forbidden band-to-band transitions energies, respectively, in the single-particle picture, the difference in the band gaps yields the amplitude of the spin-orbit splitting in the conduction band: $\Delta_{\mathrm{CB}} = E_g^B - E_g^D$. The values of the band gaps related to bright and dark excitons can be extracted from the observation of their Rydberg series (9, 76).

The excitonic states of the bright Rydberg series can be relatively easily traced in the luminescence experiments(9, 77, 78, 158). The excited states of the dark excitons, on the other hand, were not observed up to now. Moreover, there are only a few reports on the observation of the dark excitons in any compounds (159, 160, 161) and none of them by the photoluminescence. Below, the low-temperature magneto-optical study of the Rydberg series of bright and dark excitonic states in a WSe_2 monolayer is presented. The in-plane magnetic field is used to couple bright and dark excitons and by so "brighten" the latter. States with principal quantum numbers n up to 4 were observed. The comparison of the energy diagrams of two excitonic series allowed us to extract the single-particle separation between spin-orbit-split conduction band subbands in this material.

4.2 Experimental results - Magneto-photoluminescence in in-plane magnetic field

The results of the low temperature (4.2 K) magneto-photoluminescence measurements carried out in in-plane magnetic fields up to 30 T on a WSe_2 monolayer encapsulated in hBN flakes are presented in Fig. 4.2 for selected values of magnetic fields. The lower energy range of the spectra (left panel of Fig. 4.2) contains a set of characteristic emission lines related to many different excitonic states such as indirect/inter-valley excitons and their phonon replicas and also more complicated excitonic complexes such as trions and biexcitons (162, 163, 164, 165, 166, 167). Here, the focus is only on the neutral bright and dark excitons, while the other transitions are beyond the scope of the work. The higher energy range of the spectra (right panel of Fig. 4.2) is composed

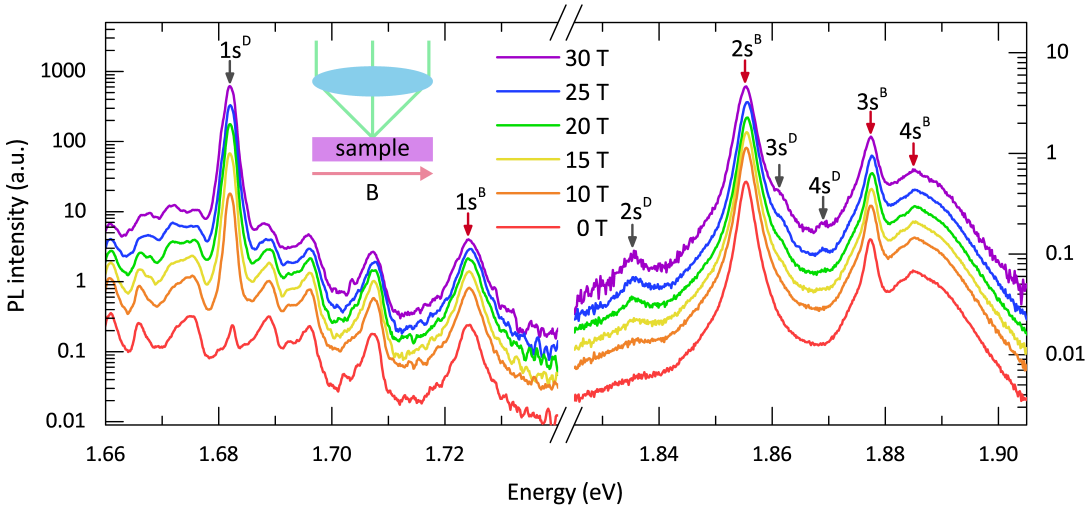

Figure 4.2: Low-temperature photoluminescence spectra measured at selected values of the in-plane magnetic field in the energy region of both ground (left panel) and excited states (right panel). Spectra were normalized to the $1s^B$ feature in the lower energy region and the $2s^B$ feature in the higher energy region and shifted vertically for clarity. Note that the intensity scales differ for these two regions. The inset schematically displays the "backscattering" Voigt geometry used in the experiment, where the excitation and the collected light beams are perpendicular to the sample plane.

of the excited excitonic states. First, let us consider the measured PL spectrum in the absence of the magnetic field. Based on the previous reports, the Rydberg series of neutral bright excitons with four distinct states $1s^B$, $2s^B$, $3s^B$ and $4s^B$ can be recognized (9, 76, 77, 78, 158). In the zero-field spectrum, also weak transition related to the ground state of the dark (grey) exciton $1s^D$ can be observed (80, 81, 82), thanks to the relatively large numerical aperture used in the experiment (80, 81, 82). It should be noted that since the polarisation of the signal was not controlled in the experiment and the used resolution did not allow to resolve grey and dark excitons, their small splitting ~ 0.7 meV for the ground states (80, 82) is disregarded and single dark exciton Rydberg series is referred to.

More crucial in that case is the change of the spectrum when the magnetic field ($B_{\parallel}$) is applied in the in-sample-plane direction. Two effects can be observed. Firstly, the intensity of the $1s^D$ state increases progressively with a magnetic field, by two orders of magnitude in the spectrum measured at $B_{\parallel}$=30 T. This is due to the transfer of the optical activity from the $1s^B$ state due to their mixing in the in-plane field. More

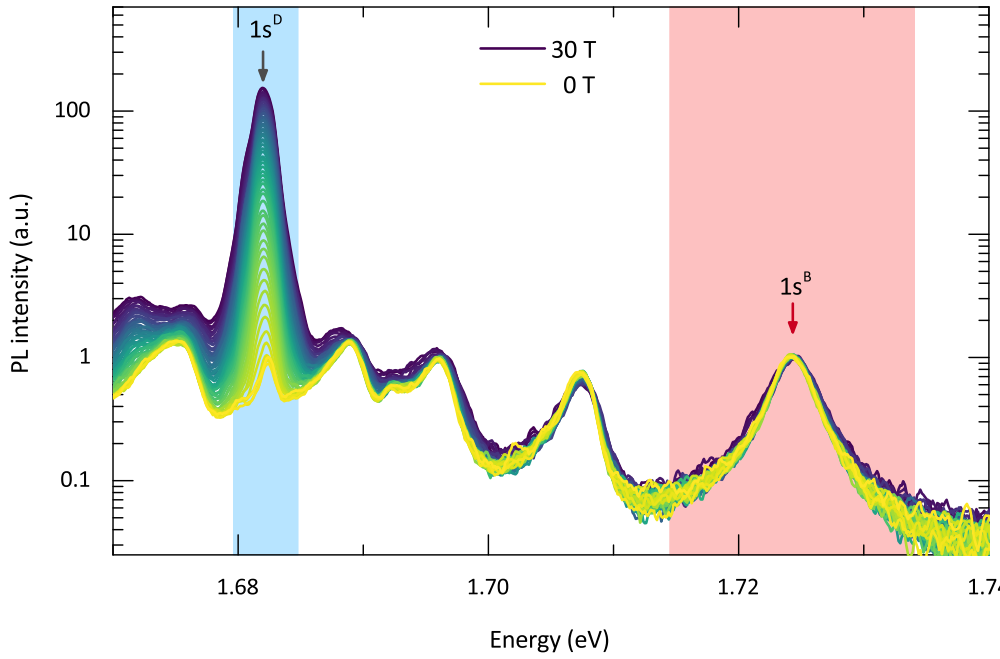

Figure 4.3: The low-temperature photoluminescence spectra measured at in-plane magnetic fields from 30 T to 0 T in the energy region of ground states. The spectra were normalized to $1s^B$ feature for clarity. The red/blue rectangles highlight the regions that were integrated to obtain the total PL intensity of $1s^B/1s^D$.

importantly, additional emission lines appear in the higher energy part of the spectrum in the vicinity of the PL peaks related to the excited states of dark excitons. These new peaks labelled as $2s^D$, $3s^D$ and $4s^D$ are attributed to the excited Rydberg states of the dark exciton.

In order to perform a qualitative analysis of the brightening effect of the Rydberg states of the dark exciton, the amplitudes and energies of the states have to be extracted from the measured spectra. The estimation of the energies of the ground states was straightforward, as those peaks were relatively well separated from the other emission lines. The intensities of the $1s^B$ and $1s^D$ states were obtained by integrating the area of these peaks. Fig. 4.3 shows the regions used for integration. As the edge of the area used for $1s^D$ slightly overlaps with the neighbouring emission line, the error for that area was estimated as the difference between the areas obtained for two regions– one that fully covers the emission line at 30 T, and the other that covers only $1s^D$ at 0 T.

The same approach could not be applied to the excited states, as some of these lines

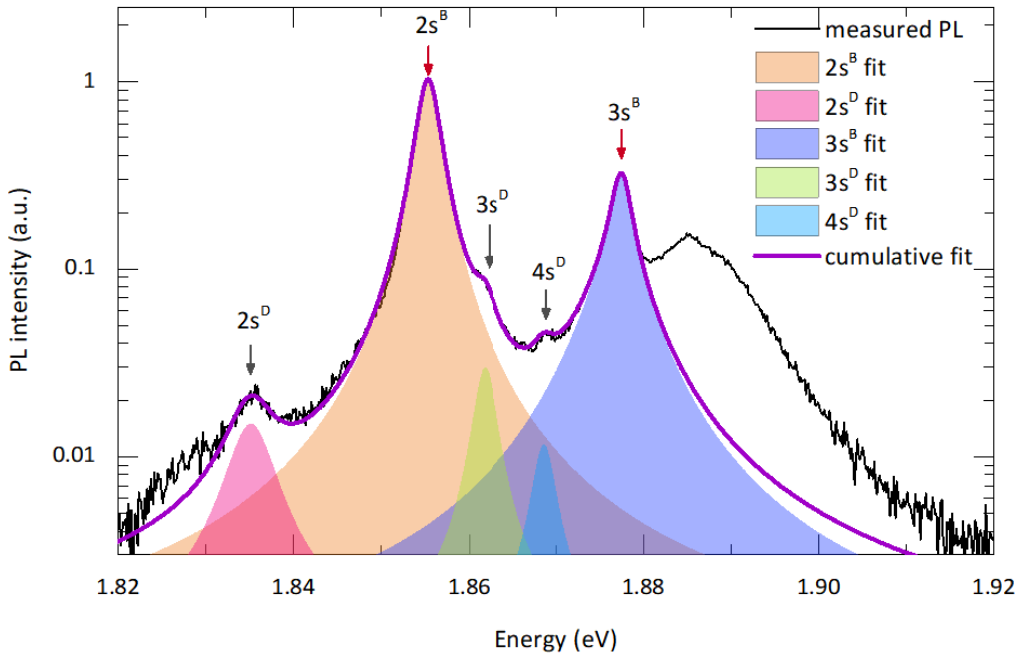

Figure 4.4: The low-temperature photoluminescence spectrum measured at 30 T in the energy region of excited states, along with the single peaks curves. The black line represents the measured spectrum, the intensities of excited bright and dark states are represented by coloured areas, while the cumulative curve is represented by the purple line. The same energies and linewidths of features were used to reproduce the spectra obtained at lower magnetic fields.

were significantly overlapping. Hence, the intensities and the energies were extracted by reproducing the region of interest of the spectra with multiple Lorentzian functions. Fig. 4.3 shows the result of such a procedure for the spectrum obtained at 30 T. The parameters used in this figure are listed in Tab. 4.1. The same energies and linewidths of the Lorentzian functions were then used to reproduce the spectra at lower magnetic fields.

4.3 Discussion

The amplitudes obtained from the analysis of the magneto-photoluminescence spectra were used to calculate the change of the relative intensity $I_D(n)/I_B(n)$ of dark states ns^D to those of bright states ns^B in a magnetic field. The relative intensity is presented

Table 4.1: List of the parameters used to reproduce the spectrum measured at 30 T in the energy region of excited states with Lorentzian functions. Note that the $3s^B$ peak required two Lorentzians to account for its asymmetric shape.

	$2s^D$	$2s^B$	$3s^D$	$4s^D$	$3s^B$
E0 (eV)	1.83511	1.85531	1.86183	1.86863	1.87676 1.87746
Linewidth (meV)	5.82	2.91	2.93	2.91	8.68 2.59
Amplitude (a.u.)	$1.2766{\cdot}10^{-4}$	$4.74{\cdot}10^{-3}$	$1.33741{\cdot}10^{-4}$	$4.86977{\cdot}10^{-5}$	$9.64564{\cdot}10^{-4}$ $1.02{\cdot}10^{-3}$

in Fig. 4.5 for n=1,2,3. As expected for the brightening effect in the low magnetic field regime $g_{\parallel}\mu_B B_{\parallel} << \Delta_{DB}$, the relative intensities follow roughly the quadratic increase with magnetic field $I_D(n)/I_B(n) = b_n^E B_{\parallel}^2$, with the exception of the ground state for magnetic fields $B_{\parallel}^2 > 20$ T. This deviation from the quadratic dependence could result from the shortened (due to the optical activation by magnetic field) dark exciton lifetime, which in turn leads to the decrease of the dark exciton population and hence the PL intensity. Thus only the data for $B_{\parallel}^2 < 20$ T was used to estimate the b_1^E. The obtained parameters are as follows $b_1^E = (69 \pm 6)10^{-2}$ T^{-2}, $b_2^E = (21 \pm 6)10^{-6}$ T^{-2} and $b_3^E = (7 \pm 2)10^{-5}$ T^{-2}. These parameters can also be estimated theoretically when the occupation difference of the bright and dark states is neglected, using formula (80):

$$b_n^T = \left[\frac{g_{\parallel}\mu_B}{2(E_n^B - E_n^D)}\right]^2, \tag{4.1}$$

where $g_{\parallel}$ is the in-plane g-factor, μ_B is the Bohr magneton (value of $g_{\parallel} = 2.71$ is used (80)), $B_{\parallel}$ represents the in-plane magnetic field, while $E_n^{B/D}$ denote the zero-field energies of bright and dark states, respectively, for given principal quantum number n. The parameters obtained this way are as follows: $b_1^T = 34{\cdot}10^{-7}$ T^{-2}, $b_2^T = 15{\cdot}10^{-6}$ T^{-2} and $b_3^T = 23 \cdot 10^{-6}$ T^{-2}. Whereas in the case the excited states (n=2,3) there is reasonable agreement between values obtained theoretically and experimentally, for the ground states the parameters differ by 5 orders of magnitude. Such enormous difference could be explained non-thermal population difference of optical excitations in a WSe_2

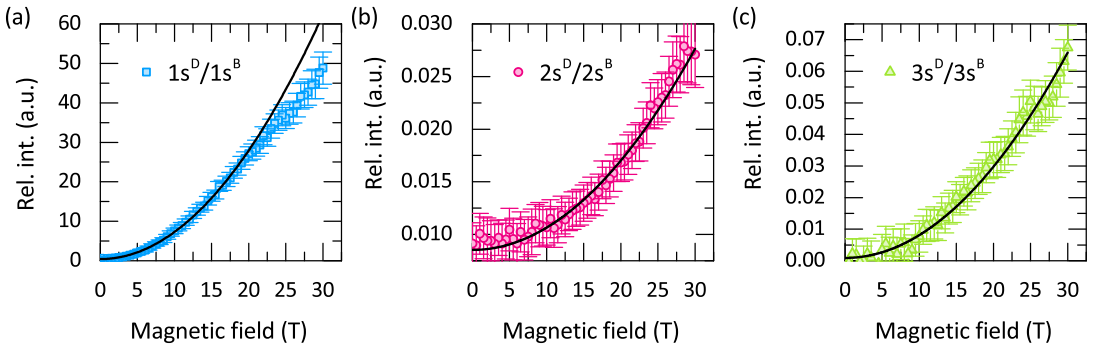

Figure 4.5: Relative intensities of dark states to bright states as a function of the in-plane magnetic field for (a) the 1s states (blue squares), (b) the 2s states (red circles) and c the 3s states (green triangles) along with parabolic curve fits (black lines) of the form $a + bx^2$. Note that in the case of 1s states, only data points from 0 T to 20 T were used for the fitting since, for higher fields, the relative intensity apparently starts to deviate from quadratic dependence.

monolayer. Nonetheless, the quadratic dependence of the relative intensities confirm the assignment of the emission lines appearing in the in-plane magnetic field to the excited states of dark Rydberg series.

Now let us focus on the main result, which is related to the energies of the bright and dark Rydberg series. As shown in Fig. 4.6, the energies of the n-series of bright and dark excitons follow the semi-empirical formula(9) nicely:

$$E_n^{D/B} = E_g^{D/B} - \frac{Ry^{D/B}}{(n+\delta)^2}, \tag{4.2}$$

where $E_g^{D/B}$ is the bandgap related to dark/bright excitons, associated to the lower/upper conduction band subband respectively and, $Ry^{D/B}$ should be in the first approximation identified with the effective Rydberg energy for the dark/bright exciton: $Ry^{D/B} = 13.6eV \cdot \mu^{D/B}/(\epsilon^2 m_0)$, where $\mu^{D/B}$ is the exciton's effective mass related to the masses of the valence band hole and electron from upper/lower conduction subbands, ϵ is the dielectric constant of the surrounding hBN material, and m_0 stands for the electron mass. The δ parameter is found to be equal to about -0.09 for both bright and dark series, in good agreement with the previously reported value for bright series (-0.008 (9)). The use of this formula to fit the energies obtained from the experiment allowed us to extract the important energies in that system with error values lower

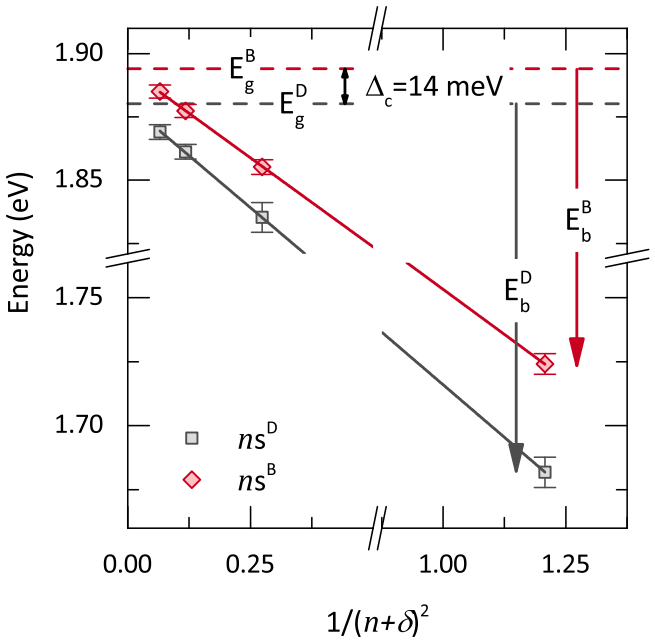

Figure 4.6: The transition energies of the bright (red, ns^B) and dark (grey, ns^D) exciton s-series as a function of $1/(n+\delta)^2$ with $\delta = -0.09$. The error bars correspond to the line widths of the related emission lines. The solid red and grey lines represent best fits to the data with the formula described in the text. The dashed red and grey lines show the band gaps for dark (E_g^D=1.880 eV) and bright (E_g^B=1.894 eV) excitons, while the red and grey arrows mark the binding energies of bright (E_b^B=170 meV) and dark (E_b^D=198 meV) excitons, respectively. The black arrow indicates the conduction band splitting (Δ_{CB}=14 meV).

than 1 meV. The extracted band gaps for dark and bright states are $E_g^D = 1.880$ eV and $E_g^B = 1.894$ eV. Most crucially, from these two values, one can also obtain the amplitude of spin-orbit splitting of the conduction band in this material: $\Delta_{CB} = 14$ meV. Surprisingly, this value is twice lower than the theoretical predictions from the modelling of electronic bands of TMDs MLs (52, 58, 168). It should be noted, however, that these calculations were performed for MLs in a vacuum, and it is not clear what the result on the Δ_{CB} would have the band renormalisation effects.

The binding energies of ground states of bright and dark excitons are two other parameters extracted from the fitting: $E_b^B = 170$ meV and $E_b^D = 198$ meV. Now, following the Eq.(4.2) and Fig. 4.6, the energy ratio between these energies is: $\rho_{DB} = E_b^D/E_b^B = 1.16$. As previously noted, the difference between these two values is expected

to be defined by the differences in electrons' masses and exchange interactions in these two excitonic complexes. Now using the calculated masses of a valence hole ($m_h = 0.36$) and electrons in two conduction subbands ($m_e^D = 0.40$ and $m_e^B = 0.29$), one can find the ratio of effective exciton masses of $\mu^D/\mu^B = 1.18$, which is very close to the experimentally derived ratio of the binding energies. This suggests that the effect of the exchange interactions can be negligibly small. This claim, however, has to be taken with caution as the calculated masses are not necessarily precise enough. Nonetheless, this finding could raise a question about the importance of the exchange term on the energies of bright and dark exciton series in TMD monolayers.

4.4 Conclusions

In this chapter, it was shown for the first time that magnetic brightening could be used to probe the excited states of dark excitons in TMD MLs. Quadratic increase of the relative intensity of dark states to bright states confirmed the observation of the former. The comparison of the energy ladders of bright and dark exciton Rydberg series allowed to obtain the long-sought and highly important for the interpretation of experimental results parameter in hBN encapsulated WSe_2 ML - the amplitude of the spin-orbit splitting of the conduction band. Its value of 14 meV, significantly lower than commonly assumed, shows that the theoretical modelling of the electronic bands might need some revision. The binding energies of two exciton species with a comparison with calculated masses of electrons in two conduction band subbands suggest that the impact of the exchange interactions on the energies of these two excitonic complexes could be negligible.

5

Highly anisotropic excitons in bulk ReS_2

5.1 Introduction

The transition metal dichalcogenides based on rhenium, such as rhenium disulfide and rhenium diselenide, are also semiconductors, but with some stark differences when compared to the S-TMDs of group VI that were discussed in previous chapters. These differences originate mainly from the different number of valence electrons (two in the case of rhenium, six for molybdenum and tungsten), what affects the ways of bond creation in the crystal and hence the crystal structure. Although rhenium based S-TMDs also crystallize in layered form, with a single layer of transition metal atoms sandwiched between two layers of chalcogen atoms, the character of a single layer is significantly different(25). Whereas the MoS_2 and alike crystallize mainly in $2H$ and $3R$ phases with hexagonal in-plane symmetry, strong interactions between transition metal atoms in rhenium based S-TMDs lead to the $1T'$ phase, with the chains of the Re_4 clusters producing Jahn-Teller distortion that breaks hexagonal in-plane symmetry(86, 87, 88). This results in structural anisotropy of the ReS_2 and $ReSe_2$ that in turn manifests itself in robust optical anisotropy, with the optical response highly sensitive to the linear polarization of the interacting light (112, 169, 170).

While the substantial experimental and theoretical efforts provided a fair understanding of the basic electronic and optical properties of group VI S-TMDs, there are still many controversies regarding the group VII (rhenium-based) counterparts. One of

the examples of such disagreements regards the character of the band structure. While the most of the experimental studies point towards the indirect bandgap of the bulk and thin layers of ReS_2 and $ReSe_2$ (89, 90, 91, 92, 93, 94, 95), some other results suggest direct bandgap (98, 99). Similarly, theoretical calculations are not conclusive on this issue (96, 97). This is in stark contrast to the case of group VI S-TMDs for which it is largely agreed that bandgap is indirect for bulk materials and undergoes a transition to direct in the monolayer limit (30, 47, 48, 49, 50).

Another parameter differentiating Re-dichalcogenides from Mo- and W-based ones seems to be the strength of interlayer coupling, although not without further disputes. In all TMDs, layers are rather weakly coupled, only by the Van der Waals forces significantly weaker intralayer interactions between atoms. Nonetheless, this interlayer coupling can still have an impact on the electronic properties of the system, and in the case of the group VI S-TMDs, this coupling is responsible for the transition from indirect to direct bandgap (48, 49). In group VII, S-TMDs coupling seems to be much weaker (97, 101, 102, 103, 104, 105), hence the electronic and optical properties should be determined predominantly by the intra-layer coupling parameters even in the limit of bulk crystals. However, this is still disputed, as some works point towards the small but still relevant interlayer coupling (98, 171, 172). Nonetheless, while the intralayer coupling of group VI S-TMDs leads to the drastic increase of the PL yield when a material is thinned down to the monolayer limit (30, 47), the opposite was observed in the case of ReS_2, where the strongest PL signal is observed for bulk material (24). Hence, the advantage of working with bulk or multilayer structures combined with the strong in-plane anisotropy makes Re-based dichalcogenides promising for applications in polarization-sensitive devices (173, 174, 175, 176).

Strong Coulomb interactions lead to the dominance of the exciton effects in optical response in both group VI (177, 178, 179) and group VII (24, 89, 90, 105, 113, 172, 180) S-TMDs. However, the excitons in those groups differ significantly, as the symmetries of these structures are contrasting. Hexagonal symmetry of Mo- and W-based S-TMDs implies their uniaxial character and leads to the coupling of excitons mostly with circularly polarized photons. Recent theoretical and experimental studies have allowed an almost complete understanding of the fine structure of neutral excitons in group VI S-TMDs (66, 67, 81, 118, 134, 136, 181) and also indirect/intervalley excitons and their phonon replicas as well as more complicated excitonic complexes such as trions and

biexcitons (162, 163, 164, 165, 166, 167, 182). A similar understanding is lacking in the case of rhenium-based materials. The optical response of these structures is known to be governed mainly by two distinct excitonic resonances, split in energy and linearly polarized along different in-plane directions (24, 89, 90, 100, 113, 114, 172, 180). It is still ambiguous, however, what is the origin of these two excitons and their polarization properties. Few contradictory scenarios have been proposed so far. First involves the exchange interaction mediated splitting of excitons(105), the second assign the excitons to transitions at two different Z and K1 points of the Brillouin zone (114) and the third sees the involvement of different atomic orbitals (113).

In this chapter, focused on bulk ReS_2, the properties of excitonic resonances are probed by the magnetophotoluminescence experiments, with a magnetic field applied in Faraday and Voigt geometries, with few different orientations of a magnetic field with respect to the crystallographic orientation of the samples. This work focuses on the Rydberg series of excitons, with the ground and excited states. Two series of "dark" excitons are observed for the first time, in complement to commonly observed two other series of "bright" excitons (24, 113). It is also shown that all four observed excitonic series can be well explained with a theoretical model describing the energy diagrams of the direct-gap excitons associated with a single point of the Brillouin zone, split by the strong exchange interaction.

5.2 Experimental results

5.2.1 Excitonic resonances in PL of bulk ReS_2

The unpolarized low-temperature ($T = 4.2$ K) photoluminescence (PL) response of the bulk ReS_2 is shown in the Fig. 5.1. Several emission lines can be distinguished, here denoted as: $1s^{\alpha}$, $1s^{\beta}$, "?", $2s^{\alpha/\beta}$, $3s^{\alpha/\beta}$, $4s^{\alpha/\beta}$ and E_g. It was already reported in previous works on this material that the $1s^{\alpha}$ and $1s^{\beta}$ transitions are almost perfectly linearly polarized (24, 89, 90, 113, 172, 180) - when rotating the axis of the linear polarizer placed in the collection beam, one can extinguish either $1s^{\beta}$ or the $1s^{\alpha}$ emission peak. The dependence of the PL intensity on the collected signal polarization, probed at the energies marked on the figure by vertical blue and red lines, are presented on the inset of Fig. 5.1. The intensities of $1s^{\alpha}$ and $1s^{\beta}$ transitions as a function of the linear polarization of the collected signal follow sine-like dependence with the angle between their maxima

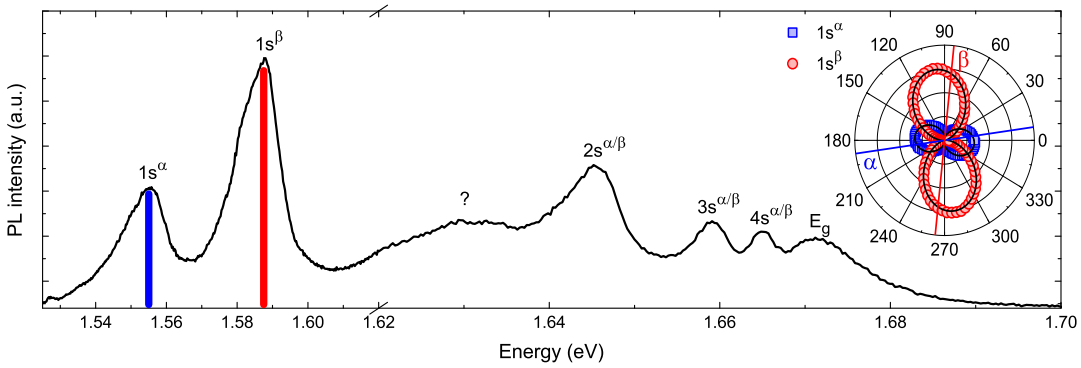

Figure 5.1: Unpolarized low-temperature photoluminescence response of the bulk ReS_2 sample. The energy scale has been stretched in the energy region of the excited transitions for clarity. The inset presents the PL intensities of $1s^{\alpha/\beta}$ transitions as a function of the linear polarization of the signal obtained at the energies marked by the blue and red vertical lines on the main figure, along with the black lines representing fits with a sine function. Blue and red lines on the inset represent the $\alpha-$ and $\beta-$ linear polarization angles for which $1s^{\beta}$ and $1s^{\alpha}$ series are absent form the spectra, respectively.

equal to 75°. Now, by tuning the linear polarization of the collected signal, one can find such angles for which intensities of either $1s^{\beta}$ or $1s^{\alpha}$ transitions have their minima (see blue and red lines on the inset of Fig. 5.1). These two distinct polarization directions are referred to in the text as α- and β-polarizations, respectively.

The α- and β-polarized PL spectra (see Fig. 5.2) reveal that α- and β-polarized spectra are in fact composed of two distinct sets of non-degenerated emission peaks. In line with the previous work on ReS_2 (24), the $1s^{\alpha/\beta}$ resonances are attributed to the ground states excitonic resonances, while the higher energy $2s^{\alpha/\beta}$, $3s^{\alpha/\beta}$ and $4s^{\alpha/\beta}$ resonances are interpreted as the excited excitonic states. This can be proved by the help of the previously invoked, semi-empirical formula describing the excitonic spectrum

Table 5.1: Parameters obtained by fitting Eq(5.1) to the energies of the α- and β-polarized excitonic series, as shown on the inset of the Fig. 5.2.

	E_g (eV)	Ry^* (meV)	γ	E_b (meV)
ns^{α}	1.671	110	-0.03	117
ns^{β}	1.671	123	0.21	84

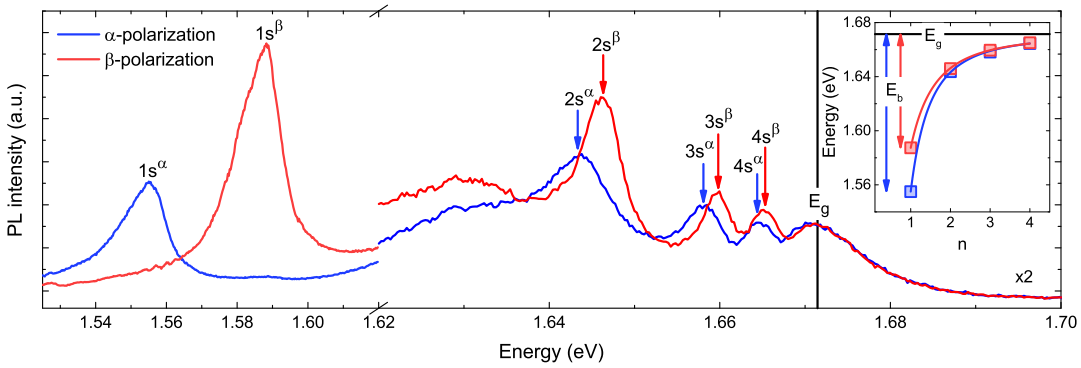

Figure 5.2: α-polarized (blue) and β-polarized (red) low-temperature photoluminescence response of the bulk ReS_2 sample. The energy scale has been stretched in the energy region of the excited transitions, and spectra were multiplied by a factor of 2 for clarity. The inset presents the experimentally obtained transition energies for the ns^{α} and ns^{β} exciton states as a function principal quantum number n. Solid blue and red lines show fits to the data by Eq(5.1). The black vertical and horizontal lines on the main figure and the inset, respectively, highlight the bandgap energy E_g obtained from the fits, while blue and red arrows on the inset represent corresponding binding energies E_b.

(8, 9) and its comparison with the energy diagrams of both ns^{α} and ns^{β}:

$$E_n^{\alpha/\beta} = E_g - \frac{Ry^{*,\alpha/\beta}}{(n+\gamma^{\alpha/\beta})^2}, \tag{5.1}$$

where E_n is the energy of the excitonic state with principal quantum number n, E_g is the bandgap associated with the given Rydberg series, Ry^* is the effective Rydberg constant, and γ is the parameter which accounts for the effective dimensionality of excitonic states (8) and also possible inhomogeneity of dielectric environment(9). This model reproduces the experimental energy diagrams very well with the use of parameters summarized in Table 5.1 as shown in the inset to Fig. 5.2. Moreover, band gap energy obtained from the fit fall into the spectral range of the highest energy emission band observed in both spectra. Hence, this feature could be attributed to the response due to the continuum of single-particle electron-hole excitations, consistent with the characteristic high energy tail. Unfortunately, the emission lines related to the higher excitonic states with $n > 4$ cannot be resolved but are expected to fall within the higher energy tail of the $4s^{\alpha/\beta}$ peaks. This assignment is confirmed by measurements of magnetophotoluminescence in Faraday configuration (which are discussed further in the text), which demonstrate that

$4s^{\alpha/\beta}$ transitions broaden significantly (see Fig. 5.4), as expected for the line composed of higher excited states with varying diamagnetic constants.

5.2.2 Magneto-photoluminescence

In order to get more insight into the nature of the observed two excitonic Rydberg series, the magnetophotoluminescence measurements were performed for both α and β polarization configurations in magnetic fields up to 30 T in various experimental geometries. The measurements performed in Faraday configuration (with the magnetic field applied in the out-of-plane direction of the sample) are expected to lift the spin degeneracy, if there is any, of the observed states by the Zeeman splitting. The measurements in Voigt configurations (magnetic field applied in the in-plane direction of the sample) should lead to the mixing of the excitons with opposite electrons' and holes' spins, possibly leading to the brightening of the dark excitons, as discussed in previous chapters. Moreover, as the ReS_2 has an in-plane anisotropy, the magnetic field interactions could also depend on the angle between the direction of the applied magnetic field and the chosen in-plane crystal axis (here, the b-axis, parallel to the rhenium-chains, will be invoked). Hence, the measurements in Voigt geometry were performed for three different angles. Since there are two non-degenerate bright exciton Rydberg series in ReS_2, one can expect at least two other non-degenerate dark excitons series. Whether the observed bright excitons originate from the same point in the Brillouin zone or two different points will determine the nature of interactions between these states, as magnetic mixing is expected only for the states originating from the same valley.

5.2.2.1 Out-of-plane magnetic field

The magnetophotoluminescence response of ReS_2 measured in α and β polarizations in the Faraday configuration in magnetic fields up to 30 T is shown in the Fig. 5.3(a) and (c), respectively. No Zeeman effect can be observed, suggesting that the observed ns^{α} states are not spin-degenerate. Surprisingly, the blueshift induced by diamagnetic shift is very weak, even for the higher excited states. Moreover, as highlighted in Fig. 5.3(b) and (d), some of the states get significantly broader. This broadening is prominent for the whole α-polarized series and $4s^{\beta}$ state.

For more quantitative analysis the relative broadening $(100\% \cdot [\gamma(B) - \gamma(0)]/\gamma(0))$ of the excited states was calculated and presented in the Fig. 5.4. As can be seen, the

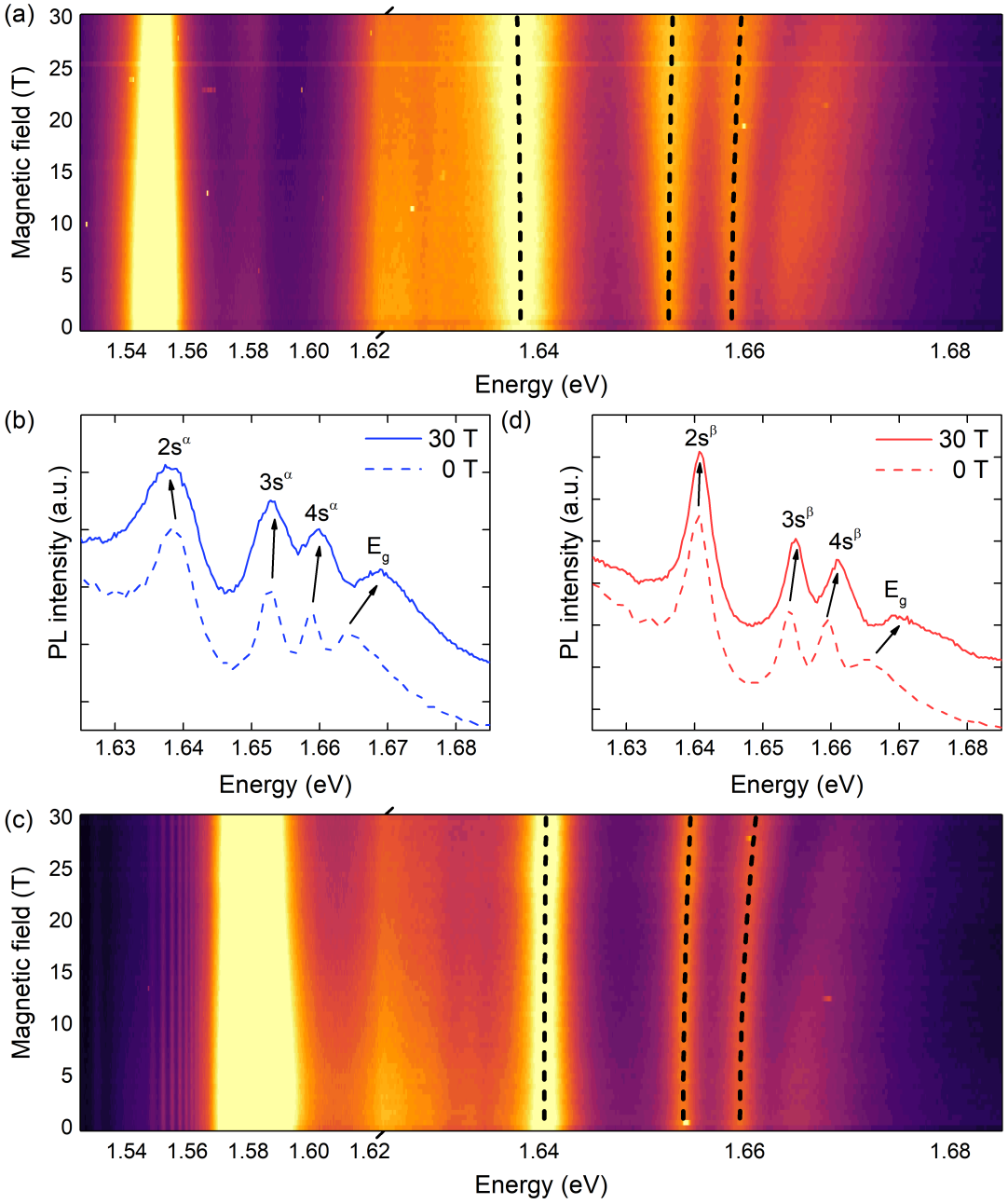

Figure 5.3: False-colour maps of the PL response as a function of magnetic field in the Faraday configuration for (a) α- and (c) β- linear polarizations. The energy scales has been stretched in the energy region of the excited transitions for clarity. The dotted lines represent quadratic fits to transition energies. Comparison of the spectra obtained for (b) α- and (d) β- linear polarizations at $B = 0$ T (dashed lines) and $B = 30$ T (solid lines) in the range of the excited states.

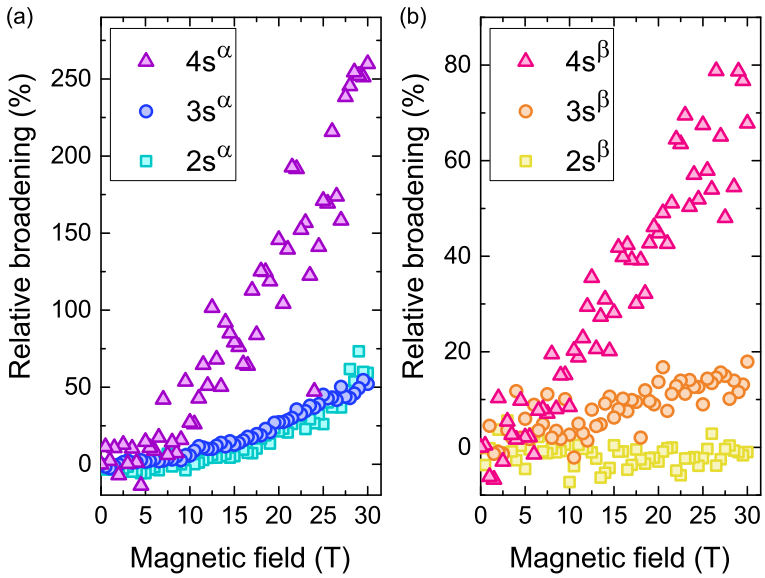

Figure 5.4: Relative broadening of the excited states of (a) ns$^{\alpha}$ and (b) ns$^{\beta}$ excitonic series as a function of magnetic field applied in Faraday configuration.

broadening of the 2s$^{\beta}$ and 3s$^{\beta}$ states is negligible (less than 20%), corresponding states from the other series broaden significantly, by around 50% at $B = 30$ T. The origin of this effect will be discussed further in the text. Broadening of the linewidth of both 4s$^{\alpha/\beta}$ states is clearly greater. This could act as a confirmation that these states are, in fact, superpositions of excited states with $n > 3$ not resolved energetically - while in the magnetic field, these states undergo diamagnetic shifts at different rates, the line becomes broader.

The aforementioned broadening of the emission lines complicates the quantitative analysis of the diamagnetic energy shifts. Nevertheless, the magnitude of the shift can be estimated from the data. Surprisingly, the diamagnetic coefficients σ obtained by fitting dependencies of the energies of the transitions on the magnetic field with the formula: $E(B) = E_0 + \sigma B^2$ (see Fig. 5.3(a) and (c)) are smaller than 2 μeV/T^2, even for the higher excited states. The weak diamagnetic shift can be explained by the additional reduction of the dimensionality of the excitonic states, resulting from the in-plane anisotropy of the carrier's masses (183). Note that 2s$^{\alpha}$ seems to be shifting to lower energies. This could result from a combination of two effects: small (negligible) diamagnetic shift and broadening of the line from the lower energy side.

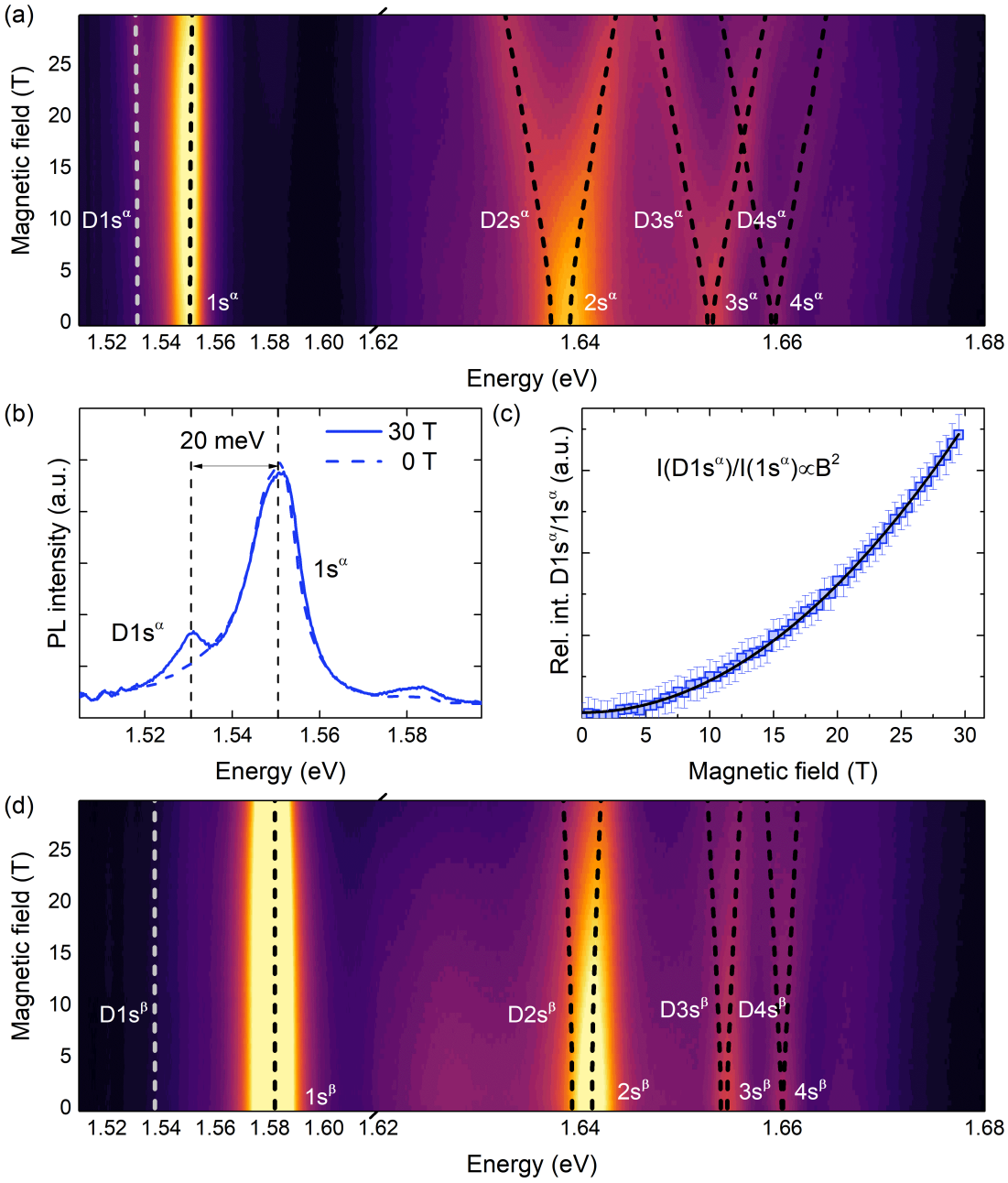

Figure 5.5: False-colour maps of the PL response as a function of magnetic field in the Voigt configuration with $B \parallel b$ for (a) α- and (d) β- linear polarizations. The energy scales on both figures have been stretched in the energy region of the excited transitions. Dashed white and black lines represent transition energies obtained from the theoretical model. (b) Comparison of the spectra obtained for α linear polarization at $B = 0$ T (dashed lines) and $B = 30$ T (solid lines) in the range of the ground state. (c) The relative intensity of the D1s$^{\alpha}$ transition to 1s$^{\alpha}$ (blue squares) as a function of the magnetic field, along with quadratic fit (black line).

5.2.2.2 In-plane magnetic field $B \parallel b$

The results of the magnetophotoluminescence measurements in Voigt configuration with B parallel to the rhenium chains in magnetic fields up to 30 T for α and β configurations of linear polarizations are summarized in Fig. 5.5. There are two main effects that the application of an external magnetic field has on the PL spectra. The first observation is the appearance of the additional resonance in the spectrum in the α polarization, at the energy $\sim$ 20 meV lower than the ns^{α} ground state transition (see Fig. 5.5(b)), possibly due to the magnetic brightening effect. Therefore this resonance is assigned as the dark state $D1s^{\alpha}$. The increase of its intensity relative to $1s^{\alpha}$ state follows quadratic behaviour, as shown in the Fig. 5.5(c), which is a hallmark of the brightening of the dark state in magnetic field (66), confirming the assignment. Nothing similar, however, is observed in the β polarization configuration.

The second effect of the application of the magnetic field is the apparent splitting of all the excited states of the ns^{α} series (see Fig. 5.5(a)). The magnitude of this splitting is roughly the same for all states and can be described by the effective g-factor of $g_{1,\parallel} \sim 6.4$. The excited states of the ns^{β} series are affected by similar splitting, but more than 3 times smaller in magnitude $g_{2,\parallel} \sim 2$ (see Fig. 5.5(d)). Closer inspection, however, shows that this is not, in fact, the splitting of the ns^{α} and s^{β} excited states, but the appearance of the new states in the vicinity of the ones observed at zero fields. Moreover, the interaction between these states leads to energy repelling, much similar to the case of the brightening of dark exciton state in $MoSe_2$ ML, described in Chapter 3.

Hence, both effects can be well explained by the existence of the dark exciton series Dns^{α}. The ground state of that series lies $\sim$ 20 meV below the ns^{α} ground state, while the excited dark states are closer in energy to their bright exciton counterparts. When a magnetic field is applied, dark and bright states are mixed by Zeeman coupling, leading to the brightening of dark states, as demonstrated for the ground dark state $D1s^{\alpha}$. Additionally, when the splitting between bright and dark states is small compared to the energy changes with a magnetic field, as is the case of the excited states, bright and dark states repel each other due to the Zeeman coupling.

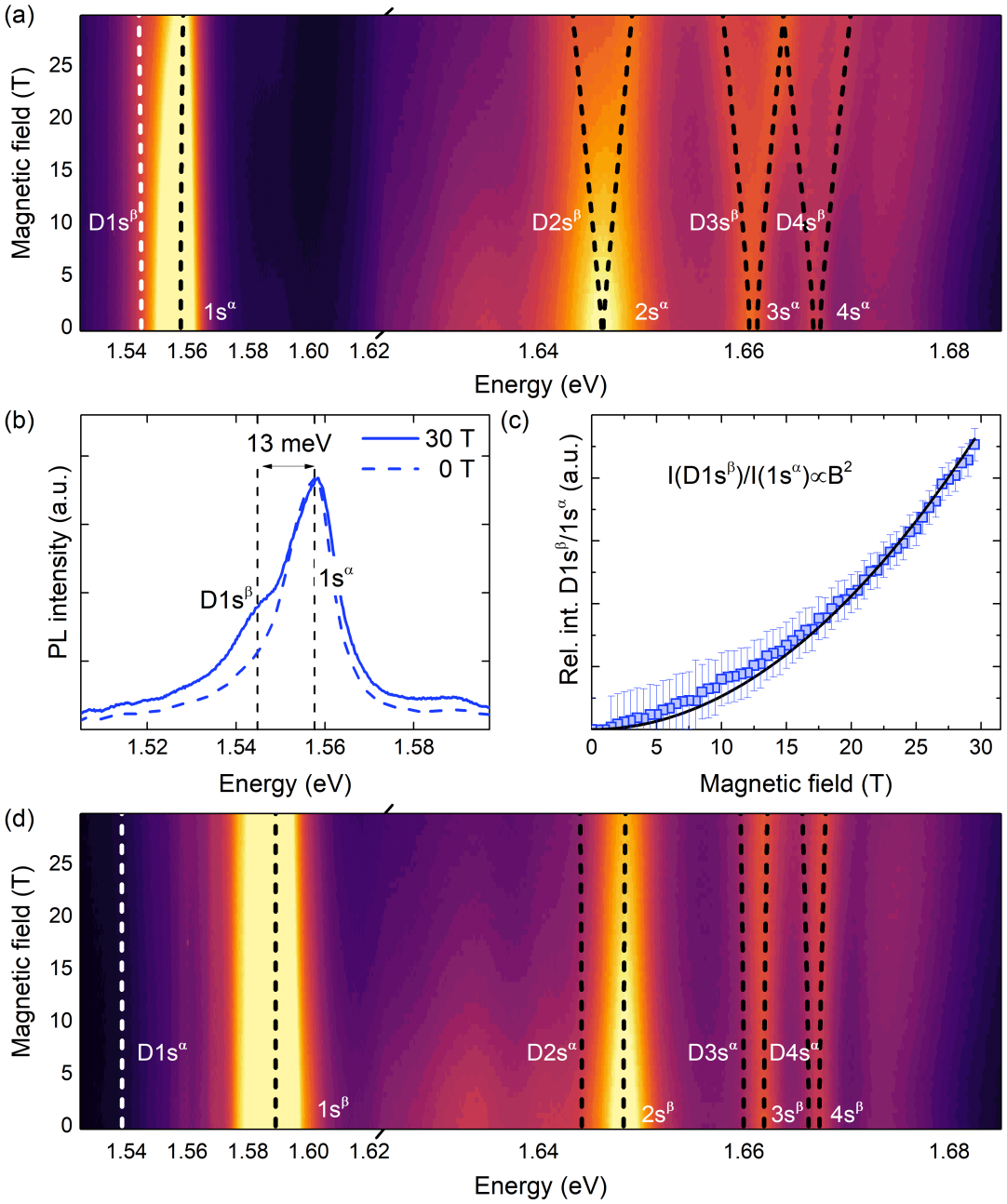

Figure 5.6: False-colour maps of the PL response as a function of magnetic field in the Voigt configuration with $B \perp b$ for (a) α- and (d) β- linear polarizations. The energy scales on both figures have been stretched in the energy region of the excited transitions. Dashed white and black lines represent transition energies obtained from the theoretical model. (b) Comparison of the spectra obtained for α linear polarization at $B = 0$ T (dashed lines) and $B = 30$ T (solid lines) in the range of the ground state. (c) The relative intensity of the D1s$^{\beta}$ transition to 1s$^{\alpha}$ (blue squares) as a function of a magnetic field, along with quadratic fit (black line).

5.2.2.3 In-plane magnetic field $B \perp b$

Qualitatively similar but quantitatively different effects can be observed in the analogous experiments, but with the magnetic field applied perpendicularly to the b-axis, see Fig. 5.6. The first difference is the energy of the brightened ground state (see Fig. 5.6(b)), which is now only about ~ 13 meV lower than that of $1s^{\alpha}$ state. Hence, this has to be a different state than that observed in $B \parallel b$ geometry, and thus this new state is here denoted as $D1s^{\beta}$. One concludes that there are two dark exciton series, which are energetically non-degenerate. As in the previous case, the "brightening" of $D1s^{\beta}$ state nicely follows the quadratic intensity increase in the magnetic field (Fig. 5.6(c)).

The second difference is related to the magnitude of the apparent splitting of the excited states of ns^{α} series - it is notably smaller and corresponds to the effective g-factor of around $g_{1,\perp} \sim 3.6$. No such effect can be noted for the ns^{β} series - there is only a small broadening and blueshift of the lines related to the excited states.

5.2.2.4 In-plane magnetic field $\angle(B, b) \sim 20°$

The measurements performed in $B \parallel b$ and $B \perp b$ Voigt geometries confirmed the presence of two non-degenerate dark exciton series. Moreover, both series interact with the ns^{α} series, which suggest that they have to originate from the same valley in the Brillouin zone. To confirm that, measurements were performed in the additional, intermediate field configuration: $\angle(B, b) \sim 20°$, see Fig. 5.7. Now, the apparent splitting of each excited state of ns^{α} series into three components is observed. Also, the $1s^{\alpha}$ state and the excited states of the ns^{β} series are only blueshifted with the increase of the magnetic field. The energy of the $1s^{\beta}$ resonance does not seem to be affected by the magnetic field. These effects are qualitatively in line with the assumption of the presence of the two non-degenerate dark exciton series, which couple to either ns^{α} and ns^{β} series, depending on the direction of the in-plane field. As measurements in $B \parallel b$ and $B \perp b$ have shown, the coupling of both dark series is stronger with the ns^{α} excitons than with ns^{β} series. This is also reflected in the $\angle(B, b) \sim 20°$ geometry - while both dark series brighten in α polarization, the β polarization shows only the blueshift of the ns^{β} series.

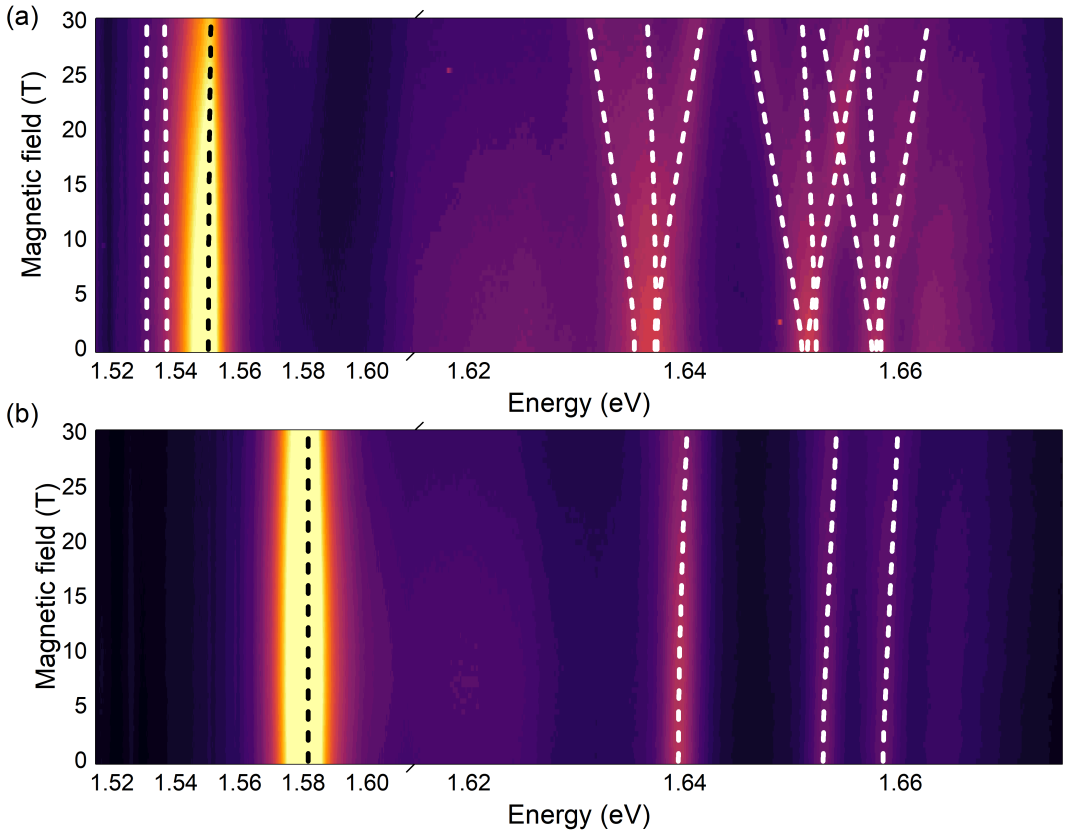

Figure 5.7: False-colour maps of the PL response as a function of magnetic field in the Voigt configuration with $\angle(B, b) \sim 20°$ for (a) α- and (b) β- linear polarizations. The energy scales on both figures has been stretched in the energy region of the excited transitions. Dashed white and black lines represents transition energies obtained from the theoretical model.

5.3 Theoretical modelling

As discussed in the previous section, the effect of the in-plane magnetic field can be qualitatively explained by the presence of two non-degenerate dark exciton series (Dns^{α} and Dns^{β}), in addition to two Rydberg series of bright excitons (ns^{α} and ns^{β}). The results could be summarized in the following way: when a magnetic field is applied along the rhenium chains, the $\mathrm{ns}^{\alpha}(\mathrm{ns}^{\beta})$ states couple via Zeeman terms to $\mathrm{Dns}^{\alpha}(\mathrm{Dns}^{\beta})$ ones, whereas when the magnetic field is applied perpendicularly to the rhenium chains, the $\mathrm{ns}^{\alpha}(\mathrm{ns}^{\beta})$ states hybridize in the same way with $\mathrm{Dns}^{\beta}(\mathrm{Dns}^{\alpha})$ states. This behaviour

in the magnetic field, involving direction-dependent selective coupling of the states, resembles the case of excitonic states in anisotropic quantum dots, where the exchange interaction mixes bright/dark spin states into their linear combinations(12, 128, 184, 185, 186). To provide a quantitative explanation, the model based on the exchange and Zeeman Hamiltonians is introduced in this section. The model parameters are derived from the experimental data and used to calculate the magnetic dependencies of the energies of the observed transitions. Then, the comparison between the results of the modelling and measurements is discussed.

5.3.1 Phenomenological model

The model based on the exchange and Zeeman Hamiltonians, analogous to the ones used in the case of anisotropic quantum dots(12), is used here to describe the observed effects quantitatively. As it will be shown, it can fully explain the results of magnetophotoluminescence experiments performed in Voigt configuration. This is surprising, as the low symmetry of ReS_2 in principle implies more complex form of exchange and Zeeman Hamiltonians than of those describing excitons in anisotropic quantum dots. Further theoretical studies are needed to explain why this model seems to be sufficient.

5.3.1.1 Exchange terms

Bulk crystals of ReS_2 possess only the inversion and time-reversal symmetry. Thus, as states in the Kramers theorem, there is double degeneracy due to the spin of each Bloch band in this material. Two optically allowed transitions can be found between the valence and conduction bands, which conserve total angular momentum, denoted as $|\uparrow\Uparrow\rangle$ and $|\downarrow\Downarrow\rangle$. Here $\{\uparrow,\downarrow\}$ and $\{\Uparrow,\Downarrow\}$ represent the spin states of the conduction band (electrons) and valence band (holes), respectively. These states are related to the bright excitons. The second pair of excitonic states, labelled as $|\uparrow\Downarrow\rangle$ and $|\downarrow\Uparrow\rangle$, is optically inactive and thus related to dark excitons. In principle, the degeneracy of these four excitonic states can be lifted by exchange interaction. Here it is assumed that exchange Hamiltonian, written in the basis $\{|\uparrow\Uparrow\rangle, |\downarrow\Downarrow\rangle, |\uparrow\Downarrow\rangle, |\downarrow\Uparrow\rangle\}$, has the following

matrix representation:

$$\mathcal{H}_{ex} = \frac{1}{2}\begin{pmatrix} +\delta_0 & +\delta_1 & 0 & 0 \\ +\delta_1 & +\delta_0 & 0 & 0 \\ 0 & 0 & -\delta_0 & +\delta_2 \\ 0 & 0 & +\delta_2 & -\delta_0 \end{pmatrix}. \tag{5.2}$$

δ_0, δ_1 and δ_2 are parameters related to the asymmetry and the strength of Coulomb interactions in the system. Bright ($|\uparrow\Uparrow\rangle$ and $|\downarrow\Downarrow\rangle$) and dark ($|\uparrow\Downarrow\rangle$ and $|\downarrow\Uparrow\rangle$) states are split energetically by δ_0. Moreover, the bright states hybridize via δ_1 term, while the dark states hybridize via δ_2. Therefore the eigenstates of the system are described by linear combination of either bright or dark spin states. The excitonic transitions observed in the magnetophotoluminescence experiments can be assigned to the eigenstates of the Eq(5.2) in a way summarized in Table 5.2.

Table 5.2: Exciton eigenvalues, eigenstates and their assignment to transitions in ReS_2 in zero magnetic field.

Energy	Eigenstate	ReS_2 basis
$+\frac{1}{2}\delta_0 + \frac{1}{2}\delta_1$	$\frac{1}{\sqrt{2}}(\lvert\uparrow\Uparrow\rangle + \lvert\downarrow\Downarrow\rangle)$	$\lvert \mathrm{ns}^{\beta}\rangle$
$+\frac{1}{2}\delta_0 - \frac{1}{2}\delta_1$	$\frac{1}{\sqrt{2}}(\lvert\uparrow\Uparrow\rangle - \lvert\downarrow\Downarrow\rangle)$	$\lvert \mathrm{ns}^{\alpha}\rangle$
$-\frac{1}{2}\delta_0 + \frac{1}{2}\delta_2$	$\frac{1}{\sqrt{2}}(\lvert\uparrow\Downarrow\rangle + \lvert\downarrow\Uparrow\rangle)$	$\lvert \mathrm{Dns}^{\beta}\rangle$
$-\frac{1}{2}\delta_0 - \frac{1}{2}\delta_2$	$\frac{1}{\sqrt{2}}(\lvert\uparrow\Downarrow\rangle - \lvert\downarrow\Uparrow\rangle)$	$\lvert \mathrm{Dns}^{\alpha}\rangle$

For the sake of simplicity, this model will be used only for the states with the same principal quantum number n, assuming that the spin states do interact with each other when having different n. This can be justified based on the spatial part of wavefunctions of these states. As all the excitonic states originate from the same two bands, the masses of electrons and holes in those complexes should be the same. Hence, the spacial part of the wavefunctions should not differ for the states with different spin configurations and the same n. The spacial overlap integrals between different spin states should be then equal to 1 for the same n and to 0 when n differs. Therefore, there should be no interaction between states differing by n.

5.3.1.2 Out-of-plane magnetic field

When magnetic field is applied in the out-of-plane direction of the sample and so along excitation and detection axis (Faraday configuration), the Zeeman effect leads to the energy splitting of the excitonic spin states. Hence, the Hamiltonian describing magnetic interactions in the basis invoked before takes the following form:

$$\mathcal{H}^{F}_{zeeman,z} = \frac{\mu_B B_z}{2} \begin{pmatrix} +g_{B,z} & 0 & 0 & 0 \\ 0 & -g_{B,z} & 0 & 0 \\ 0 & 0 & -g_{D,z} & 0 \\ 0 & 0 & 0 & +g_{D,z} \end{pmatrix}. \tag{5.3}$$

In the notation used here the effective out-of-plane g-factor of bright excitons has the following form: $g_{B,z} = g_{e,z} + g_{h,z}$, while the same parameter for dark excitons is: $g_{D,z} = g_{e,z} - g_{h,z}$. $g_{e,z}$ and $g_{h,z}$ are electron's and hole's effective g-factors in the out-of-plane direction. The eigenvalues of the sum of this and exchange Hamiltonians (see Table 5.3) show the following effect: magnetic field applied perpendicularly to the plane of the sample is "unmixing" the spin states into the pairs of bright and dark states, leading again to "clean" spin states in the infinite magnetic field. The higher $\mu_B B_z g_{e,B/D}/\delta_{1/2}$ ratio, the more significant this effect is. However, the Zeeman shift is not linear for the lower field, and its magnitude also depends on this ratio.

Table 5.3: Eigenvalues and eigenstates of the excitonic Hamiltonian in magnetic field in Faraday configuration. $\beta_1 = \mu_B B_z(g_{e,z} + g_{h,z})$, $\beta_2 = \mu_B B_z(g_{e,z} - g_{h,z})$, while N_i are normalization coefficients dependent on the magnetic field.

Energy	Eigenstate
$+\frac{1}{2}\delta_0 + \frac{1}{2}\sqrt{\delta_1^2 + \beta_1^2}$	$N_1[\lvert\uparrow\Uparrow\rangle + \left(\frac{\beta_1}{\delta_1} + \sqrt{1 - \frac{\beta_1^2}{\delta_1^2}}\right)\lvert\downarrow\Downarrow\rangle]$
$+\frac{1}{2}\delta_0 - \frac{1}{2}\sqrt{\delta_1^2 + \beta_1^2}$	$N_2[\lvert\uparrow\Uparrow\rangle + \left(\frac{\beta_1}{\delta_1} - \sqrt{1 - \frac{\beta_1^2}{\delta_1^2}}\right)\lvert\downarrow\Downarrow\rangle]$
$-\frac{1}{2}\delta_0 + \frac{1}{2}\sqrt{\delta_2^2 + \beta_2^2}$	$N_3[\lvert\uparrow\Downarrow\rangle + \left(\frac{\beta_2}{\delta_2} + \sqrt{1 + \frac{\beta_2^2}{\delta_2^2}}\right)\lvert\downarrow\Uparrow\rangle]$
$-\frac{1}{2}\delta_0 - \frac{1}{2}\sqrt{\delta_2^2 + \beta_2^2}$	$N_4[\lvert\uparrow\Downarrow\rangle + \left(\frac{\beta_2}{\delta_2} - \sqrt{1 + \frac{\beta_2^2}{\delta_2^2}}\right)\lvert\downarrow\Uparrow\rangle]$

5.3.1.3 In-plane magnetic field $B \parallel b$

Now let us consider the interaction of the carriers' spins with an in-plane magnetic field (perpendicular to the excitation/detection axis - Voigt configuration). However, as the ReS_2 is an in-plane anisotropic crystal, the angle between the field direction and the chosen in-plane axis (here b-axis defined by rhenium chains) will also have an impact on magnetic interactions. In Hamiltonians, this will be only affecting the phase of the matrix elements. The differing phase will have, however, some crucial implications due to the exchange driven mixing of the spin states, as will be discussed further in the text.

When the in-plane magnetic field parallel to the b-axis is applied, the Hamiltonian of the magnetic interactions of the following form has to be added to Eq(5.2):

$$\mathcal{H}^V_{zeeman,\parallel} = \frac{\mu_B B_\parallel}{2} \begin{pmatrix} 0 & 0 & +g_{h,\parallel} & +g_{e,\parallel} \\ 0 & 0 & +g_{e,\parallel} & +g_{h,\parallel} \\ +g_{h,\parallel} & +g_{e,\parallel} & 0 & 0 \\ +g_{e,\parallel} & +g_{h,\parallel} & 0 & 0 \end{pmatrix}. \tag{5.4}$$

Here, $g_{e,\parallel}$ and $g_{h,\parallel}$ are effective in-plane g-factors in the direction of b-axis of electrons and holes, respectively. The eigenstates of the sum of Eq(5.2) and Eq(5.4) and their energies, along with the corresponding states in ReS_2 basis are presented in Table 5.4. As can be seen, the application of the magnetic field in this configuration leads to the coupling of ns^α state to Dns^α state via $(g_{h,\parallel} - g_{e,\parallel})$, while ns^β state couples to Dns^β state via $(g_{h,\parallel} + g_{e,\parallel})$. The asymmetry of the coupling parameters explains why different magnitudes of the brightening and the splittings are observed in the experiment for α and β polarizations.

5.3.1.4 In-plane magnetic field $B \perp b$

Finally, in the Voigt configuration with the magnetic field applied perpendicularly to the b-axis, the Hamiltonian of the magnetic interactions takes the following form:

$$\mathcal{H}^V_{zeeman,\perp} = i\frac{\mu_B B_\perp}{2} \begin{pmatrix} 0 & 0 & +g_{h,\perp} & -g_{e,\perp} \\ 0 & 0 & +g_{e,\perp} & -g_{h,\perp} \\ -g_{h,\perp} & -g_{e,\perp} & 0 & 0 \\ +g_{e,\perp} & +g_{h,\perp} & 0 & 0 \end{pmatrix}. \tag{5.5}$$

$g_{e,\parallel}$ and $g_{h,\parallel}$ are effective in-plane g-factors of electrons and holes, respectively, in the direction perpendicular to the b-axis. This case differs from the $B \parallel b$ configuration due to different phases of the matrix elements in general Hamiltonian, here leading to

Table 5.4: The eigenvalues and eigenstates in the ReS_2 basis of excitons in magnetic field in Voigt $B \parallel b$ configuration. The mixing α_i and normalization N_i coefficients are complicated functions of the magnetic field.

Energy	Eigenstate in ReS_2 basis
$+\frac{1}{4}[-(\delta_1+\delta_2)+\sqrt{(2\delta_0-\delta_1+\delta_2)^2+4(g_{h,\parallel}-g_{e,\parallel})^2\mu_b^2B^2}]$	$N_1(\lvert \mathrm{ns}^{\alpha}\rangle+\alpha_1\lvert \mathrm{Dns}^{\alpha}\rangle)$
$+\frac{1}{4}[+(\delta_1+\delta_2)+\sqrt{(2\delta_0+\delta_1-\delta_2)^2+4(g_{h,\parallel}+g_{e,\parallel})^2\mu_b^2B^2}]$	$N_2(\lvert \mathrm{ns}^{\beta}\rangle+\alpha_2\lvert \mathrm{Dns}^{\beta}\rangle)$
$-\frac{1}{4}[+(\delta_1+\delta_2)+\sqrt{(2\delta_0-\delta_1+\delta_2)^2+4(g_{h,\parallel}-g_{e,\parallel})^2\mu_b^2B^2}]$	$N_3(\lvert \mathrm{Dns}^{\alpha}\rangle+\alpha_3\lvert \mathrm{ns}^{\alpha}\rangle)$
$-\frac{1}{4}[-(\delta_1+\delta_2)+\sqrt{(2\delta_0+\delta_1-\delta_2)^2+4(g_{h,\parallel}+g_{e,\parallel})^2\mu_b^2B^2}]$	$N_4(\lvert \mathrm{Dns}^{\beta}\rangle+\alpha_4\lvert \mathrm{ns}^{\beta}\rangle)$

different signs. Together with mixing of the spin states via exchange interaction it leads to different coupling rules to those observed in $B \parallel b$. Now the magnetic field mixes ns^{α} state with Dns^{β} state via $(h_{e,\perp}-e_{h,\perp})$ and ns^{β} state with Dns^{α} state via $(g_{h,\perp}+g_{e,\perp})$. The eigenvalues and eigenstates are summarized in the Table 5.5.

5.3.1.5 Consequences of the model

The fine structure of exciton and the impact of the application of external magnetic field in various experimental geometries on the energies of excitonic states as predicted by the presented model are summarized schematically in Fig. 5.8. The exchange Hamiltonian splits all exciton spin states energetically into four non-degenerate linear combinations of bright states (ns^{α} state to $\mathrm{ns}^{\beta)}$) and dark states (Dns^{α} state to $\mathrm{Dns}^{\beta)}$). When the out-of-plane magnetic field is applied (Faraday configuration), it leads to the Zeeman splitting of the exciton spin states ($\{|\uparrow\Uparrow\rangle, |\downarrow\Downarrow\rangle, |\uparrow\Downarrow\rangle, |\downarrow\Uparrow\rangle\}$), leading to their unmixing, with the transition to clean spin states for the infinite magnetic fields. The magnetic field applied in the in-plane direction (Voigt configurations) has a very contrasting impact - it mixes all the exciton spin states. However, if the field is applied along or perpendicularly to the b-axis of the crystal, some symmetry can be still restored. For instance, in the $B \parallel b$ case, although all spin states are being mixed with a magnetic field, in the basis of exchange Hamiltonian, it can be seen as coupling of one of the

Table 5.5: The eigenvalues and eigenstates in the ReS_2 basis of excitons in magnetic field in Voigt $B \perp b$ configuration. The mixing α_i and normalization N_i coefficients are complicated functions of the magnetic field.

Energy	Eigenstate in ReS_2 basis
$+\frac{1}{4}[-(\delta_1-\delta_2)+\sqrt{(2\delta_0-\delta_1-\delta_2)^2+4(g_{h,\perp}-g_{e,\perp})^2\mu_b^2B^2}]$	$M_1(\lvert \mathrm{ns}^{\alpha}\rangle+\beta_1\lvert \mathrm{Dns}^{\beta}\rangle)$
$+\frac{1}{4}[+(\delta_1-\delta_2)+\sqrt{(2\delta_0+\delta_1+\delta_2)^2+4(g_{h,\perp}+g_{e,\perp})^2\mu_b^2B^2}]$	$M_2(\lvert \mathrm{ns}^{\beta}\rangle+\beta_2\lvert \mathrm{Dns}^{\alpha}\rangle)$
$-\frac{1}{4}[-(\delta_1-\delta_2)+\sqrt{(2\delta_0+\delta_1+\delta_2)^2+4(g_{h,\perp}+g_{e,\perp})^2\mu_b^2B^2}]$	$M_3(\lvert \mathrm{Dns}^{\alpha}\rangle+\beta_3\lvert \mathrm{ns}^{\beta}\rangle)$
$-\frac{1}{4}[+(\delta_1-\delta_2)+\sqrt{(2\delta_0-\delta_1-\delta_2)^2+4(g_{h,\perp}-g_{e,\perp})^2\mu_b^2B^2}]$	$M_4(\lvert \mathrm{Dns}^{\beta}\rangle+\beta_4\lvert \mathrm{ns}^{\alpha}\rangle)$

bright linear combinations with one of the dark linear combinations. Hence in the basis invoked in the discussion of experimental results, ns^{α} state couples with Dns^{α}, while ns^{β} state couples with Dns^{β}. On the other hand, in the $B \perp b$ configuration ns^{α} state couples with Dns^{β}, while ns^{β} state couples with Dns^{α}. However, when a magnetic field is applied in any intermediate in-plane direction, all the states are mixed in a complicated manner.

Another interesting result of this model is the magnitude of the magnetic interactions. In an out-of-plane field, the Zeeman splitting of spin states is proportional to the sum of electrons and holes g-factors in the case of bright states and the difference for the dark states. As the electrons and hole g-factors are expected to have opposite signs in the chosen notation, one can expect a more substantial impact on the dark states than on the bright. However, in this configuration, the dark states are not being observed. A similar effect can be observed for the Zeeman coupling in the Voigt configuration. No matter what the direction of the field is, the ns^{α} states couple to dark states via the difference of electrons and holes g-factors, while ns^{β} via their sum, which is consistent with the more prominent effects in α polarization in all geometries of the field.

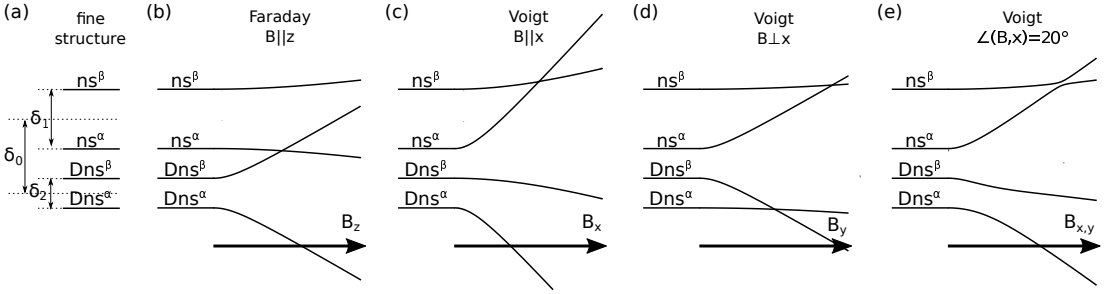

Figure 5.8: Schematic representation of the exciton fine structure at (a) zero magnetic field and in magnetic field B in few geometries: (b) Faraday configuration, (c) Voigt configuration with $B \parallel b$, (d) Voigt configuration with $B \perp b$ and (e) Voigt configuration with $\angle(B, b) \sim 20°$. The black arrows indicate which states are coupled in magnetic field, with the coupling constant indicated, with an exception of last panel, as for this configuration all the states are coupled in a complex way.

5.3.2 Parameters

To compare the experiment with the model in a more strict way, the parameters for the model are needed: g-factors of electrons and holes and exchange splitting constants δ_i. In order to extract these parameters, the magnetic field dependencies of the energies of the bright and dark states were fitted by using the eigenvalues from Tables 5.4 and 5.5. The example of such fitting was presented in Fig. 5.9. This procedure was applied to measurements in the α-polarization in both $B \parallel b$ and $B \perp b$ configurations. A combination of the results from these measurements allowed us to estimate values of the exchange splitting parameters δ_i. However, a similar approach could not be used in the case of the β-polarization measurements due to the weak effect on the magnetic field interactions. It was only roughly estimated that the g-factors are around ~ 3.4 times smaller. Therefore, to estimate the values of $g_{e,\parallel}$, $g_{h,\parallel}$, $g_{e,\perp}$ and $g_{h,\perp}$, it was assumed that $g_{1,\parallel}/g_{2,\parallel} = g_{1,\perp}/g_{2,\perp} = 3.4$. Thanks to these rough estimations, all the necessary parameters were obtained and summarized in Table 5.6.

5.3.3 Comparison with experimental results

The energies of excitonic states obtained from the theoretical modelling in both $B \parallel b$ and $B \perp b$ Voigt configurations are presented in Fig. 5.5(a),(d) and Fig. 5.6(a),(d), respectively. All the effects observed in the experiment are well reproduced: energies of brightened ground states of dark excitons, slight blueshift of the $1s^{\alpha}$ state energy,

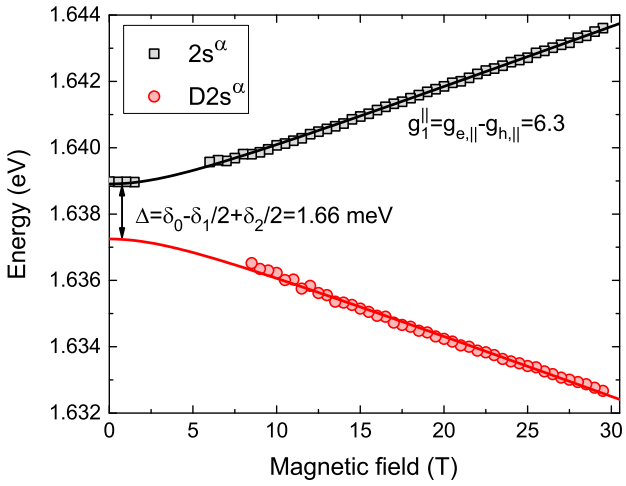

Figure 5.9: Energies of the $2ns^{\alpha}$ and $D2s^{\alpha}$ as a function of the in-plane magnetic field $B \parallel b$ along with the best fit to the corresponding eigenfunctions from the Table 5.4.

apparent splitting of excited states in both configurations and also the difference of the magnitude of that splitting between bright and dark states for ns^{α} and ns^{β} series. Although the model predicts coupling between ns^{β} and Dns^{α}, one cannot observe dark states in the experiment. This can be explained by the low coupling constant between these states (as the model predicts) and the highest energy difference of all possible pairs from the four exciton series. Similarly, the explanation for the lack of the brightening of the ground states of dark excitons in the β-polarization is straightforward: there is a relatively large energy difference between $1s^{\beta}$ and Dns^{α}/Dns^{β} states (as compared with the $1s^{\alpha}$. Overall, the proposed model fits well with the experimental data presented in Fig. 5.5 and Fig. 5.6, which cannot come as a surprise since these datasets were used to obtain the parameters.

A more robust test for the model comes from comparing the measurements in the intermediate $\angle(B,b) \sim 20^{\circ}$ Voigt geometry, which was not used to estimate the parameters. As can be seen in Fig. 5.7., there is a fair agreement between the energies obtained from the model and the experimental dependencies. The apparent splitting of the excited ns^{α} states into three separate components can be explained by the interaction with both dark series and the brightening of those states followed by the energy repelling due to the mixed character of the new states. On the other hand, in both theory and experiment, the $1s^{\alpha}$ state and the excited states of the ns^{β} series are only

Table 5.6: Values of the parameters estimated from the experiment and used for the the calculations.

n	δ_0 (meV)	δ_1 (meV)	δ_2 (meV)	$g_{h,\parallel}$	$g_{e,\parallel}$	$g_{h,\perp}$	$g_{e,\perp}$
1	31.80	31.25	6.37	2.8	-1.6	2.4	-1.3
2	1.94	2.16	2.09	4.0	-2.2	2.2	-1.2
3	0.60	1.45	1.32	4.1	-2.2	2.2	-1.2
4	0.31	0.61	0.86	3.9	-2.1	1.9	-1.0

blue-shifted with the magnetic field. Moreover, the energy of the $1s^{\beta}$ resonance does not change with a magnetic field. Nonetheless, it should be noted that the model predicts weak anticrossing between ns^{β} series and blue-shifted dark states. However, the magnitude of these anticrossings is almost an order of magnitude smaller than the linewidths of observed transitions. Thus, such an effect could not be observed and was omitted in theoretical results to clarify data presentation.

The analogy between the model and the experimental results in the case of the Faraday geometry is less straightforward. As previously pointed out, for this experimental geometry the theory predicts the magnetic field induced unmixing of the observed linear combinations into clean spin states. One could also expect that this would lead to the change of the linear polarisation of linear combinations of bright states into circular/elliptical ones for the spin states. The magnitude of this effect should be defined by the $\mu_B B_z g_{e,B}/\delta_1$ ratio. No such effect can be observed on the ground states. However, this is understandable, as the zero-field splitting of ground states is relatively high, much higher than any energy shift induced by a magnetic field. A similar effect should be observed in the case of the excited states, as they are close in energy in both polarisations. To estimate what magnitude of this effect model predicts, one can analyse energy shifts of excited states in a magnetic field. The model used here does not take into account the diamagnetic shift, but in the first approximation, it can be assumed that this shift is the same for ns^{α} and ns^{β} states with the same principal quantum number n. Then

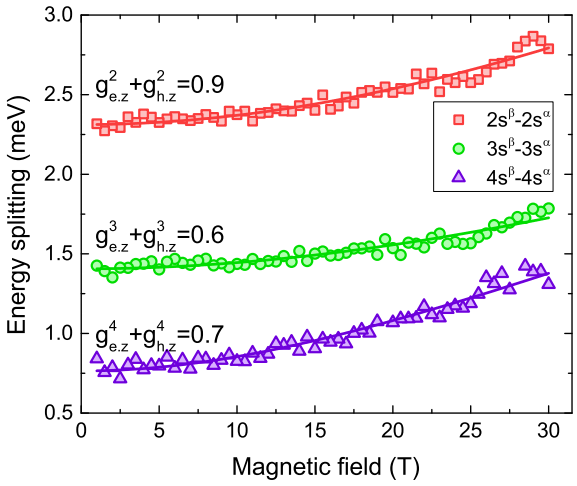

Figure 5.10: The energy splitting of the excited states of the ns^{β} and ns^{α} exciton series along with the lines resulting from the fitting with Eq(5.6).

their energy difference (see Table 5.3) should be:

$$ns^{\beta} - ns^{\alpha} = \sqrt{(\delta_1^{(n)})^2 + [\mu_B B_z (g_{e,z}^{(n)} + g_{h,z}^{(n)})]^2}. \tag{5.6}$$

Fig. 5.10 presents these differences along with the best fits with Eq(5.6) and obtained g-factors. From these g-factors, the value of the ratio $\mu_B B_z g_{e,B}/\delta_1$ can be estimated to be around ~ 0.68, ~ 0.68 and ~ 1.50, for the states with $n = 2, 3, 4$, respectively. According to the model, this should lead to the change of the percentage of the ratio of squares of amplitudes in the $(|\uparrow\Uparrow\rangle + |\downarrow\Downarrow\rangle)$ superposition from 50 : 50 to 22 : 78, 21 : 79 and 8 : 92, respectively. Hence, for states with $n = 4$ that should lead to the almost complete change from linearly polarized to circularly/elliptically polarized emission. This would mean, that both energy and linewidth in the both polarization of lines denoted as $4s^{\alpha}$ and $4s^{\beta}$ (as they are still probed in α and β polatizations) should be the same. This is not in line with the observed PL spectra (see Fig. 5.3(b) and (d)). Therefore the broadening of the excited states observed in Faraday geometry cannot be simply explained by the unmixing of the $|\uparrow\Uparrow\rangle$ and $|\downarrow\Downarrow\rangle$ states or, in other basis, mixing of the $|\,ns^{\alpha}\rangle$ and $|\,ns^{\beta}\rangle$ states.

Moreover, it is clear that the broadening of the $2s^{\alpha}$ state happens on the lower energy side ($2s^{\beta}$ has higher energy, see Fig. 5.3(c) and (f)). A very similar broadening can be observed in the Voigt configuration $B \parallel b$ in the lower fields, when $D2s^{\alpha}$ starts to

appear, but the energy repelling is not yet prominent. One could then argue that there is still some non-negligible component of Voigt-like interactions even when a magnetic field is applied in the out-of-plane direction. If that were the case, also the fact that broadening presented in the Fig. 5.4 is more prominent for the ns^{α} series would be explained (compare with Fig. 5.5(e)). The presence of the Voigt-like interactions when the magnetic field is applied perpendicularly to the plane of the sample could happen in the case of the complex g-factor tensor than assumed in the simple model presented here, possibly due to reduced symmetry of ReS_2.

5.4 Discussion

The afore-described results of the magnetophotoluminescence measurements performed in the Voigt configurations provide indisputable proof of the presence of two non-degenerate dark excitonic Rydberg series in ReS_2. The in-plane field provides a way to brighten those states and observe them in the PL response. The states' selective (dependent on the field direction) coupling resembles the behaviour observed in anisotropic quantum dots of III-V compounds. This similarity is not wholly unexpected - while in the case of dots, it is the anisotropy of the shape that leads to exchange splitting, here the anisotropy of the crystal structure itself enables this effect. The layered character of ReS_2 and the formation of the rhenium chains leads to strong confinement of the carriers and reduction of the dimensionality of the carriers (as also indicated by the extremely low diamagnetic shifts). Since both valence and conduction bands are only spin-degenerated (97), excitons of 4 different spin configurations can be formed at a given point in the Brillouin zone. The exchange interactions resulting from the anisotropy of the structure fully lift their degeneracy, with the new eigenstates being two linear combinations of bright and two of dark states.

Such interpretation is in stark contrast to the recently proposed idea, according to which two linearly polarised excitons originate from two distinct valleys: Z and K1, with both series accompanied by the dark counterparts (114). Although it also leads to the presence of four states, two bright and two dark, it is not compatible with the experimental results presented here. It is shown that the in-plane field can lead to the coupling of ns^{α} and ns^{β} with either of the dark states Dns^{α} and Dns^{β}. If those originated from two different valleys, it would not be possible, as the magnetic field affects

only the spin components of wavefunctions. Therefore the magnetophotoluminescence experiments performed in Voigt geometry confirm that these four excitonic states have to originate from the same valley.

The application of the phenomenological model (based on one describing excitons in anisotropic medium) to the case of bulk rhenium disulfide provides an explanation for most of the experimental results observed in the Voigt geometry. Nonetheless, further theoretical studies are needed to provide a solid explanation of the observed polarisation rules that govern the optical transitions and the behaviour observed in the Faraday geometry.

5.5 Conclusions

Several emission lines that can be distinguished in the low-temperature, zero magnetic field photoluminescence spectrum of the bulk rhenium disulfide are identified here as two bright Rydberg series, split by the exchange interactions resulting from the low symmetry of the crystal. The magnetophotoluminescence measurements performed in Voigt geometry reveal the presence of two additional, non-degenerate dark Rydberg series. All four series hybridise in the magnetic field due to Zeeman coupling in a complex way, dependent on the in-plane direction of the applied field. Those phenomena can be well explained by using the simple, phenomenological model that considers both exchange interactions of spin states and Zeeman Hamiltonians describing interactions of carriers spins with a magnetic field. These findings confirm that all four excitonic Rydberg series originate from the same point in the Brillouin zone. However, the results obtained in the Faraday configuration are not that straightforward and, along with the polarisation rules that govern these transitions, need more theoretical work to be fully understood.

6

Singlet and triplet negatively charged excitons - the case of WS_2

6.1 Introduction

The charged excitons (or trions) are three-particle excitonic complexes consisting of the electron-hole pair and an additional carrier - either an electron or a hole. Trions are being formed in low dimensional semiconductor structures, such as quantum wells (QW)(16, 187, 188) or quantum dots (QD)(189, 190, 191) of III-V or II-VI compounds, with an excess electron or hole density. Such excess carrier density is usually obtained by the modulation doping of the sample(16). It can also be achieved by optical excitation of intrinsic samples in which electrons can tunnel to quantum well from another, narrower QW more effectively than holes(192). Another, more straightforward method for achieving excess carrier density is using quantum well with one thin barrier layer close to the sample's surface, where photo-excited electrons in QW can tunnel to the surface states, leading to the excess density of holes(193).

Recently, the trion complexes were observed also in monolayers of semiconducting transition metal dichalcogenides of group VI such as MoS_2(68), $MoSe_2$(69), WS_2(145), WSe_2(122) and $MoTe_2$(194), even at room temperature(195). This is possible due to exceptionally large exciton binding energies up to 0.5 eV in these materials(59, 196, 197), leading also to the high trion binding energies of 30-40 meV(198). Such monolayers are usually obtained by the mechanical exfoliation of the bulk material(29, 30). The most common technique to used to grow high-quality bulk crystals of the S-TMDs is

chemical vapour transport (CVT)(199, 200). The material grown by this method is usually unintentionally doped, with the doping sign dependent on the transport agent used(199). However, in the case of the monolayers, the charge transfer between the thin film and the substrate is also crucial in determining doping sign and excess carrier concentration(201, 202). Usually, negative unintentional doping is reported for MLs exfoliated on the SiO_2 or Si substrates, and also for MLs encapsulated in hBN(60, 70, 145, 203, 204, 205, 206, 207, 208). The excess electron density leads to the formation of the negatively charged excitons.

One of the main features that distinguishes the MLs of S-TMDs from nanostructures of III-V and II-VI compounds is the peculiar band structure around the K^+ and K^- points of the Brillouin zone, where the direct bandgap is located. Moreover, in the S-TMDs monolayers both conduction and valence bands are split by spin-orbit interaction(52, 55). Consequently, two conduction band subbands and one valence subband at two K^+ and K^- valleys are relevant for the near bandedge optical transitions, while in III-V and II-VI compounds only one conduction and one valence band at single Γ point can be considered. The four electron states involved in optical transitions lead to the possibility of the formation of three doubly-degenerate types of optically active and negatively charged trions, as presented for the case of darkish material in Fig. 6.1, in contrast to only two trions observed in nanostructures of III-V and II-VI compounds(209).

In the "darkish" TMD monolayers, the optically active electron-hole pair consists of an electron from the upper conduction band and a hole from the top valence band, both located in the same valley. Whether the e-h pair resides at K^+ or K^- valley determines the helicity of light (σ^+ and σ^-, respectively) to which the e-h excitation does couple. The trion's additional electron can be located in the lower conduction band in the same valley (first intravalley singlet trion T_S, Fig. 6.1(a)), in the lower conduction band in the opposite valley (triplet trion T_T, Fig. 6.1(b)) or in the upper conduction band in the opposite valley (second intervalley singlet trion T_{S^*}, Fig. 6.1(c)). However, the formation of the T_{S^*} requires high free electron concentrations, what makes its description more complex, beyond a simple image of a three particle state. Hence its observation is difficult, and in non-gated structures usually, only T_S and T_T states are being observed. Other kinds of trions can also be formed in these materials, although they are optically inactive, forbidden by the spin or momentum conservation rules.

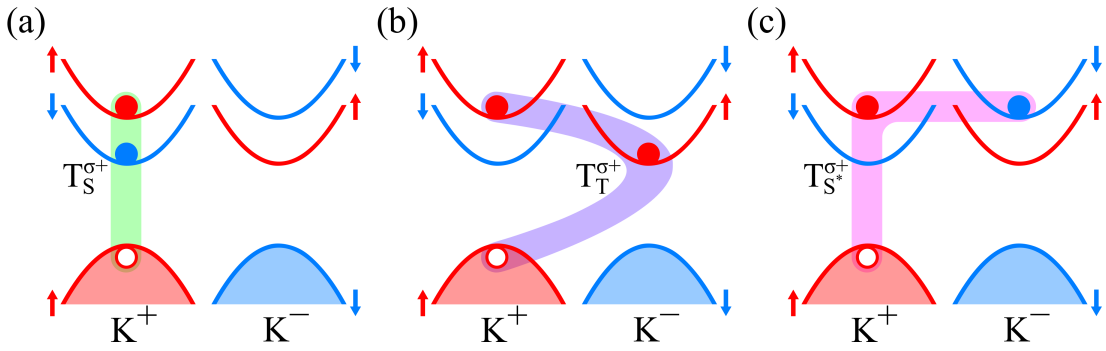

Figure 6.1: Schematic illustration of the σ^+-polarised trion complexes formed in S-TMDs, representative for a darkish material. (a) first intravalley singlet trion state $T_S^{\sigma+}$, (b) triplet trion state $T_T^{\sigma+}$ and (c) second intervalley singlet trion state $T_{S^*}^{\sigma+}$. The red (blue) curves indicate the spin-up (spin-down) subbands. The electrons (holes) in the conduction (valence) band are represented by closed (open) circles. The σ^--polarised counterparts of trion complexes can be obtained by exchange of all the carriers between K^+ and K^- valleys. The trion complexes of the bright materials can be obtained by the exchange of the conduction band subbands in K^+ and K^- valleys.

Optically active excitons in "bright" materials consist of an electron in the lower conduction band and a hole in the top valence band, both in the same valley. The additional electron can be located in the lower conduction band in the opposite valley (first intervalley singlet trion T_S), in the upper conduction band in the opposite valley (triplet trion T_T) or in the upper conduction band in the same valley (second intravalley singlet trion T_{S^*}). This time in the low density of free electrons regime, only T_S complex can be observed.

In MoS_2 monolayers, as the spin-orbit splitting of the conduction band is small(52, 57, 117), the Coulomb (including exchange) interaction have a significant impact on the band order, and thus the trion fine structure cannot be reliably presented in the single-particle picture. The presence of the hole in one of the valleys inverts the energy ordering of the conduction band subbands in the same valley, leading to the possibility of the observation of both intervalley and intravalley singlet trions in low electron density regime(140, 210).

As shown schematically in Fig 3.1, the external out-of-plane magnetic field changes the energy of the band states at K^+/K^- points of the BZ, lifting their degeneracy. Different energies of the lower conduction band subbands lead to the free carrier density imbalance in two valleys (valley polarisation), which in turn affects the formation

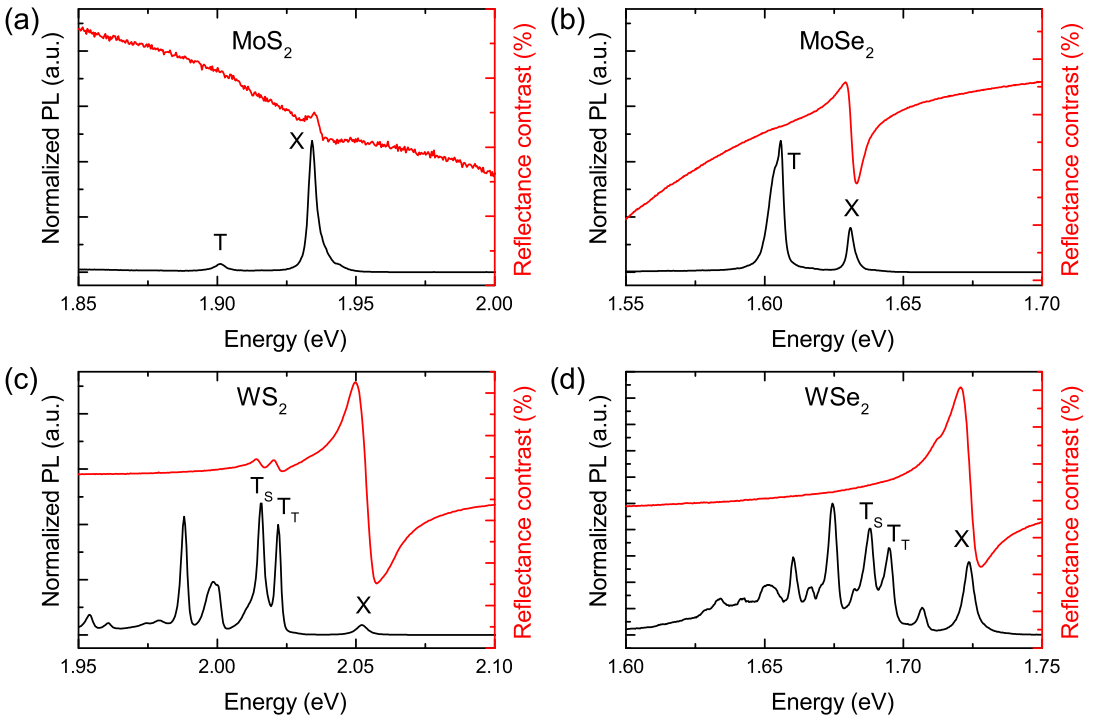

Figure 6.2: Comparison of photoluminescence (black lines) and reflectance contrast (red lines) signals of typical structures of hBN encapsulated (a) MoS_2, (b) $MoSe_2$, (c) WS_2 and (d) WSe_2 monolayers in the energy region of the band-edge optical excitations.

probability of various types of σ^+- and σ^--polarised trions. For example, in a darkish monolayer, the increase of free electrons at K^+ point (at the cost of decrease of the concentration at K^- point) would result in favouring the formation of σ^+-polarised intravalley singlet trions over their σ^- counterparts and also σ^--polarised triplet trions over their σ^+ counterparts. Such valley polarisation of the free electrons and the possibility to probe it via trions' formation could be useful for the emerging field of valleytronics(211).

In order to study the effects of the magnetic field on optical resonances related to trions in TMDs monolayers, the best material candidate was identified first. The comparison of the PL and RC signals of typical structures consisting of TMDs monolayers encapsulated in hBN is presented in Fig 6.2. As can be seen, in the MoS_2 and $MoSe_2$ monolayers, only two resonances can be observed in the energy region of ground optical transitions: those resonances are related to the ground state of bright exciton X and one trion T. However, in the case of the samples available, only the X resonance was

observed in the RC spectra, limiting the experimental possibilities for magneto-optical studies of trions. In the photoluminescence signal of hBN encapsulated WS_2 and WSe_2 monolayers, there are several emission lines - ground state of bright exciton X, singlet T_S and triplet T_T trions and other excitonic complexes such as biexcitons, charged biexcitons, momentum- and spin-forbidden dark excitons. Such states were studied recently in many details in both WSe_2 (162, 163, 164, 212) and WS_2 monolayers (134, 182). In this chapter, however, the focus is on the singlet and triplet trions. Such resonances are nicely spectrally resolved in the PL of both WS_2 and WSe_2, but easily observable in the RC spectrum only in the case of WS_2. To take advantage of both techniques for the magneto-optical studies of trions, the encapsulated WS_2 monolayer was chosen for this project, and the rest of the chapter will concern only this structure.

6.2 Experimental results

This section presents the experimental results on the singlet and triplet trions' behaviour in the out-of-plane magnetic field. First, the zero-magnetic field reflectance contrast and photoluminescence spectra are shown, and energies, intensities and shapes of the resonances are discussed. Then the results of magneto-optics are described - first probed by RC and then by PL.

6.2.1 Trion resonances in tungsten disulfide monolayer

The low-temperature ($T = 4.2\,\mathrm{K}$) reflectance contrast and photoluminescence response of the WS_2 monolayer encapsulated in hBN flakes are presented in the energy range of exciton and trion complexes in Fig. 6.3. The RC spectrum consists of three distinct resonances indicated as X_A, T_T, and T_S. The same transitions can also be distinguished in the emission spectrum. The X_A feature is assigned to the ground state of the neutral A-exciton formed in the vicinity of the bandgap, in agreement with previous studies of WS_2 monolayers(9, 59, 70, 147, 207, 213). In line with the previously published observations(83, 207, 208, 214), the T_T and T_S features are identified as the triplet and singlet states of the negatively charged excitons (see Fig. 6.1(a) and (b)), respectively. Note that the PL spectrum also includes several additional lines (not shown here, but visible in the Fig 6.3(c)) apparent on the low energy side of trions emissions, related to the recombination of various excitonic complexes, such as biexcitons, charged

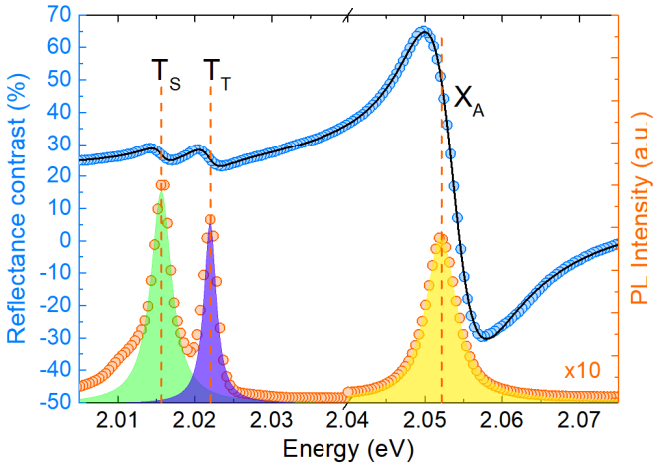

Figure 6.3: Reflectance contrast (blue dots) and photoluminescence (orange dots, E_{exc} = 2.408 eV, P_{exc} = 20 μW) spectra of WS_2 monolayer encapsulated in hBN, measured at T = 4.2 K. The black curve is the result of a fitting of the RC spectrum with three Fano resonances. The green/purple and yellow Lorentzians represent the best fits to spectral lines related to the singlet/triplet trions and neutral exciton, respectively. The PL spectrum in the higher energy region of the X_A peak was multiplied by a factor of 10 for clarity.

biexcitons, momentum- and spin- forbidden dark excitons and trions, and also their phonon replicas (66, 70, 134, 145, 165, 182, 207).

To obtain the energies and relative amplitudes of these resonances from the measurements, the RC spectrum was fitted using three Fano-type functions, while the PL spectrum was fitted using three Lorentzian functions. The energy of X_A transition is of 2.052 eV. The T_T resonances in both experiments are located ~30 meV below the X_A, while the energy difference Δ_{T-S} between T_T and T_S is of ~7 meV. These values agree very well with those reported previously (83, 85, 214, 215, 216).

While there is good agreement between the two types of spectra regarding the energies of the observed features, discrepancies in relative amplitudes of the trions and exciton responses in the RC and the PL spectra underline the fundamental difference of these two optical phenomena. As for the absorption-type measurement, the reflectance contrast probes the product of the density of states and the oscillator strength of a given transition. In the case of the photoluminescence (emission-type) measurements, on the other hand, the intensity also reflects the occupation of the states, and thus it strongly depends on the efficiency of relaxation processes and quasi-thermal distribution of the

carriers. The formation of the neutral exciton is related to the density of excitonic states and its intrinsic oscillator strength, characteristic for a given material(122, 217, 218). An additional free electron is required for the negative trion creation, thus the observation of trion related resonances in the optical response is dependent on the carrier concentration, or, in other words, on the Fermi energy (E_F). E_F can be tuned externally, for instance, in gated structures (165, 207, 213, 219). The unintentional n-type doping, which allows for the creation of trions in the probed hBN/WS_2/hBN structure is commonly reported in this material(70, 145, 207, 208) and therefore the gating is not required. As the amplitude of the trions resonances in the RC signal is small compared to the exciton resonance, the free carrier concentration is expected to be relatively small.

6.2.2 Trion resonances in magnetic field - the RC response

Fig. 6.4(a) presents the magnetic field evolution of the helicity-resolved RC spectra measured in magnetic fields up to 14 T on the studied WS_2 ML in the energy region of the T_T and T_S resonances. Two effects of the applied magnetic fields can be appreciated. First one is the energy splitting of transitions into two circularly polarised components, related to the excitonic Zeeman effect. The second effect is the substantial change of the amplitude of observed resonances. The σ^+-polarised component of T_S feature and σ^--polarised of T_T resonance decrease in intensity with the increase of the magnetic field and completely vanish at 14 T. In contrast, the intesities of i.e. $T_S^{\sigma-}$ and $T_T^{\sigma+}$ increase with the strength of the applied magnetic field.

To analyse the energy and amplitude evolutions of these features, the spectra were fitted with Fano-like functions. The energies and amplitudes extracted from such fitting are presented in Fig. 6.4(b) and (c). Moreover, presented in Fig. 6.4(d) is the degree of circular polarisation defined as $\mathscr{P} = (I_{\sigma^+} - I_{\sigma^-})/(I_{\sigma^+} + I_{\sigma^-}) \times 100\%$, where $I_{\sigma^+}/I_{\sigma^-}$ is the signal intensity detected in the σ^+/σ^- polarisation. The magnetic field dependence of these three properties will be discussed in more detail in Sec. 6.3.

6.2.3 Trion resonances in magnetic field - the PL response

Similar, yet not entirely analogous, the magnetic field dependence of the trion features can be observed in the magnetic field evolution of the PL spectra, as shown in Fig. 6.5(a). As in the RC experiment, the trion features show the Zeeman splitting of circularly polarised components. The evolution of the intensities of the PL resonances, on the

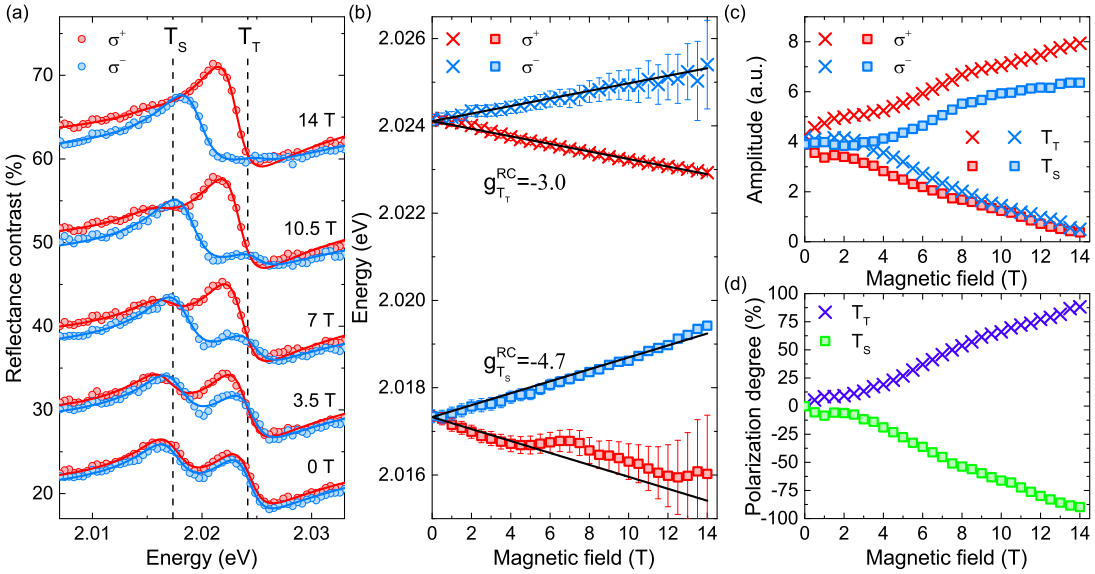

Figure 6.4: (a) Circular-polarisation-resolved low temperature ($T = 4.2$ K) RC spectra of the hBN encapsulated WS_2 monolayer in the energy region of singlet (T_S) and triplet (T_T) trions at selected values of the out-of-plane magnetic fields. The dots denote the measured signals, while the lines represent best fits to the signal. The red (blue) colour corresponds to the σ^+-polarised (σ^--polarised) spectra. The dashed vertical lines indicate the zero-field energy positions of trions. The spectra are vertically shifted for clarity. (b) Transition energies of the T_S and T_T features extracted from the fits to the RC spectra as a function of the magnetic field. The squares (crosses) represent the T_S (T_T) resonances. The solid black curves represent fits according to Eq. 6.1. Magnetic field dependency of (c) the intensities and (d) the polarisation degrees of the T_S and T_T transitions extracted from the fits of the RC spectra.

other hand, is not the same: only the σ^--polarised component of T_S state is strongly enhanced in a magnetic field, while the rest of the features show less prominent change.

Spectra were fitted using Lorentzian functions to extract the change of the energies and amplitudes of the observed PL peaks induced by the out-of-plane magnetic field. It is important to mention that for the detected σ^+-polarised PL, the σ^--polarised signal is also apparent, most probably due to the non-perfect alignment of a circular analyser and the slight leakage of a strong signal of opposite polarisation, which was considered during the data analysis. The results of the fitting i.e. extracted energies and amplitudes and also the degree of circular polarisation, are shown in Fig. 6.4(b), (c) and (d), respectively.

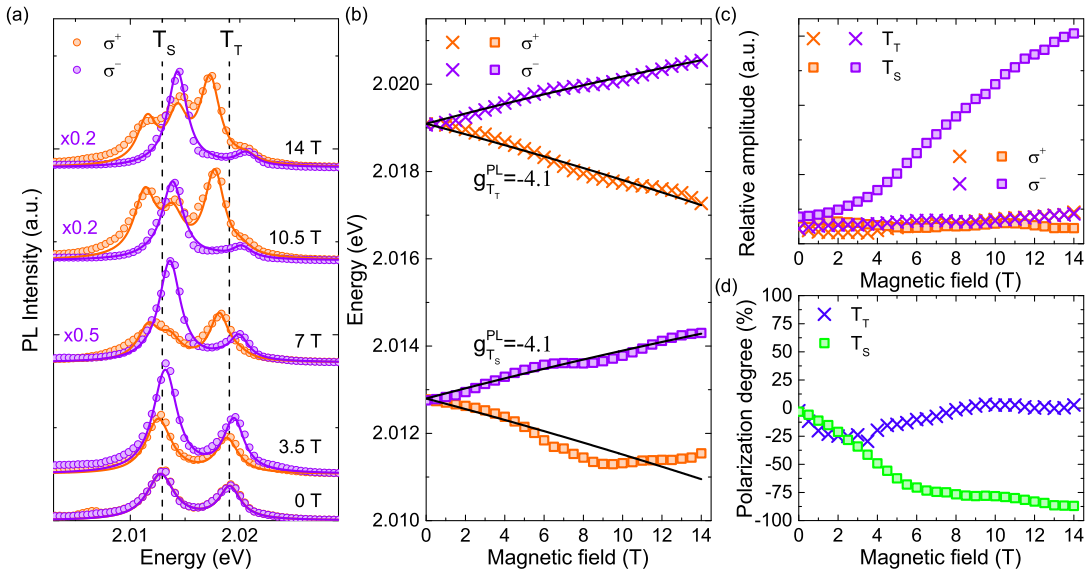

Figure 6.5: (a) Circular-polarisation-resolved low temperature ($T = 4.2$ K) PL spectra (measured with excitation energy $E_{exc} = 2.408$ eV and power $P_{exc} = 20$ μW) of the hBN encapsulated WS_2 in the energy region of singlet (T_S) and triplet (T_T) trions features, measured at selected values of the out-of-plane magnetic field. The dots mark the measured signals, while the lines correspond to the fitted curves. The orange (purple) colour represents the σ^+-polarised (σ^--polarised) spectra. The dashed vertical lines show zero-field energies of trions. The spectra are vertically shifted for clarity and some of those detected at σ^- were multiplied by indicated scaling factors for clarity. (b) Transition energies of the T_S and T_T features extracted from the fits to the PL spectra as a function of the magnetic field. The squares (crosses) refer to the T_S (T_T) resonances. The solid black curves represent fits in accordance to Eq. 6.1. Magnetic field evolutions of (c) the intensities and (d) the polarisation degrees of the T_S and T_T transitions extracted from the fits of the PL spectra.

There is a stark difference when it comes to the change of the amplitudes as compared with the RC results. While the $T_S^{\sigma-}$ feature increase significantly in intensity, as mentioned, the $T_S^{\sigma-}$ state seems to decrease in intensity, while, surprisingly, both $T_T^{\sigma+}$ and $T_T^{\sigma+}$ slightly increase with the applied magnetic field. These effects will be discussed in more detail below.

6.3 Discussion

As was previously mentioned, two effects can be appreciated in both experiments when the magnetic field is applied: the splitting of the energies of circularly polarised trion components and the change of the intensity of the observed trion features. Both effects can be understood mainly by analysing the Zeeman shift of the electronic bands in which electrons and holes involved in trion complexes reside, as shown in Fig. 6.6. Let us first discuss the former effect. The T_T and T_S lines split into two circularly-polarised components and the σ^+ features experience redshift, while the σ^- features are blueshifted. This happens due to the Zeeman shift of electronic bands. Moreover, while all the relevant bands in the K^+ valley shift towards the higher energies, the valence band shifts with a higher rate than conduction bands. Hence the difference between them decreases, and so does the energy of the trions with the recombining electron-hole

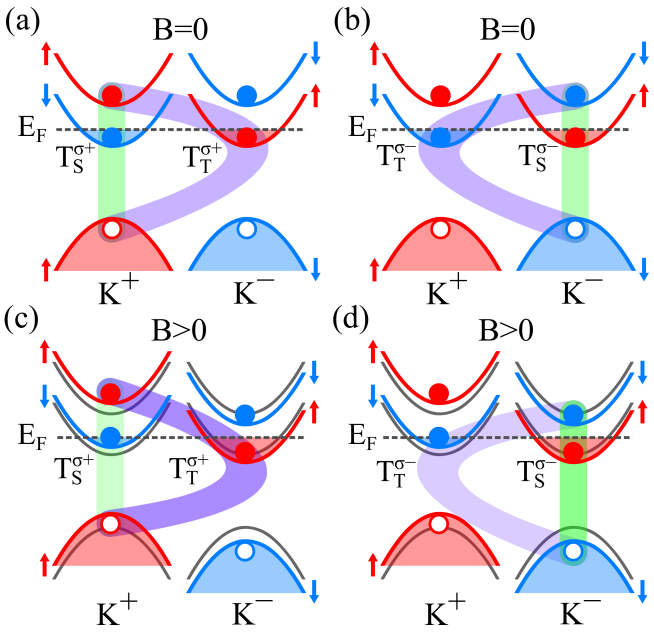

Figure 6.6: Schematic representation of the circularly-polarised (a)/(c) σ^+ and (b)/(d) σ^- singlet (T_S) and triplet (T_T) trions formed at K^+ and K^- points of the Brillouin zone at zero/non-zero magnetic fields. The red (blue) curves indicate the spin-up (spin-down) subbands. The grey curves in (c) and (d) mark the position of subbands at zero field. The electrons (holes) in the conduction (valence) band are illustrated as closed (open) circles. Saturation of green and violet colours is related to the probability of trions formation.

pairs residing in this valley ($T_S^{\sigma+}$ and $T_T^{\sigma+}$). In the K^- valley, the situation is opposite: all the bands shift to lower energies. However, since the valence band sifts at a higher rate than the conduction bands, the energy difference between them increases with the magnetic field, leading to the blueshift of the σ^- features. This observation is in line with previous studies of the Zeeman shift of the bands relevant to trion transitions(154).

The valley Zeeman effect for trions can be quantitatively described by the following equation:

$$E(B) = E_0 \pm \frac{1}{2} g \mu_B B, \tag{6.1}$$

where E_0 is the energy of the given transition at zero magnetic fields, g denotes the effective g-factor of the considered excitonic complex and μ_B is the Bohr magneton. This equation was fitted to the obtained dependencies of trions energies, as shown in Fig. 6.4(b) and Fig. 6.5(b) with solid black curves. In the case of the RC response the extracted g-factors for the singlet and triplet trions differ significantly: $g_{T_S}^{RC} \approx -4.7$ and $g_{T_T}^{RC} \approx -3.0$. The corresponding g factor of the X_A transition is about $g_{X_A}^{RC} \approx -4.2$. On the other hand, the PL results indicate that both trions have practically identical g-factors of ~ -4.1, close to that of the neutral A-exciton. As will be explained later in the text, this discrepancy between two experimental methods is related to the charge redistribution in the two valleys induced by the magnetic field, which also defines the changes in the intensity of circularly polarised trion components.

The evolution of the intensities of the different trion components can also be explained by the Zeeman shift of the electronic bands. For the positive magnetic fields, the conduction bands at the K^+ valley shift towards higher energies, while those at the K^- move towards lower energies. With the assumption of the fixed Fermi energy slightly above the bottom conduction band (consistent with zero-field results and previous works(70, 145, 207, 208)), it leads to the transfer of free electrons from the K^+ to K^- valley. As the concentration of the electrons in the K^- valley increases but decreases in the K^+ valley, and since a probability of the formation of a trion with an additional electron in the given valley is directly related to the free carrier concentration in that valley, the probabilities of the formation of trion complexes will change accordingly. Hence, the intensity of the $T_T^{\sigma+}$ and $T_S^{\sigma-}$ features should increase, while it should decrease in the case of the $T_T^{\sigma-}$ and $T_S^{\sigma+}$ resonances, see Fig. 6.6(c) and (d). This is exactly what is observed in the RC experiments (compare with Fig. 6.4(c)).

The same cannot be said about the results of the PL studies, where only the intensity of the $T_S^{\sigma-}$ component increases significantly, by a factor of 10 up to $B = 14$ T. One can understand this increase as a combined effect of charge transfer into the lowest K^- valley, and of efficient carrier relaxation also towards energy states in the K^- valley. The probability of the formation of the trions involving free carriers in the K^+ valley strongly decreases with increasing magnetic fields due to the valley Zeeman effect and the related electron redistribution between two valleys, as evidenced in the RC experiments. This concerns the $T_T^{\sigma-}$ and the $T_S^{\sigma+}$ complexes, which amplitudes are expected to vanish. On the other hand, the $T_T^{\sigma+}$ state can also efficiently relax into $T_S^{\sigma-}$ state by flipping spins of both the electron and the hole, with the conservation of both spin and momentum. This reasoning explains the observed enhancement of the $T_S^{\sigma-}$ emission, with respect to other trion complexes.

The effect of the magnetic field on the trion amplitudes can be investigated in more detail by inspecting the degree of circular polarisation $\mathscr{P}$, presented for RC experiment in Fig. 6.4(d) and for the PL measurements in Fig. 6.5(d). In the case of the RC experiments, the degrees of circular polarisation of T_T and T_S are opposite, with the very similar dependence and almost linear growth with the increased magnetic field, with a rate close to $\sim 6.6\%.T^{-1}$. The density of states of the 2D conduction band considered does not depend on energy. Since the band energy shifts linearly with the magnetic field, the polarisation of T_T and T_S is also expected to increase linearly with the magnetic field. It is expected to saturate (at $\pm 100\%$) when the bottom conduction band in the K^+ valley reaches the Fermi energy. As the bottom conduction band of the K^+ valley of WS_2 monolayer shifts in the first approximation as $\mu_B B$, the saturation of $\mathcal{P}$ is expected when $\mu_B B_c = E_F$. The extracted value of $B_c \sim 15.2$ T allows one to estimate $E_F \sim 0.9$ meV in this sample. Using the relation $n = m_e E_F/\pi\hbar^2$ and the effective mass of electrons $m_e \sim 0.35$ (52), we can estimate the free carriers concentration to be $n \sim 1.3 \cdot 10^{11}\,\mathrm{cm}^{-2}$. These results clearly show that free electrons in the conduction band can be effectively valley polarised with an external magnetic field. This effect determines the degree of circular polarisation of the different trion species as probed by RC (absorption-like) spectroscopy.

The effect of the free carriers transfer with magnetic field could also explain the difference in the trion g-factors, as observed in the RC experiments. The previous studies on high quality gated monolayers have demonstrated that the trion energies

also depend on the free carrier concentration and that the trion energy increases with free carrier density when the Fermi energy is located in the conduction band(220). Hence, in addition to the aforementioned Zeeman effect, there is an additional factor influencing the trions energies related to the free electrons densities in a given valley. For example, the free carrier density in the K^+ valley decreases with a magnetic field, leading to the decrease of the energy of the two trions with an additional electron in this valley ($T_T^{\sigma-}$ and $T_S^{\sigma+}$). At the same time, the K^- valley population of free electrons increases, leading to the increase of both $T_T^{\sigma+}$ and the $T_S^{\sigma-}$ components energies. This effect can be responsible for an apparent increase of the g-factor of the singlet trion and an apparent decrease of the triplet trion, as observed in the dependencies presented in Fig. 6.4(b).

In the PL studies, the dependence of the degree of circular polarisation $\mathscr{P}$ of the two trion features seems to be much more complicated. $\mathscr{P}$ of T_S increases with the magnetic field, first with a rate of $\sim 12.5\% \cdot T^{-1}$, higher than the one observed in the RC experiment. However, when at $B \sim 6$ T $\mathscr{P}$ reaches $\sim 80\%$, the rate decreases significantly down to $2.1\% \cdot T^{-1}$ and $\mathscr{P}$ reaches -90% at $B = 14$ T. The existence of two regimes in this evolution reflects mechanisms that cannot be elucidated with continuous-wave photoluminescence experiments. Although the intensities of both triplet trion components seem to decrease, the degree of the circular polarisation shows first the evolution towards $\sim -30\%$ (so opposite to the one observed in the RC) close to $B = 4$ T, and then it vanishes. This evolution could result from a subtle interplay between different scattering processes (both radiative and non-radiative types), the effect of photodoping due to the excitation laser, and finally, free carrier redistribution among the two valleys which this experiment does not allow to identify. However, one can conclude that the PL experiments are not the best method to probe the excitonic complexes, as they could be affected by a number of possible non-equilibrium phenomena.

6.4 Conclusions

The magnetic field evolution of negative trion features in a WS_2 monolayer encapsulated in hBN flakes was investigated through reflectance contrast and photoluminescence experiments. The results obtained by these two techniques are surprisingly different. The RC signal can be understood by considering only carrier redistribution between

two valleys, which happens due to the magnetic field induced shift of the band energies with respect to the Fermi energy. This redistribution allows obtaining strong valley-polarisation of free carriers in the system by applying a magnetic field, which subsequently leads to the circular polarisation of the absorption of the trion features. In other words, the valley-polarisation of the carriers can be effectively probed by the polarisation-resolved absorption-like experiments. Moreover, the changing carrier concentration in the sample leads to the change of the energies of the trion features, modifying the values of the effective g-factors of the observed trion complexes. The effect of the carrier redistribution on the PL response is less straightforward. A similar increase of circular polarisation is observed only in the case of the singlet trion. This discrepancy could result from the interplay between competing effects of exciton relaxation to lower energy states (which does not affect the absorption-like experiments) and of changes in the formation probability of polarised components of trion species induced by the carrier redistribution between valleys. The experiments allowed us to extract values of g-factors of both trion complexes and estimate electrons' concentration. The described findings reveal that the valley polarisation of the free electrons can be controlled by magnetic fields and probed by the RC experiments. On the other hand, the PL response highlights the complexity of the different mechanisms involved in the emission related to trions.

7

Conclusions

The results of the experimental studies of the optical properties of semiconducting transition metal dichalcogenides are presented in this thesis. The main focus of this work was put on the fine structure and the Rydberg series of excitons in such materials, which was probed by optical and magneto-optical spectroscopy techniques: photoluminescence and reflectance contrast measurements, including the experiments in high magnetic fields. The original findings were in part already published in peer-reviewed journals, and the other still await the review.

The most important results obtained in this work are:

- The fine structure of the ground exciton states in hBN encapsulated molybdenum disulfide monolayer was extensively studied using the magneto-optical techniques (in Voigt configuration). Contrary to earlier predictions and interpretations present in the literature, it was finally proven that MoS_2 ML is a "darkish" material, i.e. the ground neutral exciton state in this electronic system is dark (optically inactive). The energy separations between bright and dark and also between dark and grey states were determined. Based on these findings, the interpretation of yet puzzling properties of MoS_2 monolayers, such as polarization effects and temperature dependence of the photoluminescence signal, was proposed.

- For the first time, the out-of-plane g-factors of dark excitons in MoS_2 and $MoSe_2$ MLs were extracted using a magnetic field applied in the "tilted-field" configuration. The obtained values provided additional proof about the interpretation of these states as dark excitons.

- Magnetic field in Voigt configuration was also used to brighten not only the ground state of dark exciton in WSe_2 MLs but also, for the first time, its excited states. The observation of the Rydberg series of dark and excitons allowed us to extract the long-sought value of the amplitude of the spin-orbit splitting of the conduction band.

- The analysis of the Rydberg series of two linearly polarised excitons of bulk rhenium disulfide has shown that these states, again contrary to some of the interpretations proposed in the literature, originate from the same bandgap in the band structure.

- The magnetophotoluminescence studies have shown that not only two bright but also two dark exciton series can be found in bulk ReS_2. Moreover, their complex interaction, visualised by application of the magnetic field, proved that all these states originate from the same point in the Brillouin zone and, therefore, are probably the result of the giant exchange splitting.

- It was shown that the out-of-plane magnetic field can be used to effectively induce valley polarisation of free carries in TMDs monolayers, with the example of study of WS_2 monolayer, and that this effect can be probed by the reflection contrast technique. In contrast, it was shown that the photoluminescence could not be used to probe the valley polarisation of free carriers straightforwardly, as the complex relaxation processes largely affect the emission spectra and cover some of the effects related to the carrier polarisation.

List of publications

During the doctoral studies, the Author took part in the research that resulted in a few already published articles and a few more, still being in preparation, manuscripts. The results of the studies were also presented at scientific conferences.

List of publications related to this work:

- C. Robert, B. Han, **P. Kapuściński**, A. Delhomme, C. Faugeras, T. Amand, M.R. Molas, M. Bartos, K. Watanabe, T. Taniguchi, B. Urbaszek, M. Potemski and X. Marie, "Measurement of the spin-forbidden dark excitons in MoS_2 and $MoSe_2$ monolayers," *Nat Commun* **11**, 4037 (2020).

- **P. Kapuściński**, D. Vaclavkova, M. Grzeszczyk, A. O. Slobodeniuk, K. Nogajewski, M. Bartos, K. Watanabe, T. Taniguchi, C. Faugeras, A. Babiński, M. Potemski and M. R. Molas, "Valley polarization of singlet and triplet trions in WS_2 monolayer in magnetic fields," *Phys. Chem. Chem. Phys.* **22**, 19155-19161 (2020).

- **P. Kapuściński**, A. Delhomme, D. Vaclavkova, A. O. Slobodeniuk, M. Grzeszczyk, M. Bartos, K. Watanabe, T. Taniguchi, C. Faugeras and M. Potemski, "Rydberg series of dark excitons and the conduction band spin-orbit splitting in monolayer WSe_2," *Commun Phys* **4**, 186 (2021).

- **P. Kapuściński**, J. Dzian, C. Rodríguez-Fernández, A. O. Slobodeniuk, J. Jadczak, L. Bryja, C. Faugeras, D. Basko and M. Potemski, "Exchange-split multiple Rydberg series of excitons in anisotropic quasi two-dimensional ReS_2," *to be published.*

List of other publications, not included in this thesis:

- J. Jadczak, L. Bryja, J. Kutrowska-Girzycka, **P. Kapuściński**, M. Bieniek, Y. S. Huang and P. Hawrylak, "Room temperature multi-phonon upconversion photoluminescence in monolayer semiconductor WS_2," *Nat Commun* **10**, 107 (2019).

- M. R. Molas, A. O. Slobodeniuk, T. Kazimierczuk, K. Nogajewski, M. Bartos, **P. Kapuściński**, K. Oreszczuk, K. Watanabe, T. Taniguchi, C. Faugeras, P. Kossacki, D. M. Basko and M. Potemski, "Probing and Manipulating Valley Coherence of Dark Excitons in Monolayer WSe_2," *Phys. Rev. Lett.* **123**, 096803 (2019).

- M. Zinkiewicz, A. O. Slobodeniuk, T. Kazimierczuk, **P. Kapuściński**, K. Oreszczuk, M. Grzeszczyk, M. Bartos, K. Nogajewski, K. Watanabe, T. Taniguchi, C. Faugeras, P. Kossacki, M. Potemski, A. Babiński and M. R. Molas, "Neutral and charged dark excitons in monolayer WS_2," *Nanoscale* **12**, 18153-18159 (2020).

- M. Zinkiewicz, T. Woźniak, T. Kazimierczuk, **P. Kapuściński**, K. Oreszczuk, M. Grzeszczyk, M. Bartos, K. Nogajewski, K. Watanabe, T. Taniguchi, C. Faugeras, P. Kossacki, M. Potemski, A. Babiński and M. R. Molas, "Excitonic complexes in n-doped WS_2 monolayer," *Nano Lett.* **21**, 6, 2519–2525 (2021).

- D. Vaclavkova, M. Palit, J. Wyzula, S. Ghosh, A. Delhomme, S. Maity, **P. Kapuściński**, A. Ghosh, M. Veis, M. Grzeszczyk, C. Faugeras, M. Orlita, S. Datta, M. Potemski, "Magnon-polarons in van der Waals antiferromagnet $FePS_3$," *arXiv* 2108.10945 (2021).

List of conference presentations:

- **P. Kapuściński**, A. Delhomme, D. Vaclavkova, K. Nogajewski, M. Bartos, M. R. Molas, C. Faugeras and M. Potemski, "Magnetic field induced valley polarization of singlet and triplet trions in monolayer WS_2," *Graphene Study 2019 on Science and Technologies of 2D Materials*, 04-08.02.2019, Obergurgl, Austria, poster presentation.

- **P. Kapuściński**, D. Vaclavkova, M. Grzeszczyk, M. Bartos, K. Nogajewski, K. Watanabe, T. Taniguchi, A. Babiński, C. Faugeras, M. Potemski, and M. R. Molas, "Magnetic field induced valley polarization of singlet and triplet trions in monolayer WS_2," *4th International Conference on Physics of 2D Crystals*, 11-14.06.2019, Hangzhou, China, poster presentation.

- **P. Kapuściński**, D. Vaclavkova, M. Grzeszczyk, M. Bartos, K. Nogajewski, K. Watanabe, T. Taniguchi, A. Babiński, C. Faugeras, M. Potemski, and M. R. Molas, "Magnetic field induced valley polarization of singlet and triplet trions in monolayer WS_2," *EMFL User meeting 2019*, 25.06.2019, Warsaw, Poland, poster presentation.

- **P. Kapuściński**, J. Dzian, A. O. Slobodeniuk, C. Rodriguez-Fernandez, Y. S. Huang, J. Jadczak, L. Bryja, C. Faugeras and M. Potemski, "Rydberg series of bright and dark excitons in ReS_2," *Joint annual meeting on International Research Projects, CNRS '2DM' and 'TeraMIR'*, 30.11-01.12.2020, online conference, oral presentation.

- **P. Kapuściński**, A. Delhomme, D. Vaclavkova, A. O. Slobodeniuk, M. Grzeszczyk, M. Bartos, K. Watanabe, T. Taniguchi, C. Faugeras and M. Potemski, "Excited states of dark excitons and spin-orbit splitting of the conduction band in tungsten diselenide monolayer," *Optics of Excitons in Confined Systems OECS 17*, 30.08-02.09.2021, online conference, oral presentation.

- **P. Kapuściński**, A. Delhomme, D. Vaclavkova, A. O. Slobodeniuk, M. Grzeszczyk, M. Bartos, K. Watanabe, T. Taniguchi, C. Faugeras and M. Potemski, "Rydberg series of dark excitons and spin-orbit splitting of the conduction band in WSe_2 monolayer," *49th International School & Conference on the Physics of Semiconductors "Jaszowiec 2021"*, 01-10.09.2021, online conference, oral presentation.

- **P. Kapuściński**, A. Delhomme, D. Vaclavkova, A. O. Slobodeniuk, M. Grzeszczyk, M. Bartos, K. Watanabe, T. Taniguchi, C. Faugeras and M. Potemski, "Excited states of dark excitons and spin-orbit splitting of the conduction band in tungsten diselenide monolayer," *Graphene and other 2D materials*, 13-15.09.2021, online conference, oral presentation.

References

[1] J. Frenkel, "On the transformation of light into heat in solids. II," Phys. Rev., vol. 37, pp. 1276–1294, May 1931. 2

[2] G. H. Wannier, "The structure of electronic excitation levels in insulating crystals," Phys. Rev., vol. 52, pp. 191–197, Aug 1937. 2

[3] G. H. Wannier, Elements of solid state theory. University Press, 1959. 2

[4] W. Kohn, "Shallow impurity states in silicon and germanium," vol. 5 of Solid State Physics, pp. 257–320, Academic Press, 1957. 2

[5] P. Y. Yu and M. Cardona, Optical Properties I, pp. 243–344. Berlin, Heidelberg: Springer Berlin Heidelberg, 2010. 3

[6] I. Strzalkowski, S. Joshi, and C. R. Crowell, "Dielectric constant and its temperature dependence for GaAs, CdTe, and ZnSe," Applied Physics Letters, vol. 28, no. 6, pp. 350–352, 1976. 4

[7] W. Nakwaski, "Effective masses of electrons and heavy holes in GaAs, InAs, A1As and their ternary compounds," Physica B: Condensed Matter, vol. 210, no. 1, pp. 1–25, 1995. 4

[8] X.-F. He, "Excitons in anisotropic solids: The model of fractional-dimensional space," Phys. Rev. B, vol. 43, pp. 2063–2069, Jan 1991. 5, 61

[9] M. R. Molas, A. O. Slobodeniuk, K. Nogajewski, M. Bartos, L. Bala, A. Babiński, K. Watanabe, T. Taniguchi, C. Faugeras, and M. Potemski, "Energy spectrum of two-dimensional excitons in a nonuniform dielectric medium," Phys. Rev. Lett., vol. 123, p. 136801, Sep 2019. 5, 13, 42, 49, 50, 54, 61, 87

[10] B. Hönerlage, Symmetry and Symmetry-Breaking in Semiconductors [electronic resource] : Fine Structure of Exciton States / by Bernd Hönerlage, Ivan Pelant. Springer Tracts in Modern Physics, 279, Cham: Springer International Publishing, 1st ed. 2018. ed., 2018. 6, 7

[11] T. Amand and X. Marie, Exciton Spin Dynamics in Semiconductor Quantum Wells, pp. 55–89. Berlin, Heidelberg: Springer Berlin Heidelberg, 2008. 7

[12] M. Bayer, G. Ortner, O. Stern, A. Kuther, A. A. Gorbunov, A. Forchel, P. Hawrylak, S. Fafard, K. Hinzer, T. L. Reinecke, S. N. Walck, J. P. Reithmaier, F. Klopf, and F. Schäfer, "Fine structure of neutral and charged excitons in self-assembled In(Ga)As/(Al)GaAs quantum dots," Phys. Rev. B, vol. 65, p. 195315, May 2002. 7, 70

[13] K. Cho, "Unified theory of symmetry-breaking effects on excitons in cubic and wurtzite structures," Phys. Rev. B, vol. 14, pp. 4463–4482, Nov 1976. 7

[14] G. Pikus and G. Bir, "Exchange interaction in excitons in semiconductors," Sov. Phys. JETP, vol. 33, no. 1, 1971. Zh. Eksp. Teor. Fiz. **60**, 195 (1971). 7

[15] M. A. Lampert, "Mobile and immobile effective-mass-particle complexes in nonmetallic solids," Phys. Rev. Lett., vol. 1, pp. 450–453, Dec 1958. 8

[16] K. Kheng, R. T. Cox, M. Y. d' Aubigné, F. Bassani, K. Saminadayar, and S. Tatarenko, "Observation of negatively charged excitons x^- in semiconductor quantum wells," Phys. Rev. Lett., vol. 71, pp. 1752–1755, Sep 1993. 8, 83

[17] G. Finkelstein, H. Shtrikman, and I. Bar-Joseph, "Negatively and positively charged excitons in GaAs/Al_xGa_{1-x}As quantum wells," Phys. Rev. B, vol. 53, p. 1709, Jan 1996. 8

[18] R. C. Miller, D. A. Kleinman, A. C. Gossard, and O. Munteanu, "Biexcitons in GaAs quantum wells," Phys. Rev. B, vol. 25, pp. 6545–6547, May 1982. 8

[19] A. Hartmann, Y. Ducommun, E. Kapon, U. Hohenester, and E. Molinari, "Few-particle effects in semiconductor quantum dots: Observation of multicharged excitons," Phys. Rev. Lett., vol. 84, pp. 5648–5651, Jun 2000. 8

[20] B. Urbaszek, R. J. Warburton, K. Karrai, B. D. Gerardot, P. M. Petroff, and J. M. Garcia, "Fine structure of highly charged excitons in semiconductor quantum dots," Phys. Rev. Lett., vol. 90, p. 247403, Jun 2003. 8

[21] M. Ikezawa, Y. Masumoto, T. Takagahara, and S. V. Nair, "Biexciton and triexciton states in quantum dots in the weak confinement regime," Phys. Rev. Lett., vol. 79, pp. 3522–3525, Nov 1997. 8

[22] M. R. Molas, A. A. L. Nicolet, A. Babiński, and M. Potemski, "Quadexciton cascade and fine-structure splitting of the triexciton in a single quantum dot," EPL (Europhysics Letters), vol. 113, p. 17004, jan 2016. 8

[23] J. Wilson and A. Yoffe, "The transition metal dichalcogenides discussion and interpretation of the observed optical, electrical and structural properties," Advances in Physics, vol. 18, no. 73, pp. 193–335, 1969. 8, 9, 10

[24] J. Jadczak, J. Kutrowska-Girzycka, T. Smolenski, P. Kossacki, Y. S. Huang, and L. Bryja, "Exciton binding energy and hydrogenic rydberg series in layered ReS2," Scientific Reports, vol. 9, no. 1, p. 1578, 2019. 8, 15, 58, 59, 60

[25] M. Chhowalla, H. S. Shin, G. Eda, L.-J. Li, K. P. Loh, and H. Zhang, "The chemistry of two-dimensional layered transition metal dichalcogenide nanosheets," Nature Chemistry, vol. 5, pp. 263–275, Apr 2013. 9, 57

[26] E. A. Marseglia, "Transition metal dichalcogenides and their intercalates," International Reviews in Physical Chemistry, vol. 3, no. 2, pp. 177–216, 1983. 9, 10

[27] M. B. Dines, "Lithium intercalation via n-butyllithium of the layered transition metal dichalcogenides," Materials Research Bulletin, vol. 10, no. 4, pp. 287–291, 1975. 9

[28] J. N. Coleman, M. Lotya, A. O'Neill, S. D. Bergin, P. J. King, U. Khan, K. Young, A. Gaucher, S. De, R. J. Smith, I. V. Shvets, S. K. Arora, G. Stanton, H.-Y. Kim, K. Lee, G. T. Kim, G. S. Duesberg, T. Hallam, J. J. Boland, J. J. Wang, J. F. Donegan, J. C. Grunlan, G. Moriarty, A. Shmeliov, R. J. Nicholls, J. M. Perkins, E. M. Grieveson, K. Theuwissen, D. W. McComb, P. D. Nellist, and V. Nicolosi, "Two-dimensional nanosheets produced by liquid exfoliation of layered materials," Science, vol. 331, no. 6017, pp. 568–571, 2011. 9

[29] K. S. Novoselov, D. Jiang, F. Schedin, T. J. Booth, V. V. Khotkevich, S. V. Morozov, and A. K. Geim, "Two-dimensional atomic crystals," Proc. Natl. Acad. Sci. U. S. A., vol. 102, no. 30, p. 10451, 2005. 9, 10, 83

[30] K. F. Mak, C. Lee, J. Hone, J. Shan, and T. F. Heinz, "Atomically thin MoS_2: A new direct-gap semiconductor," Phys. Rev. Lett., vol. 105, p. 136805, Sep 2010. 9, 10, 25, 58, 83

[31] P. Joensen, R. Frindt, and S. Morrison, "Single-layer MoS2," Materials Research Bulletin, vol. 21, no. 4, pp. 457–461, 1986. 9

[32] M. Acerce, D. Voiry, and M. Chhowalla, "Metallic 1T phase MoS2 nanosheets as supercapacitor electrode materials," Nature Nanotechnology, vol. 10, pp. 313–318, Apr 2015. 9

[33] J. Wildervanck and F. Jellinek, "The dichalcogenides of technetium and rhenium," Journal of the Less Common Metals, vol. 24, no. 1, pp. 73–81, 1971. 10, 14

[34] J. V. Marzik, R. Kershaw, K. Dwight, and A. Wold, "Photoelectronic properties of ReS2 and ReSe2 single crystals," Journal of Solid State Chemistry, vol. 51, no. 2, pp. 170–175, 1984. 10

[35] A. M. Goldberg, A. R. Beal, F. A. Lévy, and E. A. Davis, "The low-energy absorption edge in 2H-MoS2 and 2H-MoSe2," The Philosophical Magazine: A Journal of Theoretical Experimental and Applied Physics, vol. 32, no. 2, pp. 367–378, 1975. 10

[36] A. R. Beal and W. Y. Liang, "Excitons in 2H-WSe2 and 3R-WS2," Journal of Physics C: Solid State Physics, vol. 9, pp. 2459–2466, jun 1976. 10

[37] R. A. Neville and B. L. Evans, "The band edge excitons in 2H-MoS2," physica status solidi (b), vol. 73, no. 2, pp. 597–606, 1976. 10

[38] M. Tanaka, H. Fukutani, and G. Kuwabara, "Excitons in VI B transition metal dichalcogenides," Journal of the Physical Society of Japan, vol. 45, no. 6, pp. 1899–1904, 1978. 10

[39] C. H. Ho, P. C. Liao, Y. S. Huang, and K. K. Tiong, "Temperature dependence of energies and broadening parameters of the band-edge excitons of ReS_2 and $ReSe_2$," Phys. Rev. B, vol. 55, pp. 15608–15613, Jun 1997. 10, 15

[40] C. Ho, P. Liao, Y. Huang, and K. Tiong, "Piezoreflectance study of the band-edge excitons of ReS2," Solid State Communications, vol. 103, no. 1, pp. 19–23, 1997. 10, 15

[41] R. Frindt, "The optical properties of single crystals of WSe2 and MoTe2," Journal of Physics and Chemistry of Solids, vol. 24, no. 9, pp. 1107–1108, 1963. 10

[42] R. F. Frindt, A. D. Yoffe, and F. P. Bowden, "Physical properties of layer structures : optical properties and photoconductivity of thin crystals of molybdenum disulphide," Proceedings of the Royal Society of London. Series A. Mathematical and Physical Sciences, vol. 273, no. 1352, pp. 69–83, 1963. 10

[43] B. L. Evans, P. A. Young, and R. W. Ditchburn, "Optical absorption and dispersion in molybdenum disulphide," Proceedings of the Royal Society of London. Series A. Mathematical and Physical Sciences, vol. 284, no. 1398, pp. 402–422, 1965. 10

[44] R. F. Frindt, "Single crystals of MoS2 several molecular layers thick," Journal of Applied Physics, vol. 37, no. 4, pp. 1928–1929, 1966. 10

[45] R. A. Bromley, R. B. Murray, and A. D. Yoffe, "The band structures of some transition metal dichalcogenides. III. group VIA: trigonal prism materials," Journal of Physics C: Solid State Physics, vol. 5, pp. 759–778, apr 1972. 10

[46] K. S. Novoselov, A. K. Geim, S. V. Morozov, D. Jiang, Y. Zhang, S. V. Dubonos, I. V. Grigorieva, and A. A. Firsov, "Electric field effect in atomically thin carbon films," Science, vol. 306, no. 5696, pp. 666–669, 2004. 10

[47] A. Splendiani, L. Sun, Y. Zhang, T. Li, J. Kim, C.-Y. Chim, G. Galli, and F. Wang, "Emerging photoluminescence in monolayer MoS2," Nano Letters, vol. 10, no. 4, p. 1271, 2010. 10, 58

[48] A. Kuc, N. Zibouche, and T. Heine, "Influence of quantum confinement on the electronic structure of the transition metal sulfide TS_2," Phys. Rev. B, vol. 83, p. 245213, Jun 2011. 10, 58

[49] A. Kumar and P. K. Ahluwalia, "Electronic structure of transition metal dichalcogenides monolayers 1H-MX2 (M = Mo, W; X = S, Se, Te) from ab-initio theory: new direct band gap semiconductors," The European Physical Journal B, vol. 85, p. 186, Jun 2012. 10, 11, 25, 58

[50] J. K. Ellis, M. J. Lucero, and G. E. Scuseria, "The indirect to direct band gap transition in multilayered MoS2 as predicted by screened hybrid density functional theory," Applied Physics Letters, vol. 99, no. 26, p. 261908, 2011. 10, 58

[51] T. Li and G. Galli, "Electronic properties of MoS2 nanoparticles," The Journal of Physical Chemistry C, vol. 111, pp. 16192–16196, Nov 2007. 11

[52] A. Kormányos, G. Burkard, M. Gmitra, J. Fabian, V. Zólyomi, N. D. Drummond, and V. Fal'ko, "k · p theory for two-dimensional transition metal dichalcogenide semiconductors," 2D Materials, vol. 2, no. 2, p. 022001, 2015. 11, 13, 25, 26, 28, 41, 42, 49, 55, 84, 85, 94

[53] W. Yao, D. Xiao, and Q. Niu, "Valley-dependent optoelectronics from inversion symmetry breaking," Phys. Rev. B, vol. 77, p. 235406, Jun 2008. 11, 12, 25

[54] D. Xiao, G.-B. Liu, W. Feng, X. Xu, and W. Yao, "Coupled spin and valley physics in monolayers of MoS_2 and other group-VI dichalcogenides," Phys. Rev. Lett., vol. 108, p. 196802, May 2012. 11, 12, 13, 25

[55] Z. Y. Zhu, Y. C. Cheng, and U. Schwingenschlögl, "Giant spin-orbit-induced spin splitting in two-dimensional transition-metal dichalcogenide semiconductors," Phys. Rev. B, vol. 84, p. 153402, Oct 2011. 11, 25, 84

[56] T. Cheiwchanchamnangij and W. R. L. Lambrecht, "Quasiparticle band structure calculation of monolayer, bilayer, and bulk MoS_2," Phys. Rev. B, vol. 85, p. 205302, May 2012. 11

[57] K. Kośmider and J. Fernández-Rossier, "Electronic properties of the MoS_2-WS_2 heterojunction," Phys. Rev. B, vol. 87, p. 075451, Feb 2013. 11, 26, 41, 85

[58] G.-B. Liu, W.-Y. Shan, Y. Yao, W. Yao, and D. Xiao, "Three-band tight-binding model for monolayers of group-VIB transition metal dichalcogenides," Phys. Rev. B, vol. 88, p. 085433, 2013. 13, 26, 55

[59] A. Chernikov, T. C. Berkelbach, H. M. Hill, A. Rigosi, Y. Li, O. B. Aslan, D. R. Reichman, M. S. Hybertsen, and T. F. Heinz, "Exciton binding energy and nonhydrogenic rydberg series in monolayer WS_2," Phys. Rev. Lett., vol. 113, p. 076802, Aug 2014. 13, 83, 87

[60] M. M. Ugeda, A. J. Bradley, S.-F. Shi, F. H. da Jornada, Y. Zhang, D. Y. Qiu, W. Ruan, S.-K. Mo, Z. Hussain, Z.-X. Shen, F. Wang, S. G. Louie, and M. F. Crommie, "Giant bandgap renormalization and excitonic effects in a monolayer transition metal dichalcogenide semiconductor," Nat. Mater., vol. 13, pp. 1091–1095, Dec 2014. 13, 84

[61] K. He, N. Kumar, L. Zhao, Z. Wang, K. F. Mak, H. Zhao, and J. Shan, "Tightly Bound Excitons in Monolayer WSe_2," Phys. Rev. Lett., vol. 113, p. 026803, Jul 2014. 13

[62] T. Cao, G. Wang, W. Han, H. Ye, C. Zhu, J. Shi, Q. Niu, P. Tan, E. Wang, B. Liu, and J. Feng, "Valley-selective circular dichroism of monolayer molybdenum disulphide," Nat. Commun., vol. 3, p. 887, 2012. 13

[63] K. F. Mak, K. He, J. Shan, and T. F. Heinz, "Control of valley polarization in monolayer MoS2 by optical helicity," Nat. Nanotechnol., vol. 7, p. 494, 2012. 13, 42

[64] H. Zeng, J. Dai, W. Yao, D. Xiao, and X. Cui, "Valley polarization in MoS2 monolayers by optical pumping," Nature Nanotechnology, vol. 7, pp. 490–493, Aug 2012. 13, 42

[65] T. C. Berkelbach, M. S. Hybertsen, and D. R. Reichman, "Theory of neutral and charged excitons in monolayer transition metal dichalcogenides," Phys. Rev. B, vol. 88, p. 045318, Jul 2013. 13

[66] M. R. Molas, C. Faugeras, A. O. Slobodeniuk, K. Nogajewski, M. Bartos, D. M. Basko, and M. Potemski, "Brightening of dark excitons in monolayers of semiconducting transition metal dichalcogenides," 2D Materials, vol. 4, no. 2, p. 021003, 2017. 13, 26, 28, 31, 58, 66, 88

[67] X.-X. Zhang, T. Cao, Z. Lu, Y.-C. Lin, F. Zhang, Y. Wang, Z. Li, J. C. Hone, J. A. Robinson, D. Smirnov, S. G. Louie, and T. F. Heinz, "Magnetic brightening and control of dark excitons in monolayer WSe2," Nature Nanotechnology, vol. 12, p. 883, Jun 2017. Article. 13, 58

[68] K. F. Mak, K. He, C. Lee, G. H. Lee, J. Hone, T. F. Hein, and J. Shan, "Tightly bound trions in monolayer MoS2," Nat. Mater., vol. 12, p. 207, 2013. 13, 83

[69] J. S. Ross, S. Wu, H. Yu, N. J. Ghimire, A. M. Jones, G. Aivazian, J. Yan, D. G. Mandrus, D. Xiao, W. Yao, and X. Xu, "Electrical control of neutral and charged excitons in a monolayer semiconductor," Nat. Commun., vol. 4, p. 1474, 2012. 13, 83

[70] J. Jadczak, J. Kutrowska-Girzycka, P. Kapuściński, Y. S. Huang, A. Wójs, and L. Bryja, "Probing of free and localized excitons and trions in atomically thin WSe_2, WS_2, $MoSe_2$ and MoS_2 in photoluminescence and reflectivity experiments," Nanotechnology, vol. 28, no. 39, p. 395702, 2017. 13, 42, 84, 87, 88, 89, 93

[71] Y. You, X.-X. Zhang, T. C. Berkelbach, M. S. Hybertsen, D. R. Reichman, and T. F. Heinz, "Observation of biexcitons in monolayer WSe2," Nat. Phys., vol. 11, p. 477, 2015. 13

[72] A. Steinhoff, M. Florian, A. Singh, K. Tran, M. Kolarczik, S. Helmrich, A. W. Achtstein, U. Woggon, N. Owschimikow, F. Jahnke, and X. Li, "Biexciton fine structure in monolayer transition metal dichalcogenides," Nature Physics, vol. 14, pp. 1199–1204, Dec 2018. 13

[73] J. Huang, T. B. Hoang, and M. H. Mikkelsen, "Probing the origin of excitonic states in monolayer WSe2," Scientific Reports, vol. 6, p. 22414, Mar 2016. 13

[74] S. Zhang, C.-G. Wang, M.-Y. Li, D. Huang, L.-J. Li, W. Ji, and S. Wu, "Defect structure of localized excitons in a WS_2 monolayer," Phys. Rev. Lett., vol. 119, p. 046101, Jul 2017. 13

[75] F. Cadiz, E. Courtade, C. Robert, G. Wang, Y. Shen, H. Cai, T. Taniguchi, K. Watanabe, H. Carrere, D. Lagarde, M. Manca, T. Amand, P. Renucci, S. Tongay, X. Marie, and B. Urbaszek, "Excitonic linewidth approaching the homogeneous limit in MoS_2-based van der Waals heterostructures," Phys. Rev. X, vol. 7, p. 021026, May 2017. 13, 28, 31, 37, 41, 44

[76] A. V. Stier, N. P. Wilson, K. A. Velizhanin, J. Kono, X. Xu, and S. A. Crooker, "Magnetooptics of exciton Rydberg States in a monolayer semiconductor," Phys. Rev. Lett., vol. 120, p. 057405, Feb 2018. 13, 41, 49, 50

[77] S.-Y. Chen, Z. Lu, T. Goldstein, J. Tong, A. Chaves, J. Kunstmann, L. S. R. Cavalcante, T. Woźniak, G. Seifert, D. R. Reichman, T. Taniguchi, K. Watanabe, D. Smirnov, and J. Yan, "Luminescent emission of excited rydberg excitons from monolayer WSe2," Nano Letters, vol. 19, pp. 2464–2471, Apr 2019. 13, 49, 50

[78] E. Liu, J. van Baren, T. Taniguchi, K. Watanabe, Y.-C. Chang, and C. H. Lui, "Magnetophotoluminescence of exciton rydberg states in monolayer WSe_2," Phys. Rev. B, vol. 99, p. 205420, May 2019. 13, 49, 50

[79] M. Goryca, J. Li, A. V. Stier, T. Taniguchi, K. Watanabe, E. Courtade, S. Shree, C. Robert, B. Urbaszek, X. Marie, and S. A. Crooker, "Revealing exciton masses and dielectric properties of monolayer semiconductors with high magnetic fields," Nature Communications, vol. 10, p. 4172, Sep 2019. 13, 31, 37, 41

[80] M. R. Molas, A. O. Slobodeniuk, T. Kazimierczuk, K. Nogajewski, M. Bartos, P. Kapuściński, K. Oreszczuk, K. Watanabe, T. Taniguchi, C. Faugeras, P. Kossacki, D. M. Basko, and M. Potemski, "Probing and manipulating valley coherence of dark excitons in monolayer WSe_2," Phys. Rev. Lett., vol. 123, p. 096803, Aug 2019. 13, 28, 29, 31, 41, 42, 43, 44, 50, 53

[81] G. Wang, C. Robert, M. M. Glazov, F. Cadiz, E. Courtade, T. Amand, D. Lagarde, T. Taniguchi, K. Watanabe, B. Urbaszek, and X. Marie, "In-plane propagation of light in transition metal dichalcogenide monolayers: Optical selection rules," Phys. Rev. Lett., vol. 119, p. 047401, Jul 2017. 13, 26, 27, 41, 43, 47, 50, 58

[82] C. Robert, T. Amand, F. Cadiz, D. Lagarde, E. Courtade, M. Manca, T. Taniguchi, K. Watanabe, B. Urbaszek, and X. Marie, "Fine structure and lifetime of dark excitons in transition metal dichalcogenide monolayers," Phys. Rev. B, vol. 96, p. 155423, Oct 2017. 13, 27, 41, 42, 43, 44, 50

[83] D. Vaclavkova, J. Wyzula, K. Nogajewski, M. Bartos, A. O. Slobodeniuk, C. Faugeras, M. Potemski, and M. R. Molas, "Singlet and triplet trions in WS2 monolayer encapsulated in hexagonal boron nitride," Nanotechnology, vol. 29, no. 32, p. 325705, 2018. 13, 87, 88

[84] T. P. Lyons, S. Dufferwiel, M. Brooks, F. Withers, T. Taniguchi, K. Watanabe, K. S. Novoselov, G. Burkard, and A. I. Tartakovskii, "The valley zeeman effect in inter- and intra-valley trions in monolayer WSe2," Nature Communications, vol. 10, no. 1, p. 2330, 2019. 13

[85] A. Arora, T. Deilmann, T. Reichenauer, J. Kern, S. Michaelis de Vasconcellos, M. Rohlfing, and R. Bratschitsch, "Excited-state trions in monolayer WS_2," Phys. Rev. Lett., vol. 123, p. 167401, Oct 2019. 13, 88

[86] M. Kertesz and R. Hoffmann, "Octahedral vs. trigonal-prismatic coordination and clustering in transition-metal dichalcogenides," Journal of the American Chemical Society, vol. 106, pp. 3453–3460, Jun 1984. 14, 57

[87] H.-J. Lamfers, A. Meetsma, G. Wiegers, and J. de Boer, "The crystal structure of some rhenium and technetium dichalcogenides," Journal of Alloys and Compounds, vol. 241, no. 1, pp. 34 – 39, 1996. 14, 57

[88] H. H. Murray, S. P. Kelty, R. R. Chianelli, and C. S. Day, "Structure of rhenium disulfide," Inorganic Chemistry, vol. 33, pp. 4418–4420, Sep 1994. 14, 57

[89] J. M. Urban, M. Baranowski, A. Kuc, Ł. Kłopotowski, A. Surrente, Y. Ma, D. Włodarczyk, A. Suchocki, D. Ovchinnikov, T. Heine, D. K. Maude, A. Kis, and P. Plochocka, "Non equilibrium anisotropic excitons in atomically thin ReS2," 2D Materials, vol. 6, p. 015012, nov 2018. 14, 58, 59

[90] X. Wang, K. Shinokita, H. E. Lim, N. B. Mohamed, Y. Miyauchi, N. T. Cuong, S. Okada, and K. Matsuda, "Direct and indirect exciton dynamics in few-layered ReS2 revealed by photoluminescence and pump-probe spectroscopy," Advanced Functional Materials, vol. 29, no. 6, p. 1806169, 2019. 14, 58, 59

[91] I. Gutiérrez-Lezama, B. A. Reddy, N. Ubrig, and A. F. Morpurgo, "Electroluminescence from indirect band gap semiconductor ReS_2," 2D Materials, vol. 3, p. 045016, oct 2016. 14, 58

[92] C. H. Ho, Y. S. Huang, K. K. Tiong, and P. C. Liao, "Absorption-edge anisotropy in ReS_2 and $ReSe_2$ layered semiconductors," Phys. Rev. B, vol. 58, pp. 16130–16135, Dec 1998. 14, 15, 58

[93] C. H. Ho, Y. S. Huang, J. L. Chen, T. E. Dann, and K. K. Tiong, "Electronic structure of ReS_2 and $ReSe_2$ from first-principles calculations, photoelectron spectroscopy, and electrolyte electroreflectance," Phys. Rev. B, vol. 60, pp. 15766–15771, Dec 1999. 14, 15, 58

[94] C. H. Ho, H. W. Lee, and C. C. Wu, "Polarization sensitive behaviour of the band-edge transitions in ReS2 and ReSe2 layered semiconductors," Journal of Physics: Condensed Matter, vol. 16, pp. 5937–5944, aug 2004. 14, 15, 58

[95] S. J. Zelewski and R. Kudrawiec, "Photoacoustic and modulated reflectance studies of indirect and direct band gap in van der Waals crystals," Scientific Reports, vol. 7, p. 15365, Nov 2017. 14, 58

[96] S. M. Gunasekera, D. Wolverson, L. S. Hart, and M. Mucha-Kruczynski, "Electronic band structure of rhenium dichalcogenides," Journal of Electronic Materials, vol. 47, pp. 4314–4320, Aug 2018. 14, 58

[97] J. P. Echeverry and I. C. Gerber, "Theoretical investigations of the anisotropic optical properties of distorted 1t res2 and rese2 monolayers, bilayers, and in the bulk limit," Phys. Rev. B, vol. 97, p. 075123, Feb 2018. 14, 15, 58, 80

[98] D. Biswas, A. M. Ganose, R. Yano, J. M. Riley, L. Bawden, O. J. Clark, J. Feng, L. Collins-Mcintyre, M. T. Sajjad, W. Meevasana, T. K. Kim, M. Hoesch, J. E. Rault, T. Sasagawa, D. O. Scanlon, and P. D. C. King, "Narrow-band anisotropic electronic structure of ReS_2," Phys. Rev. B, vol. 96, p. 085205, Aug 2017. 14, 58

[99] K. Dileep, R. Sahu, S. Sarkar, S. C. Peter, and R. Datta, "Layer specific optical band gap measurement at nanoscale in MoS2 and ReS2 van der Waals compounds by high resolution electron energy loss spectroscopy," Journal of Applied Physics, vol. 119, no. 11, p. 114309, 2016. 14, 58

[100] Ł. Kipczak, M. Grzeszczyk, K. Olkowska-Pucko, A. Babiński, and M. R. Molas, "The optical signature of few-layer ReSe2," Journal of Applied Physics, vol. 128, no. 4, p. 044302, 2020. 15, 59

[101] S. Tongay, H. Sahin, C. Ko, A. Luce, W. Fan, K. Liu, J. Zhou, Y.-S. Huang, C.-H. Ho, J. Yan, D. F. Ogletree, S. Aloni, J. Ji, S. Li, J. Li, F. M. Peeters, and J. Wu, "Monolayer behaviour in bulk ReS2 due to electronic and vibrational decoupling," Nature Communications, vol. 5, p. 3252, Feb 2014. 15, 58

[102] Z. G. Yu, Y. Cai, and Y.-W. Zhang, "Robust direct bandgap characteristics of one- and two-dimensional ReS2," Scientific Reports, vol. 5, p. 13783, Sep 2015. 15, 58

[103] Y. Feng, W. Zhou, Y. Wang, J. Zhou, E. Liu, Y. Fu, Z. Ni, X. Wu, H. Yuan, F. Miao, B. Wang, X. Wan, and D. Xing, "Raman vibrational spectra of bulk to monolayer ReS_2 with lower symmetry," Phys. Rev. B, vol. 92, p. 054110, Aug 2015. 15, 58

[104] B. Jariwala, D. Voiry, A. Jindal, B. A. Chalke, R. Bapat, A. Thamizhavel, M. Chhowalla, M. Deshmukh, and A. Bhattacharya, "Synthesis and characterization of ReS2 and ReSe2 layered chalcogenide single crystals," Chemistry of Materials, vol. 28, pp. 3352–3359, May 2016. 15, 58

[105] A. Arora, J. Noky, M. Drüppel, B. Jariwala, T. Deilmann, R. Schneider, R. Schmidt, O. Del Pozo-Zamudio, T. Stiehm, A. Bhattacharya, P. Krüger, S. Michaelis de Vasconcellos, M. Rohlfing, and R. Bratschitsch, "Highly anisotropic in-plane excitons in atomically thin and bulklike 1T-ReSe2," Nano Letters, vol. 17, pp. 3202–3207, May 2017. 15, 58, 59

[106] Y. Huang, C. Ho, P. Liao, and K. Tiong, "Temperature dependent study of the band edge excitons of ReS2 and ReSe2," Journal of Alloys and Compounds, vol. 262-263, pp. 92–96, 1997. Proceedings of the Twelfth International Conference on Solid Compounds of Transition Elements. 15

[107] D. Wolverson, S. Crampin, A. S. Kazemi, A. Ilie, and S. J. Bending, "Raman spectra of monolayer, few-layer, and bulk ReSe2: An anisotropic layered semiconductor," ACS Nano, vol. 8, pp. 11154–11164, Nov 2014. 15

[108] D. A. Chenet, O. B. Aslan, P. Y. Huang, C. Fan, A. M. van der Zande, T. F. Heinz, and J. C. Hone, "In-plane anisotropy in mono- and few-layer ReS2 probed by Raman spectroscopy and scanning transmission electron microscopy," Nano Letters, vol. 15, pp. 5667–5672, Sep 2015. 15, 19

[109] A. McCreary, J. R. Simpson, Y. Wang, D. Rhodes, K. Fujisawa, L. Balicas, M. Dubey, V. H. Crespi, M. Terrones, and A. R. Hight Walker, "Intricate resonant Raman response in anisotropic ReS2," Nano Letters, vol. 17, pp. 5897–5907, Oct 2017. 15

[110] Y. Choi, K. Kim, S. Y. Lim, J. Kim, J. M. Park, J. H. Kim, Z. Lee, and H. Cheong, "Complete determination of the crystallographic orientation of ReX2 (x = s, se) by polarized raman spectroscopy," Nanoscale Horiz., vol. 5, pp. 308–315, 2020. 15

[111] K. Tiong, C. Ho, and Y. Huang, "The electrical transport properties of ReS2 and ReSe2 layered crystals," Solid State Communications, vol. 111, no. 11, pp. 635–640, 1999. 15

[112] C. Ho, M. Hsieh, C. Wu, Y. Huang, and K. Tiong, "Dichroic optical and electrical properties of rhenium dichalcogenides layer compounds," Journal of Alloys and Compounds, vol. 442, no. 1, pp. 245 – 248, 2007. Proceedings of the 15th International Conference on Solid Compounds of Transition Elements. 15, 57

[113] C.-H. Ho and Z.-Z. Liu, "Complete-series excitonic dipole emissions in few layer ReS2 and ReSe2 observed by polarized photoluminescence spectroscopy," Nano Energy, vol. 56, pp. 641 – 650, 2019. 15, 58, 59

[114] A. Dhara, D. Chakrabarty, P. Das, A. K. Pattanayak, S. Paul, S. Mukherjee, and S. Dhara, "Additional excitonic features and momentum-dark states in ReS_2," Phys. Rev. B, vol. 102, p. 161404, Oct 2020. 15, 59, 80

[115] A. Castellanos-Gomez, M. Buscema, R. Molenaar, V. Singh, L. Janssen, H. S. J. van der Zant, and G. A. Steele, "Deterministic transfer of two-dimensional materials by all-dry viscoelastic stamping," 2D Materials, vol. 1, no. 1, p. 011002, 2014. 17

[116] C. Liang, Y. Chan, K. Tiong, Y. Huang, Y. Chen, D. Dumcenco, and C. Ho, "Optical anisotropy of Au-doped ReS2 crystals," Journal of Alloys and Compounds, vol. 480, no. 1, pp. 94–96, 2009. Proceedings of the 16th International Conference on Solid Compounds of Transition Elements (SCTE 2008). 19

[117] K. Kośmider, J. W. González, and J. Fernández-Rossier, "Large spin splitting in the conduction band of transition metal dichalcogenide monolayers," Phys. Rev. B, vol. 88, p. 245436, Dec 2013. 26, 41, 85

[118] J. P. Echeverry, B. Urbaszek, T. Amand, X. Marie, and I. C. Gerber, "Splitting between bright and dark excitons in transition metal dichalcogenide monolayers," Phys. Rev. B, vol. 93, p. 121107, Mar 2016. 26, 43, 49, 58

[119] G. Wang, C. Robert, A. Suslu, B. Chen, S. Yang, S. Alamdari, I. C. Gerber, T. Amand, X. Marie, S. Tongay, and B. Urbaszek, "Spin-orbit engineering in transition metal dichalcogenide alloy monolayers," Nat. Comm., vol. 6, p. 10110, Dec 2015. Article. 26, 42

[120] X.-X. Zhang, Y. You, S. Y. F. Zhao, and T. F. Heinz, "Experimental evidence for dark excitons in monolayer WSe_2," Phys. Rev. Lett., vol. 115, p. 257403, Dec 2015. 26, 28, 31, 42

[121] F. Withers, O. Del Pozo-Zamudio, S. Schwarz, S. Dufferwiel, P. M. Walker, T. Godde, A. P. Rooney, A. Gholinia, C. R. Woods, P. Blake, S. J. Haigh, K. Watanabe, T. Taniguchi, I. L. Aleiner, A. K. Geim, V. I. Fal'ko, A. I. Tartakovskii, and K. S. Novoselov, "WSe2 light-emitting tunneling transistors with enhanced brightness at room temperature," Nano Letters, vol. 15, no. 12, pp. 8223–8228, 2015. 26, 42

[122] A. Arora, M. Koperski, K. Nogajewski, J. Marcus, C. Faugeras, and M. Potemski, "Excitonic resonances in thin films of WSe2: from monolayer to bulk material," Nanoscale, vol. 7, p. 10421, 2015. 26, 42, 83, 89

[123] M. Yang, C. Robert, Z. Lu, D. Van Tuan, D. Smirnov, X. Marie, and H. Dery, "Exciton valley depolarization in monolayer transition-metal dichalcogenides," Phys. Rev. B, vol. 101, p. 115307, Mar 2020. 26

[124] M. M. Glazov, T. Amand, X. Marie, D. Lagarde, L. Bouet, and B. Urbaszek, "Exciton fine structure and spin decoherence in monolayers of transition metal dichalcogenides," Phys. Rev. B, vol. 89, p. 201302, May 2014. 26

[125] A. O. Slobodeniuk and D. M. Basko, "Corrigendum: Spin-flip processes and radiative decay of dark intravalley excitons in transition metal dichalcogenide monolayers," 2D Materials, vol. 6, p. 029501, jan 2019. 26, 27

[126] H. Dery and Y. Song, "Polarization analysis of excitons in monolayer and bilayer transition-metal dichalcogenides," Phys. Rev. B, vol. 92, p. 125431, Sep 2015. 26, 43

[127] S. Glasberg, H. Shtrikman, I. Bar-Joseph, and P. C. Klipstein, "Exciton exchange splitting in wide GaAs quantum wells," Phys. Rev. B, vol. 60, pp. R16295–R16298, Dec 1999. 28

[128] M. Bayer, O. Stern, A. Kuther, and A. Forchel, "Spectroscopic study of dark excitons in $In_xGa_{1-x}As$ self-assembled quantum dots by a magnetic-field-induced symmetry breaking," Phys. Rev. B, vol. 61, pp. 7273–7276, Mar 2000. 28, 70

[129] K. Kowalik, O. Krebs, A. Golnik, J. Suffczyński, P. Wojnar, J. Kossut, J. A. Gaj, and P. Voisin, "Manipulating the exciton fine structure of single CdTe/ZnTe quantum dots by an in-plane magnetic field," Phys. Rev. B, vol. 75, p. 195340, May 2007. 28

[130] S. Zaric, G. N. Ostojic, J. Kono, J. Shaver, V. C. Moore, M. S. Strano, R. H. Hauge, R. E. Smalley, and X. Wei, "Optical signatures of the Aharonov-Bohm phase in single-walled carbon nanotubes," Science, vol. 304, no. 5674, pp. 1129–1131, 2004. 28

[131] J. Shaver, J. Kono, O. Portugall, V. Krstić, G. L. J. A. Rikken, Y. Miyauchi, S. Maruyama, and V. Perebeinos, "Magnetic brightening of carbon nanotube photoluminescence through symmetry breaking," Nano Letters, vol. 7, pp. 1851–1855, Jul 2007. 28

[132] A. Srivastava, H. Htoon, V. I. Klimov, and J. Kono, "Direct observation of dark excitons in individual carbon nanotubes: Inhomogeneity in the exchange splitting," Phys. Rev. Lett., vol. 101, p. 087402, Aug 2008. 28

[133] M. Goryca, P. Plochocka, T. Kazimierczuk, P. Wojnar, G. Karczewski, J. A. Gaj, M. Potemski, and P. Kossacki, "Brightening of dark excitons in a single CdTe quantum dot containing a single Mn^{2+} ion," Phys. Rev. B, vol. 82, p. 165323, Oct 2010. 28

[134] M. Zinkiewicz, A. O. Slobodeniuk, T. Kazimierczuk, P. Kapuściński, K. Oreszczuk, M. Grzeszczyk, M. Bartos, K. Nogajewski, K. Watanabe, T. Taniguchi, C. Faugeras, P. Kossacki, M. Potemski, A. Babiński, and M. R. Molas, "Neutral and charged dark excitons in monolayer WS2," Nanoscale, vol. 12, pp. 18153–18159, 2020. 28, 31, 41, 42, 43, 44, 58, 87, 88

[135] E. Liu, J. van Baren, Z. Lu, M. M. Altaiary, T. Taniguchi, K. Watanabe, D. Smirnov, and C. H. Lui, "Gate tunable dark trions in monolayer WSe_2," Phys. Rev. Lett., vol. 123, p. 027401, Jul 2019. 28

[136] Z. Lu, D. Rhodes, Z. Li, D. V. Tuan, Y. Jiang, J. Ludwig, Z. Jiang, Z. Lian, S.-F. Shi, J. Hone, H. Dery, and D. Smirnov, "Magnetic field mixing and splitting of bright and dark excitons in monolayer MoSe2," 2D Materials, vol. 7, p. 015017, nov 2019. 28, 34, 41, 42, 44, 58

[137] M. Bieniek, L. Szulakowska, and P. Hawrylak, "Effect of valley, spin, and band nesting on the electronic properties of gated quantum dots in a single layer of transition metal dichalcogenides," Phys. Rev. B, vol. 101, p. 035401, Jan 2020. 28, 49

[138] C. Robert, M. A. Semina, F. Cadiz, M. Manca, E. Courtade, T. Taniguchi, K. Watanabe, H. Cai, S. Tongay, B. Lassagne, P. Renucci, T. Amand, X. Marie, M. M. Glazov, and B. Urbaszek, "Optical spectroscopy of excited exciton states in MoS_2 monolayers in van der Waals heterostructures," Phys. Rev. Materials, vol. 2, p. 011001, Jan 2018. 31

[139] Y. Zhou, G. Scuri, D. S. Wild, A. A. High, A. Dibos, L. A. Jauregui, C. Shu, K. De Greve, K. Pistunova, A. Y. Joe, T. Taniguchi, K. Watanabe, P. Kim, M. D. Lukin, and H. Park, "Probing dark excitons in atomically thin semiconductors via near-field coupling to surface plasmon polaritons," Nature Nanotechnology, vol. 12, p. 856, Jun 2017. 41

[140] J. G. Roch, G. Froehlicher, N. Leisgang, P. Makk, K. Watanabe, T. Taniguchi, and R. J. Warburton, "Spin-polarized electrons in monolayer MoS2," Nature Nanotechnology, vol. 14, pp. 432–436, May 2019. 42, 85

[141] C. Robert, R. Picard, D. Lagarde, G. Wang, J. P. Echeverry, F. Cadiz, P. Renucci, A. Högele, T. Amand, X. Marie, I. C. Gerber, and B. Urbaszek, "Excitonic properties of semiconducting monolayer and bilayer $MoTe_2$," Phys. Rev. B, vol. 94, p. 155425, Oct 2016. 42, 43

[142] M. Baranowski, A. Surrente, D. K. Maude, M. Ballottin, A. A. Mitioglu, P. C. M. Christianen, Y. C. Kung, D. Dumcenco, A. Kis, and P. Plochocka, "Dark excitons and the elusive valley polarization in transition metal dichalcogenides," 2D Materials, vol. 4, p. 025016, feb 2017. 42

[143] G. Wang, X. Marie, I. Gerber, T. Amand, D. Lagarde, L. Bouet, M. Vidal, A. Balocchi, and B. Urbaszek, "Giant enhancement of the optical second-harmonic emission of WSe_2 monolayers by laser excitation at exciton resonances," Phys. Rev. Lett., vol. 114, p. 097403, Mar 2015. 42

[144] P. K. Nayak, F.-C. Lin, C.-H. Yeh, J.-S. Huang, and P.-W. Chiu, "Robust room temperature valley polarization in monolayer and bilayer WS2," Nanoscale, vol. 8, pp. 6035–6042, 2016. 42

[145] G. Plechinger, P. Nagler, J. Kraus, N. Paradiso, C. Strunk, C. Schüller, and T. Korn, "Identification of excitons, trions and biexcitons in single-layer WS_2," Phys. Stat. Sol. RRL, vol. 9, no. 8, p. 457, 2015. 42, 83, 84, 88, 89, 93

[146] G. Wang, L. Bouet, D. Lagarde, M. Vidal, A. Balocchi, T. Amand, X. Marie, and B. Urbaszek, "Valley dynamics probed through charged and neutral exciton emission in monolayer WSe_2," Phys. Rev. B, vol. 90, p. 075413, Aug 2014. 42

[147] T. Scrace, Y. Tsai, B. Barman, L. Schweidenback, A. Petrou, G. Kioseoglou, I. Ozfidan, M. Korkusinski, and P. Hawrylak, "Magnetoluminescence and valley polarized state of a two-dimensional electron gas in WS2 monolayers," Nat. Nanotechnol., vol. 10, p. 603, 2015. 42, 87

[148] G. Kioseoglou, A. T. Hanbicki, M. Currie, A. L. Friedman, D. Gunlycke, and B. T. Jonker, "Valley polarization and intervalley scattering in monolayer MoS2," Applied Physics Letters, vol. 101, no. 22, p. 221907, 2012. 42

[149] D. Lagarde, L. Bouet, X. Marie, C. R. Zhu, B. L. Liu, T. Amand, P. H. Tan, and B. Urbaszek, "Carrier and polarization dynamics in monolayer MoS_2," Phys. Rev. Lett., vol. 112, p. 047401, Jan 2014. 42

[150] G. Kioseoglou, A. T. Hanbicki, M. Currie, A. L. Friedman, and B. T. Jonker, "Optical polarization and intervalley scattering in single layers of MoS2 and MoSe2," Scientific Reports, vol. 6, p. 25041, Apr 2016. 43

[151] G. Wang, E. Palleau, T. Amand, S. Tongay, X. Marie, and B. Urbaszek, "Polarization and time-resolved photoluminescence spectroscopy of excitons in MoSe2 monolayers," Applied Physics Letters, vol. 106, no. 11, p. 112101, 2015. 43

[152] H. Tornatzky, A.-M. Kaulitz, and J. Maultzsch, "Resonance profiles of valley polarization in single-layer MoS_2 and $MoSe_2$," Phys. Rev. Lett., vol. 121, p. 167401, Oct 2018. 43

[153] M. Yang, C. Robert, Z. Lu, D. Van Tuan, D. Smirnov, X. Marie, and H. Dery, "Exciton valley depolarization in monolayer transition-metal dichalcogenides," Phys. Rev. B, vol. 101, p. 115307, Mar 2020. 43

[154] M. Koperski, M. R. Molas, A. Arora, K. Nogajewski, M. Bartos, J. Wyzula, D. Vaclavkova, P. Kossacki, and M. Potemski, "Orbital, spin and valley contributions to zeeman splitting of excitonic resonances in MoSe2, WSe2 and WS2 monolayers," 2D Materials, vol. 6, no. 1, p. 015001, 2019. 44, 93

[155] T. Deilmann, P. Krüger, and M. Rohlfing, "Ab initio studies of exciton g factors: Monolayer transition metal dichalcogenides in magnetic fields," Phys. Rev. Lett., vol. 124, p. 226402, Jun 2020. 45

[156] T. Woźniak, P. E. Faria Junior, G. Seifert, A. Chaves, and J. Kunstmann, "Exciton g factors of van der waals heterostructures from first-principles calculations," Phys. Rev. B, vol. 101, p. 235408, Jun 2020. 45

[157] T. Deilmann and K. S. Thygesen, "Dark excitations in monolayer transition metal dichalcogenides," Phys. Rev. B, vol. 96, p. 201113, Nov 2017. 49

[158] A. Delhomme, G. Butseraen, B. Zheng, L. Marty, V. Bouchiat, M. R. Molas, A. Pan, K. Watanabe, T. Taniguchi, A. Ouerghi, J. Renard, and C. Faugeras, "Magneto-spectroscopy of exciton rydberg states in a CVD grown WSe2 monolayer," Applied Physics Letters, vol. 114, no. 23, p. 232104, 2019. 49, 50

[159] A. Farenbruch, D. Fröhlich, D. R. Yakovlev, and M. Bayer, "Rydberg series of dark excitons in Cu_2O," Phys. Rev. Lett., vol. 125, p. 207402, Nov 2020. 49

[160] K. Watanabe, K. Uchida, and N. Miura, "Magneto-optical effects observed for GaSe in megagauss magnetic fields," Phys. Rev. B, vol. 68, p. 155312, Oct 2003. 49

[161] Y. Nagamune, S. Takeyama, and N. Miura, "Exciton spectra and anisotropic Zeeman effect in PbI_2 at high magnetic fields up to 40 T," Phys. Rev. B, vol. 43, pp. 12401–12405, May 1991. 49

[162] Z. Li, T. Wang, C. Jin, Z. Lu, Z. Lian, Y. Meng, M. Blei, S. Gao, T. Taniguchi, K. Watanabe, T. Ren, S. Tongay, L. Yang, D. Smirnov, T. Cao, and S.-F. Shi, "Emerging photoluminescence from the dark-exciton phonon replica in monolayer WSe2," Nature Communications, vol. 10, p. 2469, Jun 2019. 49, 59, 87

[163] E. Liu, J. van Baren, T. Taniguchi, K. Watanabe, Y.-C. Chang, and C. H. Lui, "Valley-selective chiral phonon replicas of dark excitons and trions in monolayer WSe_2," Phys. Rev. Research, vol. 1, p. 032007, Oct 2019. 49, 59, 87

[164] M. He, P. Rivera, D. Van Tuan, N. P. Wilson, M. Yang, T. Taniguchi, K. Watanabe, J. Yan, D. G. Mandrus, H. Yu, H. Dery, W. Yao, and X. Xu, "Valley phonons and exciton complexes in a monolayer semiconductor," Nature Communications, vol. 11, p. 618, Jan 2020. 49, 59, 87

[165] M. Paur, A. J. Molina-Mendoza, R. Bratschitsch, K. Watanabe, T. Taniguchi, and T. Mueller, "Electroluminescence from multi-particle exciton complexes in transition metal dichalcogenide semiconductors," Nature Communications, vol. 10, no. 1, p. 1709, 2019. 49, 59, 88, 89

[166] M. Barbone, A. R. P. Montblanch, D. M. Kara, C. Palacios-Berraquero, A. R. Cadore, D. De Fazio, B. Pingault, E. Mostaani, H. Li, B. Chen, K. Watanabe, T. Taniguchi, S. Tongay, G. Wang, A. C. Ferrari, and M. Atatüre, "Charge-tuneable biexciton complexes in monolayer WSe2," Nature Communications, vol. 9, no. 1, p. 3721, 2018. 49, 59

[167] Z. Li, T. Wang, Z. Lu, C. Jin, Y. Chen, Y. Meng, Z. Lian, T. Taniguchi, K. Watanabe, S. Zhang, D. Smirnov, and S.-F. Shi, "Revealing the biexciton and trion-exciton complexes in bn encapsulated WSe2," Nature Communications, vol. 9, no. 1, p. 3719, 2018. 49, 59

[168] K. Kośmider, J. W. González, and J. Fernández-Rossier, "Large spin splitting in the conduction band of transition metal dichalcogenide monolayers," Phys. Rev. B, vol. 88, p. 245436, Dec 2013. 55

[169] C. H. Ho, Y. S. Huang, K. K. Tiong, and P. C. Liao, "Absorption-edge anisotropy in ReS_2 and $ReSe_2$ layered semiconductors," Phys. Rev. B, vol. 58, pp. 16130–16135, Dec 1998. 57

[170] D. Y. Lin, T. P. Huang, F. L. Wu, C. M. Lin, Y. S. Huang, and K. K. Tiong, "Anisotropy of photoluminescence in layered semiconductors Re2 and ReS2:Au," in Solid Compounds of Transition Elements I, vol. 170 of Solid State Phenomena, pp. 135–138, Trans Tech Publications Ltd, 3 2011. 57

[171] R. Oliva, M. Laurien, F. Dybala, J. Kopaczek, Y. Qin, S. Tongay, O. Rubel, and R. Kudrawiec, "Pressure dependence of direct optical transitions in ReS2 and ReSe2," npj 2D Materials and Applications, vol. 3, p. 20, May 2019. 58

[172] O. B. Aslan, D. A. Chenet, A. M. van der Zande, J. C. Hone, and T. F. Heinz, "Linearly polarized excitons in single- and few-layer ReS2 crystals," ACS Photonics, vol. 3, pp. 96–101, Jan 2016. 58, 59

[173] S. Sim, D. Lee, J. Lee, H. Bae, M. Noh, S. Cha, M.-H. Jo, K. Lee, and H. Choi, "Light polarization-controlled conversion of ultrafast coherent–incoherent exciton dynamics in few-layer ReS2," Nano Letters, vol. 19, pp. 7464–7469, Oct 2019. 58

[174] J. Wang, Y. J. Zhou, D. Xiang, S. J. Ng, K. Watanabe, T. Taniguchi, and G. Eda, "Polarized light-emitting diodes based on anisotropic excitons in few-layer ReS2," Advanced Materials, vol. 32, no. 32, p. 2001890, 2020. 58

[175] E. Zhang, Y. Jin, X. Yuan, W. Wang, C. Zhang, L. Tang, S. Liu, P. Zhou, W. Hu, and F. Xiu, "ReS2-based field-effect transistors and photodetectors," Advanced Functional Materials, vol. 25, no. 26, pp. 4076–4082, 2015. 58

[176] J. Kwon, Y. Shin, H. Kwon, J. Y. Lee, H. Park, K. Watanabe, T. Taniguchi, J. Kim, C.-H. Lee, S. Im, and G.-H. Lee, "All-2D ReS2 transistors with split gates for logic circuitry," Scientific Reports, vol. 9, p. 10354, Jul 2019. 58

[177] M. Koperski, M. R. Molas, A. Arora, K. Nogajewski, A. Slobodeniuk, C. Faugeras, and M. Potemski, "Optical properties of atomically thin transition metal dichalcogenides: Observations and puzzles," Nanophotonics, vol. 6, p. 1289, 2017. 58

[178] J. Xiao, M. Zhao, Y. Wang, and X. Zhang, "Excitons in atomically thin 2D semiconductors and their applications," Nanophotonics, vol. 6, no. 6, pp. 1309 – 1328, 2017. 58

[179] G. Wang, A. Chernikov, M. M. Glazov, T. F. Heinz, X. Marie, T. Amand, and B. Urbaszek, "Colloquium: Excitons in atomically thin transition metal dichalcogenides," Rev. Mod. Phys., vol. 90, p. 021001, Apr 2018. 58

[180] S. Sim, D. Lee, A. V. Trifonov, T. Kim, S. Cha, J. H. Sung, S. Cho, W. Shim, M.-H. Jo, and H. Choi, "Ultrafast quantum beats of anisotropic excitons in atomically thin ReS2," Nature Communications, vol. 9, p. 351, Jan 2018. 58, 59

[181] C. Robert, B. Han, P. Kapuscinski, A. Delhomme, C. Faugeras, T. Amand, M. R. Molas, M. Bartos, K. Watanabe, T. Taniguchi, B. Urbaszek, M. Potemski, and X. Marie, "Measurement of the spin-forbidden dark excitons in MoS2 and MoSe2 monolayers," Nature Communications, vol. 11, p. 4037, Aug 2020. 58

[182] M. Zinkiewicz, T. Woźniak, T. Kazimierczuk, P. Kapuscinski, K. Oreszczuk, M. Grzeszczyk, M. Bartoš, K. Nogajewski, K. Watanabe, T. Taniguchi, C. Faugeras, P. Kossacki, M. Potemski, A. Babiński, and M. R. Molas, "Excitonic complexes in n-doped WS2 monolayer," Nano Letters, vol. 21, pp. 2519–2525, Mar 2021. 59, 87, 88

[183] J. L. Webb, L. S. Hart, D. Wolverson, C. Chen, J. Avila, and M. C. Asensio, "Electronic band structure of ReS_2 by high-resolution angle-resolved photoemission spectroscopy," Phys. Rev. B, vol. 96, p. 115205, Sep 2017. 64

[184] B. J. Witek, R. W. Heeres, U. Perinetti, E. P. A. M. Bakkers, L. P. Kouwenhoven, and V. Zwiller, "Measurement of the g-factor tensor in a quantum dot and disentanglement of exciton spins," Phys. Rev. B, vol. 84, p. 195305, Nov 2011. 70

[185] A. Bogucki, T. Smoleński, M. Goryca, T. Kazimierczuk, J. Kobak, W. Pacuski, P. Wojnar, and P. Kossacki, "Anisotropy of in-plane hole g factor in CdTe/ZnTe quantum dots," Phys. Rev. B, vol. 93, p. 235410, Jun 2016. 70

[186] S. Germanis, P. Atkinson, R. Hostein, C. Gourdon, V. Voliotis, A. Lemaître, M. Bernard, F. Margaillan, S. Majrab, and B. Eble, "Dark-bright exciton coupling in asymmetric quantum dots," Phys. Rev. B, vol. 98, p. 155303, Oct 2018. 70

[187] G. Finkelstein, H. Shtrikman, and I. Bar-Joseph, "Optical spectroscopy of a two-dimensional electron gas near the metal-insulator transition," Phys. Rev. Lett., vol. 74, pp. 976–979, Feb 1995. 83

[188] A. Shields, J. Osborne, M. Simmons, M. Pepper, and D. Ritchie, "Magneto-optical spectroscopy of positively charged excitons in GaAs quantum wells," Phys. Rev. B, vol. 52, pp. R5523–R5526, Aug 1995. 83

[189] L. Landin, M. S. Miller, M.-E. Pistol, C. E. Pryor, and L. Samuelson, "Optical studies of individual InAs quantum dots in GaAs: Few-particle effects," Science, vol. 280, no. 5361, pp. 262–264, 1998. 83

[190] K. F. Karlsson, E. S. Moskalenko, P. O. Holtz, B. Monemar, W. V. Schoenfeld, J. M. Garcia, and P. M. Petroff, "Temperature influence on optical charging of self-assembled InAs/GaAs semiconductor quantum dots," Applied Physics Letters, vol. 78, no. 19, pp. 2952–2954, 2001. 83

[191] D. Haft, R. J. Warburton, K. Karrai, S. Huant, G. Medeiros-Ribeiro, J. M. Garcia, W. Schoenfeld, and P. M. Petroff, "Luminescence quenching in InAs quantum dots," Applied Physics Letters, vol. 78, no. 19, pp. 2946–2948, 2001. 83

[192] A. Manassen, E. Cohen, A. Ron, E. Linder, and L. N. Pfeiffer, "Exciton and trion spectral line shape in the presence of an electron gas in GaAs/AlAs quantum wells," Phys. Rev. B, vol. 54, pp. 10609–10613, Oct 1996. 83

[193] S. Glasberg, G. Finkelstein, H. Shtrikman, and I. Bar-Joseph, "Comparative study of the negatively and positively charged excitons in GaAs quantum wells," Phys. Rev. B, vol. 59, pp. R10425–R10428, Apr 1999. 83

[194] J. Yang, T. Lü, Y. W. Myint, J. Pei, D. Macdonald, J.-C. Zheng, and Y. Lu, "Robust excitons and trions in monolayer MoTe2," ACS Nano, vol. 9, pp. 6603–6609, Jun 2015. 83

[195] J. Jadczak, A. Delgado, L. Bryja, Y. S. Huang, and P. Hawrylak, "Robust high-temperature trion emission in monolayers of $Mo(S_ySe_{1-y})_2$ alloys," Phys. Rev. B, vol. 95, p. 195427, May 2017. 83

[196] A. R. Klots, A. K. M. Newaz, B. Wang, D. Prasai, H. Krzyzanowska, J. Lin, D. Caudel, N. J. Ghimire, J. Yan, B. L. Ivanov, K. A. Velizhanin, A. Burger, D. G. Mandrus, N. H. Tolk, S. T. Pantelides, and K. I. Bolotin, "Probing excitonic states in suspended two-dimensional semiconductors by photocurrent spectroscopy," Scientific Reports, vol. 4, p. 6608, Oct 2014. 83

[197] A. Hanbicki, M. Currie, G. Kioseoglou, A. Friedman, and B. Jonker, "Measurement of high exciton binding energy in the monolayer transition-metal dichalcogenides WS2 and WSe2," Solid State Communications, vol. 203, pp. 16 – 20, 2015. 83

[198] M. Szyniszewski, E. Mostaani, N. D. Drummond, and V. I. Fal'ko, "Binding energies of trions and biexcitons in two-dimensional semiconductors from diffusion quantum Monte Carlo calculations," Phys. Rev. B, vol. 95, p. 081301, Feb 2017. 83

[199] J. Legma, G. Vacquier, and A. Casalot, "Chemical vapour transport of molybdenum and tungsten diselenides by various transport agents," Journal of Crystal Growth, vol. 130, no. 1, pp. 253 – 258, 1993. 84

[200] J. A. Baglio, G. S. Calabrese, D. J. Harrison, E. Kamieniecki, A. J. Ricco, M. S. Wrighton, and G. D. Zoski, "Electrochemical characterization of p-type semiconducting tungsten disulfide photocathodes: efficient photoreduction processes at semiconductor/liquid electrolyte interfaces," Journal of the American Chemical Society, vol. 105, pp. 2246–2256, Apr 1983. 84

[201] Y. Li, Z. Qi, M. Liu, Y. Wang, X. Cheng, G. Zhang, and L. Sheng, "Photoluminescence of monolayer MoS2 on LaAlO3 and SrTiO3 substrates," Nanoscale, vol. 6, pp. 15248–15254, 2014. 84

[202] K. Dolui, I. Rungger, and S. Sanvito, "Origin of the n-type and p-type conductivity of MoS_2 monolayers on a SiO_2 substrate," Phys. Rev. B, vol. 87, p. 165402, Apr 2013. 84

[203] B. Radisavljevic, A. Radenovic, J. Brivio, V. Giacometti, and A. Kis, "Single-layer MoS2 transistors," Nat. Nanotechnol., vol. 6, p. 147, 2011. 84

[204] D. Sercombe, S. Schwarz, O. D. Pozo-Zamudio, F. Liu, B. J. Robinson, E. A. Chekhovich, I. I. Tartakovskii, O. Kolosov, and A. I. Tartakovskii, "Optical investigation of the natural electron doping in thin MoS2 films deposited on dielectric substrates," Scientific Reports, vol. 3, p. 3489, Dec 2013. 84

[205] H. Li, G. Lu, Z. Yin, Q. He, H. Li, Q. Zhang, and H. Zhang, "Optical identification of single- and few-layer MoS2 sheets," Small, vol. 8, no. 5, pp. 682–686, 2012. 84

[206] A. Singh and A. K. Singh, "Origin of n-type conductivity of monolayer MoS_2," Phys. Rev. B, vol. 99, p. 121201, Mar 2019. 84

[207] M. R. Molas, K. Nogajewski, A. O. Slobodeniuk, J. Binder, M. Bartos, and M. Potemski, "The optical response of monolayer, few-layer and bulk tungsten disulfide," Nanoscale, vol. 9, p. 13128, 2017. 84, 87, 88, 89, 93

[208] G. Plechinger, P. Nagler, A. Arora, R. Schmidt, A. Chernikov, A. G. del Águila, P. C. Christianen, R. Bratschitsch, C. Schüller, and T. Korn, "Trion fine structure and coupled spin–valley dynamics in monolayer tungsten disulfide," Nature Communications, vol. 7, p. 12715, 2016. 84, 87, 89, 93

[209] A. J. Shields, M. Pepper, M. Y. Simmons, and D. A. Ritchie, "Spin-triplet negatively charged excitons in GaAs quantum wells," Phys. Rev. B, vol. 52, p. 7841, Sep 1995. 84

[210] J. Jadczak, J. Kutrowska-Girzycka, M. Bieniek, T. Kazimierczuk, P. Kossacki, J. J. Schindler, J. Debus, K. Watanabe, T. Taniguchi, C. H. Ho, A. Wójs, P. Hawrylak, and L. Bryja, "Probing negatively charged and neutral excitons in MoS2/hBN and hBN/MoS2/hBN van der Waals heterostructures," Nanotechnology, vol. 32, p. 145717, jan 2021. 85

[211] J. R. Schaibley, H. Yu, G. Clark, P. Rivera, J. S. Ross, K. L. Seyler, W. Yao, and X. Xu, "Valleytronics in 2D materials," Nat. Rev. Mat., vol. 1, p. 16055, Aug 2016. Review Article. 86

[212] Z. Ye, L. Waldecker, E. Y. Ma, D. Rhodes, A. Antony, B. Kim, X.-X. Zhang, M. Deng, Y. Jiang, Z. Lu, D. Smirnov, K. Watanabe, T. Taniguchi, J. Hone, and T. F. Heinz, "Efficient generation of neutral and charged biexcitons in encapsulated WSe2 monolayers," Nature Communications, vol. 9, p. 3718, Sep 2018. 87

[213] A. Chernikov, A. M. van der Zande, H. M. Hill, A. F. Rigosi, A. Velauthapillai, J. Hone, and T. F. Heinz, "Electrical tuning of exciton binding energies in monolayer WS_2," Phys. Rev. Lett., vol. 115, p. 126802, Sep 2015. 87, 89

[214] J. Jadczak, L. Bryja, J. Kutrowska-Girzycka, P. Kapuściński, M. Bieniek, Y.-S. Huang, and P. Hawrylak, "Room temperature multi-phonon upconversion photoluminescence in monolayer semiconductor WS2," Nature Communications, vol. 10, no. 1, p. 107, 2019. 87, 88

[215] T. Jakubczyk, K. Nogajewski, M. R. Molas, M. Bartos, W. Langbein, M. Potemski, and J. Kasprzak, "Impact of environment on dynamics of exciton complexes in a WS2 monolayer," 2D Materials, vol. 5, p. 031007, apr 2018. 88

[216] A. Arora, N. K. Wessling, T. Deilmann, T. Reichenauer, P. Steeger, P. Kossacki, M. Potemski, S. Michaelis de Vasconcellos, M. Rohlfing, and R. Bratschitsch, "Dark trions govern the temperature-dependent optical absorption and emission of doped atomically thin semiconductors," Phys. Rev. B, vol. 101, p. 241413, Jun 2020. 88

[217] Y. Li, A. Chernikov, X. Zhang, A. Rigosi, H. M. Hill, A. M. van der Zande, D. A. Chenet, E.-M. Shih, J. Hone, and T. F. Heinz, "Measurement of the optical dielectric function of monolayer transition-metal dichalcogenides: MoS_2, $MoSe_2$, WS_2, and WSe_2," Phys. Rev. B, vol. 90, p. 205422, Nov 2014. 89

[218] A. Arora, K. Nogajewski, M. Molas, M. Koperski, and M. Potemski, "Exciton band structure in layered MoSe2: from a monolayer to the bulk limit," Nanoscale, vol. 7, p. 20769, 2015. 89

[219] J. Shang, X. Shen, C. Cong, N. Peimyoo, B. Cao, M. Eginligil, and T. Yu, "Observation of excitonic fine structure in a 2D transition-metal dichalcogenide semiconductor," ACS Nano, vol. 9, no. 1, p. 647, 2015. 89

[220] T. Smoleński, O. Cotlet, A. Popert, P. Back, Y. Shimazaki, P. Knüppel, N. Dietler, T. Taniguchi, K. Watanabe, M. Kroner, and A. Imamoglu, "Interaction-induced Shubnikov-de Haas oscillations in optical conductivity of monolayer $MoSe_2$," Phys. Rev. Lett., vol. 123, p. 097403, Aug 2019. 95